Scalar Field Wave Dark Matter and Galactic Halos

by

Benjamin Hamm

Department of Physics
Duke University

Date: _____

Approved:

_____
Hubert Bray, Advisor

_____
Christopher Walter

_____
Thomas Mehen

_____
Michael Troxel

_____
Daniel Scolnic

Dissertation submitted in partial fulfillment of the requirements for the degree of
Doctor of Philosophy in the Department of Physics
in the Graduate School of Duke University
2021

Abstract

Scalar Field Wave Dark Matter and Galactic Halos

by

Benjamin Hamm

Department of Physics
Duke University

Date: _____

Approved:

_____
Hubert Bray, Advisor

_____
Christopher Walter

_____
Thomas Mehen

_____
Michael Troxel

_____
Daniel Scolnic

An abstract of a dissertation submitted in partial fulfillment of the requirements for the degree of Doctor of Philosophy in the Department of Physics in the Graduate School of Duke University
2021

Abstract

The question of "What is Dark Matter?" has been a focus of cosmological research since the turn of the 20th century. Though the composition of Dark Matter is unknown, the existence of Dark Matter is crucial to the modern theory of cosmology. We focus on a theory of Dark Matter referred to as *Scalar Field Wave Dark Matter* (SFψDM), which has received an increasing amount of interest from the research community since the late 2000s. SFψDM is a peculiar theory in which Dark Matter is composed of ultralight bosonic particles. As a result, SFψDM has an astronomically large deBroglie wavelength, generating complicated wave dynamics on the largest cosmological scales.

This thesis focuses on describing the status of SFψDM theory, SFψDM halos, and how SFψDM halos are affected by the wave-like features of the scalar field. In particular, we offer an analysis of galactic rotation curves and how they relate to SFψDM excited states. This analysis yields a novel model for an observed galactic trend referred to as the Baryonic Tully-Fisher Relation. Furthering this model, we formulate an eigenfunction decomposition which can be used to describe superpositions of excited states. Finally, we examine these superposition states and discuss how they can be used to generate both oscillating and rotating patterns in SFψDM halos.

Dedicated to all who challenge the norm and push the boundaries of convention, and in spite of all those who advise against doing so. Lead the world into the unknown because you know it's the right choice, never turn back, and love and respect the life that it brings you.

Contents

List of Tables

List of Figures

List of Abbreviations and Symbols

Symbols

Mathematical Conventions

$\mathbf{G}$	Bolded variables: Coordinate-Free Representations
G_{ij}	Subscripts i,j,k, α,β,γ: Coordinate Indices
V_r	Subscripts r, t, θ, ϕ: Differentiation
ψ_{nlm}	Subscripts n, l, m: Eigenfunction Indices
$\otimes$	Tensor product
$\bar{\psi}$	Barred Variable: Complex Conjugation
$M_\odot$	Solar Masses
∇	Connection
$\vec{\nabla}$	3D Gradient
∇^2	3D Laplacian
∂_x	Partial Derivative $\frac{\partial}{\partial x}$
$\mathbf{d}$	Exterior Derivative

Abbreviations

SFψDM	Scalar Field Wave Dark Matter
SSS	Spherically Symmetric and Static
EKG	Einstein-Klein-Gordon
PS	Poisson-Schrodinger

Acknowledgements

Thank you to the reader for taking on such a huge task in reading.

I thank my advisor, Hugh Bray. Hugh, thank you for approaching our most challenging questions and conversations with a smile. Your enjoyment of problems that seem impossibly difficult is truly inspiring.

I wish a special thank you to my committee members - you make it possible for me to complete this journey. Thank you for including me in your groups and thank you for all of the time you've given towards this final interrogation.

Thank you to Philip Mocz for collaborating and sharing his works on SFψDM with me and my group. Philip, thank you for sharing your numerics, experience, and curiosity!

Thank you to James Wheeler, I envy your attention to logical and mathematical detail, it's helped keep me honest throughout these years. As my academic sibling, I wish you good luck next year! Thank you to Arya Roy, you are an unashamed educator - thank you for having me as part of your staff for so long - your classes have always been a joy and I will miss them!

Thanks to my two older siblings, Brandon and Audri. I know you didn't help with the thesis, but I know I'd only have to ask - cheers guys! For my other half, Tabitha - You gave me a reason to stay sane through this ordeal. I love you and your sarcasm and can't wait to live our next adventure together.

Mom, in the face of life's greatest trials you never fail to remind me to take a step back and appreciate where I've come and where I've yet to go. You are the only person that I would write this thesis for twice. Thank you so much, I love you more than you could imagine.

1

Introduction: Wave Dark Matter

This introductory chapter will serve three main purposes: it will familiarize the reader with the various mathematical notations and requirements for the theoretical aspects of the thesis, it will introduce the notion of Dark Matter in the context of modern cosmology, and will offer a brief review of the Scalar Field Wave Dark Matter theory. Section 1.1 will focus on the mathematical preliminaries. Sections 1.2-1.3 will introduce General Relativity and the modern theory of cosmology as well as describe the basic context of the problem of Dark Matter. Finally, sections 1.4 and 1.5 will introduce Wave Dark Matter and offer a short review of Wave Dark Matter phenomenology and constraints.

A reader who is familiar with General Relativity and Differential Geometry may skip sections 1.1-1.2, but the author highly suggests one familiarize with the content in these sections before advancing to the theoretical discussions in Chapter 2. Likewise, a reader who is familiar with Cosmology and the problem of Dark Matter can omit reading section 1.3. Nonetheless, sections 1.4-1.5 should be considered essential for any reading in order to develop the context required for the remainder of the thesis.

1.1 Notation, Mathematics, and Conventions

In the bulk of this thesis, we assume a working knowledge of differential geometry and differential equations. We will devote this section to describing our notation and conventions. Firstly, we will define our systems of units, as the equations contained in the remainder of the thesis depend on these. In following, we will develop the geometric language and notation which is used to describe spacetime in the theory of General Relativity; these descriptions are inspired by several texts which we highly recommend (18; 64; 61).

1.1.1 Units and Notation

We choose to use a unit system which is a combination of geometerized and natural units in order to simplify our equations and computations. This is achieved by taking fundamental physical constants which appear, the speed of light for instance, to have magnitude 1. Specifically, we take the scheme of $c = G = 1$. Mainly, this has the effect of simplifying our equations. We will reintroduce physical units when relevant - usually for comparison to physical data or when citing equations from other text. We list some common units and how to convert them to geometerized units in table 1.1. Other basic units can be converted by using a combination of the factors in the table. We provide the conversion of energy to length values in the table as an illustration, combining the factor for the mass to length conversion with that for the velocity conversion. In this unit system, values of mass, length, and time can be thought of as equivalent and inter-convertible. We choose to represent quantities in terms of length in table 1.1.

In addition to these conversions, it is sometimes useful to convert particle masses to their corresponding wavelength values. In terms of our equations, this amounts to taking the value of $\hbar = 1$ for the Klein-Gordon and Schrödinger equations. Denoting the spatial frequency (inverse wavelength) as Υ we have

$$m = \frac{\hbar \Upsilon}{c} \tag{1.1}$$

$$\frac{m}{10^{-22}eV} \approx \frac{\Upsilon}{3.45(ly)^{-1}} \tag{1.2}$$

Table 1.1: **Basic Unit Conversions:** We present some basic unit conversions. To make the specified conversion, multiply by the given factor. To make the reverse conversion, divide by the same factor.

Conversion	Factor	Value	Geometerized Value
Mass → Length	$\frac{G}{c^2}$	1 kg	$7.43 * 10^{-28}$m
Mass → Length	$\frac{G}{c^2}$	1 $M_\odot$	1477m
Time → Length	c	1 year	1 light year (ly)
Energy → Mass	c^{-2}	1eV	$1.783 * 10^{-36}$kg
Energy → Length	$\frac{G}{c^4}$	1eV	$1.324 * 10^{-63}$m
Velocity → Unitless	c^{-1}	$3 * 10^8 \frac{m}{s}$	1

1.1.2 Spacetime Geometry: Coordinates, Metrics, and Vector Fields

We pose equations in both coordinate-free and coordinate-dependent notation. We denote a set of coordinates at a point, x, as $\{x^\alpha\}$. The index α, in the context of a 4-dimensional spacetime is taken to have values $\alpha = 0, 1, 2, 3$, where 0 is usually chosen to represent a timelike index. Each coordinate system has a corresponding set of basis vectors $\{\mathbf{e}_\alpha|_\mathbf{x} = \frac{\partial}{\partial x^\alpha}|_x\}$. We will assume the Einstein summation convention where a repeated index implies a summation over the values of that index. A vector field, $\mathbf{V}(x)$, is then expressed in several equivalent ways as

$$\mathbf{V}(x) = v^\alpha(x)\mathbf{e}_\alpha|_\mathbf{x} = v^\alpha(x)\frac{\partial}{\partial x^\alpha}|_x = v^\alpha(x)\partial_\alpha|_x. \tag{1.3}$$

The functions $v^\alpha(x)$ are referred to as the *components* of the vector field and depend on the chosen coordinate system. Importantly, a vector field evaluated at a point x is a vector defined on the tangent space of that point. Vector fields give a formal notion of the directional derivative of a function. The derivative of a function, f, in the direction of a vector field, $\mathbf{X}$, is usually expressed as

$$\mathbf{X}(f)|_x = v^\alpha(x)\partial_\alpha f|_x. \tag{1.4}$$

A spacetime manifold comes equipped with a Lorentzian metric, $\mathbf{g}$. We choose

the $(-,+,+,+)$ convention for the metric's Lorentz signature. At a point, the metric defines a non-degenerate bilinear product between vectors as

$$\mathbf{g}(\mathbf{v},\mathbf{w})|_x = \langle \mathbf{v},\mathbf{w}\rangle_x = v^\alpha w_\alpha = g_{\alpha\beta}(x) v^\alpha w^\beta. \tag{1.5}$$

Here, the components of the metric are defined with respect to a the coordinate basis vectors $g_{\alpha\beta}(x) = \mathbf{g}(\partial_\alpha|_x, \partial_\beta|_x)$. The metric gives rise to the notion of *lowering* indices for vectors and tensors, where $v_\alpha = g_{\alpha\beta} v^\beta$. Likewise, the metric inverse, denoted with superscripts as $g^{\alpha\beta}$, can *raise* an index as $v^\alpha = g^{\alpha\beta} v_\beta$.

A vector with a lowered index is sometimes referred to as a *co-vector* or *dual vector*. This is due to the one-to-one correspondence between vectors and co-vectors that is established by the metric. Given a vector, $\mathbf{v}$, there always exists a co-vector $\tilde{\mathbf{v}}$ defined as $\tilde{\mathbf{v}} = \mathbf{g}(\mathbf{v}, -)$. The co-vector defines a mapping taking vectors to scalars, $\tilde{\mathbf{v}}(\mathbf{w}) = \mathbf{g}(\mathbf{v},\mathbf{w})$. Analogous to vector fields, one can define co-vector fields otherwise known as *one-forms*. Given a vector field, $\mathbf{V}$, its corresponding one-form can be expressed in the following equivalent ways

$$\tilde{\mathbf{V}}(x) = \mathbf{g}(\mathbf{V}, -) = g_{\alpha\beta} v^\beta dx^\alpha = v_\alpha dx^\alpha = v_\alpha(x)\tilde{\mathbf{e}}^\alpha. \tag{1.6}$$

Here we have introduced the basis one-forms $dx^\alpha = \tilde{\mathbf{e}}^\alpha$ which are defined in relation to the basis vectors as $dx^\alpha(\partial_\beta) = \delta^\alpha_\beta$.

Lastly, we can define tensors in spacetime by using the basis one-forms. We define a rank N tensor as a map which converts N vectors into a scalar. The metric tensor, for example, is a realization of a rank 2 tensor.

$$\mathbf{g} = g_{\alpha\beta} dx^\alpha \otimes dx^\beta \tag{1.7}$$

$$\mathbf{g}(\mathbf{v},\mathbf{w}) = g_{\alpha\beta} dx^\alpha(\mathbf{v}) dx^\beta(\mathbf{w}) \tag{1.8}$$

Lastly, a generic rank N tensor, $\mathbf{S}$, is expressed as

$$\mathbf{S} = S_{\alpha_1,\alpha_2,\ldots\alpha_N} dx^{\alpha_1} \otimes dx^{\alpha_2} \otimes \ldots \otimes dx^{\alpha_N} \tag{1.9}$$

We note that it is also possible to define rank (N, M) tensors which have N subscripts and M superscripts. In this case the tensor receives N vectors and M co-vectors as inputs and the M superscript components correspond to the basis vectors.

1.1.3 Spacetime Geometry: Levi Civita Connections

In the context of differential geometry a manifold's *connection*, denoted ∇, is a fundamental object which is used to relate the manifold's many different tangent spaces. Loosely speaking, the connection allows one to compare vectors which exist in the tangent space of one point to vectors which exist in the tangent space of another. Further, this allows one to formalize the notion of the differentiation of vector fields as well as tensor fields. A Kozsul Connection for vector fields is denoted as $\nabla(\mathbf{V}, \mathbf{W}) = \nabla_{\mathbf{V}}\mathbf{W}$, and can be thought of as "the covariant derivative of $\mathbf{W}$ in the direction of $\mathbf{V}$." ∇ must satisfy the following properties to be considered a connection:

$$\nabla_{f\mathbf{V}}\mathbf{W} = f\nabla_{\mathbf{V}}\mathbf{W} \tag{1.10}$$

$$\nabla_{\mathbf{V}}(f\mathbf{W}) = \mathbf{V}(f)\mathbf{W} + f\nabla_{\mathbf{V}}\mathbf{W} \tag{1.11}$$

$$\nabla_{\mathbf{V}+\mathbf{U}}\mathbf{W} = \nabla_{\mathbf{V}}\mathbf{W} + \nabla_{\mathbf{U}}\mathbf{W}. \tag{1.12}$$

Every connection is associated with a set of *connection coefficients*, often referred to as Christoffel Symbols. In our notation, the Christoffel symbols are expressed as

$$\Gamma_{ijk} = \langle \nabla_{\partial_i}\partial_j, \partial_k \rangle . \tag{1.13}$$

For a given manifold, there are many possible connections which satisfy the above properties. However, there is a particular connection which can be uniquely defined in terms of the metric which is referred to as the *Levi-Civita Connection*, ∇^{LC}. The Levi-Civita connection is the unique connection which satisfies two additional properties: it is *torsion free* and *metric compatible*. These properties are stated respectively through the following tensoral relations:

$$\mathbf{T}(\mathbf{X}, \mathbf{Y}) = \nabla^{LC}_{\mathbf{X}}\mathbf{Y} - \nabla^{LC}_{\mathbf{Y}}\mathbf{X} - [\mathbf{X}, \mathbf{Y}] = 0 \tag{1.14}$$

$$\mathbf{M}(\mathbf{X},\mathbf{Y},\mathbf{Z}) = \mathbf{X}(\langle \mathbf{Y},\mathbf{Z}\rangle) - \left\langle \nabla^{LC}_{\mathbf{X}}\mathbf{Y},\mathbf{Z}\right\rangle - \left\langle \mathbf{Y},\nabla^{LC}_{\mathbf{X}}\mathbf{Z}\right\rangle = 0. \tag{1.15}$$

Here we identify the torsion tensor, $\mathbf{T}$ and the metric compatability tensor, $\mathbf{M}$. This leads to the unique formula for the connection coefficients of ∇^{LC}

$$\Gamma^{LC}_{ijk} = \frac{1}{2}\left(\partial_k g_{ij} + \partial_j g_{ik} - \partial_i g_{jk}\right). \tag{1.16}$$

The study of manifolds equipped with the Levi-Civita connection encompasses a significant portion of the field of Differential Geometry. As well, the structures of General Relativity are usually formulated with respect to the Levi-Civita connection. Later, in Chapter 2, we will discuss the some of the implications of relaxing the torsion-free condition of eq. 1.14 in the context of General Relativity and show that this leads to a geometric interpretation of the Einstein-Klein Gordon Equations.

1.1.4 Spacetime Geometry: General Properties of Connections

To each connection, ∇, one can associate several tensoral quantities. In addition to the torsion and metric compatibility tensors in eqs. 1.15 and 1.14, any two connections differ by a tensoral relation. In the case of the difference from the Levi-Civita connection, one defines the *difference tensor* as:

$$\mathbf{D}(\mathbf{X},\mathbf{Y},\mathbf{Z}) = \langle \nabla_{\mathbf{X}}\mathbf{Y},\mathbf{Z}\rangle - \left\langle \nabla^{LC}_{\mathbf{X}}\mathbf{Y},\mathbf{Z}\right\rangle \tag{1.17}$$

Each connection is associated to a characteristic set of curves referred to as *geodesics*. Geodesics are the generalization of the concept of a"straight-line" on an otherwise curved manifold. Formally, geodesics are auto-parallel curves which can be found via solving the following differential equation posed in local coordinates:

$$\frac{d^2x^\alpha}{d\tau^2} = -\Gamma^\alpha_{\beta\gamma}\frac{dx^\beta}{d\tau}\frac{dx^\gamma}{d\tau}. \tag{1.18}$$

Lastly, the *Curvature Tensor* provides a description of how adjacent geodesics

deviate as a result of the manifold's curvature.

$$\mathbf{R}(\mathbf{X},\mathbf{Y})\mathbf{Z} = \nabla_{\mathbf{X}}\nabla_{\mathbf{Y}}\mathbf{Z} - \nabla_{\mathbf{Y}}\nabla_{\mathbf{X}}\mathbf{Z} - \nabla_{[\mathbf{X},\mathbf{Y}]}\mathbf{Z} \tag{1.19}$$

More commonly, one forms the *Riemann Curvature Tensor* as

$$\mathbf{Riem}(\mathbf{X},\mathbf{Y},\mathbf{Z},\mathbf{W}) = \langle \mathbf{R}(\mathbf{X},\mathbf{Y})\mathbf{Z},\mathbf{W}\rangle\,. \tag{1.20}$$

One then defines the *Ricci Curvature* and *Scalar Curvature*, which are used in General Relativity, as:

$$\mathbf{Ric}(\mathbf{X},\mathbf{Y}) = g^{ij}\mathbf{Riem}(\mathbf{X},\partial_i,\mathbf{Y},\partial_j) \tag{1.21}$$

$$R = g^{ij}\mathbf{Ric}(\partial_i,\partial_j) \tag{1.22}$$

Importantly, to every connection one may associate such curvature quantities; only for the Levi-Civita connection will these quantities result in formulae which are solely determined by the metric.

1.2 General Relativity

In this section we detail the theory of General Relativity using the geometric language developed in section 1.1. General Relativity (GR) is a classical and geometric description of the gravitational interaction which was developed by Albert Einstein, and first published in 1915 (23). GR describes our universe as a 4-dimensional manifold referred to as a spacetime. Spacetime comes equipped with a *Lorentzian* metric, $\mathbf{g}$, and the Levi-Civita connection ∇^{LC}. Our convention for the Lorentzian signature will be to take the time component as negative in the $(-,+,+,+)$ format. The equations of GR are referred to as the Einstein Field-Equations (EFEs). Even more fundamentally, the EFEs can be thought of as the critical point of the Hilbert action - this discussion is deferred to Chapter 2. In tensoral form, the EFEs appear as

$$\mathbf{G} + \Lambda\mathbf{g} = 8\pi\mathbf{T} \tag{1.23}$$

This set of equations relates the Einstein Curvature, **G**, to the spacetime's Stress-Energy (SE) tensor, **T**. Put simply, the SE tensor encodes the distribution and dynamics of the matter and energy contents of spacetime. In other words, one can understand the functionality of the EFEs in the sense that matter generates a SE which equates to a curvature in spacetime. This curvature is then associated with a characteristic set of geodesics which are interpreted as the free-falling paths of "test particles" in spacetime; the curving of these paths as a result of the SE tensor is what one thinks of as "gravity." In other words, the essence of GR lies in the statement "Matter curves spacetime and spacetime curvature results in gravity."

The assumption that spacetime comes equipped with the Levi-Civita connection in GR is just that, an assumption. That being said, it is a highly convenient assumption as it allows all of the quantities of the EFEs to be expressed in terms of the metric and its derivatives, greatly simplifying the theory. Alternative GR-like theories have been considered in which the spacetime connection is not necessarily the Levi-Civita one. These theories relax the conditions imposed on the connection, namely the conditions on the torsion and metric compatibility tensors in eqs. 1.14 and 1.15. For instance, Einstein-Cartan theory removes the Torsion-free condition of eq. 1.14. Among other motivating features, Einstein-Cartan theory (89) has been considered as a means of including the intrinsic spin of matter-fields into GR. Later, in chapter 2 we will consider a similar type of theory which relaxes the same torsion condition, resulting in a geometric motivation for the theory of Scalar Field Dark Matter.

1.2.1 Phenomena in GR

In GR, spacetime curvature can result in a plethora of gravitational phenomena. Importantly, most of these phenomena are unique to GR in comparison to Newtonian theory and have been confirmed observationally. A few such phenomena include: gravitational lensing, gravitational redshift, frame-dragging effects, orbital precession, the formation of black holes, and gravitational waves. All of these effects result from the spacetime curvature predicted by GR. Einstein first proposed GR

as an explanation for the anomalous precession of Mercury's orbit in another 1915 paper (22), noting that the theory agreed closely with the known precession rate. In addition, he also proposed that the curvature produced by massive celestial bodies would cause the deflection of passing rays of light. This effect was first observed and confirmed in 1919 by Eddington (21), who measured the deflection of light around the sun during a total solar eclipse.

Orbital precession and the deflection of light can be explained by making adjustments to standard Newtonian theory. Arguably, these adjustments usually result in more issues than the ones they intend to solve. The gravitational redshift, frame-dragging, and non-linear gravitational wave phenomena are truly unique to GR and cannot be explained by such ad-hoc adjustments. Einstein argued in 1907 that light would experience a Doppler-like redshift when moving through strong gravitational fields. This gravitational redshift was first measured in the vicinity of a white dwarf by Popper in 1954 (67). Frame-dragging effects result from the distortion of spacetime by rotating massive bodies. Lense-Thirring precession and the Geodetic effect are the two most prominent such effects. Geodetic precession has been measured in the vicinity of the Earth by the Gravity Probe B experiment (33) while Lense-Thirring precession has yet to be accurately measured. Lastly, the motion of massive bodies through space can generate ripples in spacetime which propagate at light speed, referred to as gravitational waves. Gravitational waves were directly detected for the first time in 2016 by LIGO, which detected the waves resulting from a binary black hole merger (32).

The admittance of black holes is a unique feature of GR. Mathematically, black holes are described by solutions to the vacuum ($\mathbf{G} = 0$) Einstein Equations. The vacuum equations admit two types of black hole solutions, static solutions giving the Schwarzchild black hole, and stationary solutions giving the rotating Kerr black hole. Black holes are characterized by their event horizon, a boundary at which gravity becomes so strong that even light speed particles cannot escape. Importantly, direct observation of black holes has been achieved recently in 2017 by the Event Horizon Telescope (EHT), pioneering a new era of observational cosmology and black hole

physics (16).

1.3 Modern Cosmology: ΛCDM

The most successful theory of cosmology to date is referred to as Λ Cold Dark Matter cosmology, or ΛCDM. In ΛCDM, the universe is described as a spacetime manifold which obeys the Einstein Equations as described in section 1.2. In short, the Stress-Energy content of the universe consists of five main components: Baryonic Matter (BM), Cold Dark Matter (CDM), Dark Energy (DE), Electromagnetic Radiation, and Neutrinos. The behavior and interactions of these components with each other and with the Einstein Equations then determines the evolution of the universe.

The term "Baryonic Matter," refers to all types of matter which consist of protons and neutrons. More specifically, a baryon is a composite particle with an odd number of valence quarks. In the cosmological context, matter consisting of electrons is also included, though electrons are not baryons in a strict sense. As such, all types of atoms and molecules are considered part of the universe's BM content. This BM content interacts via electromagnetism, and can therefore be observed via its interactions with light. In other words, BM is *visible*. The term "Dark Matter" is used somewhat in compliment to refer to types of matter which are specifically non-baryonic. Importantly, DM is assumed to lack electromagnetic interactions. As a result, DM cannot be detected via interactions with light, hence it is *dark*. Though DM is not visible, it is observable, specifically via its contributions to gravity. Whether or not DM shares interactions with the Strong and Weak Nuclear forces is often considered in ΛCDM, but remains an open question.

The character Λ in ΛCDM is chosen to represent the cosmological constant. The cosmological constant appears as a constant term in the Einstein Equations, contributing a constant energy density at all spatial points referred to as Dark Energy. At the level of the Stress-Energy tensor, Dark Energy contributes an everywhere negative pressure; this pressure is the source of the accelerating expansion of the universe. This phenomena was experimentally confirmed in 1998 by two independent groups (66; 69), solidifying the necessity of the cosmological constant in ΛCDM.

Moreover, modern studies of ΛCDM estimate Dark Energy to be the dominant energy component of the present day universe, comprising 68% of its total energy content. Though Electromagnetic Radiation and Neutrinos comprise a small amount of the total energy content of the present day universe ($< 1\%$), their dynamics in the early universe are crucial to the ΛCDM model. In fact, the early universe contains a period in which Electromagnetic Radiation comprised the majority of the universal energy content.

1.3.1 The FLRW Model

The largest scale features of the universe and its energy components can be modelled under the assumption that they are homogeneous and isotropic. This is observationally valid at the largest observed scales ($\sim$ 260Mpc) (95). The equations which govern the expansion of spacetime and the evolution of its energy components are referred to as the Friedmann equations. For the ΛCDM model, the metric is referred to as the Friedmann-Lemaitre-Robertson-Walker (FLRW) metric, and appears in line element form as

$$ds^2 = -dt^2 + a(t)\left(\frac{dr^2}{1-kr^2} + r^2 d\theta^2 + r^2 \sin^2\theta d\phi^2\right) \tag{1.24}$$

The function $a(t)$ is referred to as the "scale factor" of the universe, describing the spatial expansion of the universe in time. The value of k is referred to as the *spatial curvature*. In the case that $k = 0$, the universe is spatially flat at the largest scales. Positive and negative values of k likewise correspond to cosmologies which are "closed" or "open" respectively. Qualitatively, if one omits the cosmological constant, a universe with positive k will expand from a point, eventually reach a maximum spatial size and then re-contract back to a point. Likewise, an open universe with $k < 0$ is expected to expand indefinitely at an increasing rate. Lastly the spatially flat case, $k = 0$, the universe expands forever at a decreasing rate. Including the cosmological constant, a flat universe will share the same fate as an open one and expand forever, while a closed universe will still re-contract if Λ remains sufficiently

small. Most modern observations, those by the Planck collaboration for instance (15), suggest that the universe is spatially flat with $k = 0$ being consistent with data. This value now faces tension with recent measurements, which suggest a small but positive value for k (92).

Assuming that the SE tensor is homogeneous and isotropic and that the metric is of the FLRW form in eq. 1.24, the Einstein Equation can be evaluated to obtain the two Friedmann equations

$$H(t)^2 = \frac{8\pi\rho + \Lambda}{3} - \frac{k}{a^2} \tag{1.25}$$

$$\dot{\rho} = -3H(t)(\rho + p). \tag{1.26}$$

Here we have introduced the *Hubble constant*, $H(t) = \frac{\dot{a}}{a}$, which describes the relative expansion rate of space. The density and pressure components of the SE tensor are respectively expressed as ρ and p. A component's "equation of state" relates its pressure and density as $p = w\rho$, and is usually just specified by the value of w. Most cosmological parameters are expressed in terms of the *critical density*, ρ_c, which is defined as the threshold density for a universe with $\Lambda = 0$ such that $k = 0$. This can be found using eq. 1.25 as $\rho_c = \frac{3H^2}{8\pi}$. The energy density, ρ is decomposed into its various contributions from baryonic matter, DM, DE, and radiation

$$\frac{\rho}{\rho_c} = \Omega_{BM} + \Omega_{DM} + \Omega_\Lambda + \Omega_R. \tag{1.27}$$

Here, each Ω parameter is defined as the fraction of the corresponding density component to the critical value. That is, $\Omega_x = \frac{\rho_x}{\rho_c}$. Substituting this definition into the first Friedmann equation in eq. 1.25, and defining the "curvature contribution" as $\Omega_k = -\frac{k}{H^2a^2}$ returns the following

$$1 = \Omega_M + \Omega_{DM} + \Omega_\Lambda + \Omega_R + \Omega_k. \tag{1.28}$$

The contributions excluding Ω_k are sometimes combined into a single parameter Ω.

The value of Ω, representing the contributions of all matter and energy content, directly determines whether or not the universe is spatially closed, flat, or open, determined by $\Omega > 1$, $\Omega = 1$ and $\Omega < 1$ respectively. Since the Hubble parameter as the well density components are time dependent, the Ω_x parameters in eq. 1.28 are as well. It is common practice to evaluate these parameters based on their present day values, denoted by appending a subscript of 0.

Further than the homogeneous and isotropic features of the Friedman equations, the ΛCDM paradigm has been used to model the largest cosmological substructures including the galactic filaments and the cosmic microwave background (CMB). These features have been observed by collaborations such as the Planck collaboration and WMAP. In the modern day, simulations such as Illustris (26), EAGLE (86), and CAMB (1) model these features to a high degree of precision. Going further, the smallest cosmological structures (those of galaxies and galactic substructure), are intimately related to the problem of Dark Matter, described in the following section.

1.3.2 What is Dark Matter?

The notion of "Dark Matter," can be historically traced to a lecture series given by Lord Kelvin in 1884 (87). Kelvin argued that measuring a galaxy's luminosity distribution alone was an insufficient method for determining that galaxy's gravitational mass. Put more formally, Kelvin noticed that the velocities of stars in the Milky Way were too disperse to be accounted for by only considering the gravity generated by the galaxy's luminous mass distribution. Accordingly, Kelvin supposed the existence of "Dark Bodies" to account for this discrepancy. These "Dark Bodies," hypothesized to be some form of non-luminous matter, would then account for the additional gravity required to generate the orbital velocities observed in the Milky Way.

The term "Dark Bodies" evolved to be the term we use today (Dark Matter) in 1933 in a work regarding the Coma Cluster, fig. 1.1, by Fritz Zwicky (88). Zwicky measured the relative velocities of the cluster's galaxies as well as their inferred luminous mass. Famously, this led to the conclusion that these velocities were too great

FIGURE 1.1: **Coma Cluster:** The Coma Cluster, imaged above by (2), is a cluster with over 1000 identified galaxies. Zwicky reported that the mass of the cluster as computed by the virial theorem was over 400 times of that inferred from luminosity measurements. It was argued that the additional unmeasured mass of the cluster must be in the form of non-luminous or "dark" matter.

to be sustained by the luminous mass of the galaxy alone; in order for the cluster to be virialized or self-bound, additional non-luminous mass would be required. Zwicky hypothesized the existence of such mass, referring to it as "Dunkle Materie" (Dark Matter). As such, the search for this Dark Matter and what it could be composed of continues to the present day.

Throughout the 20th century, advances in observational astronomy have enabled more precise measurements of stellar velocities, luminous mass, and gravitational mass. Ultimately, this has led to further data and evidence for Dark Matter. For instance, the advent of 21cm spectroscopy allowed increasingly precise measurements of stellar velocities (31). This advance was utilized in 1978 by Rubin and Ford who measured the flatness of galactic rotation curves, a remarkable evidence for dark

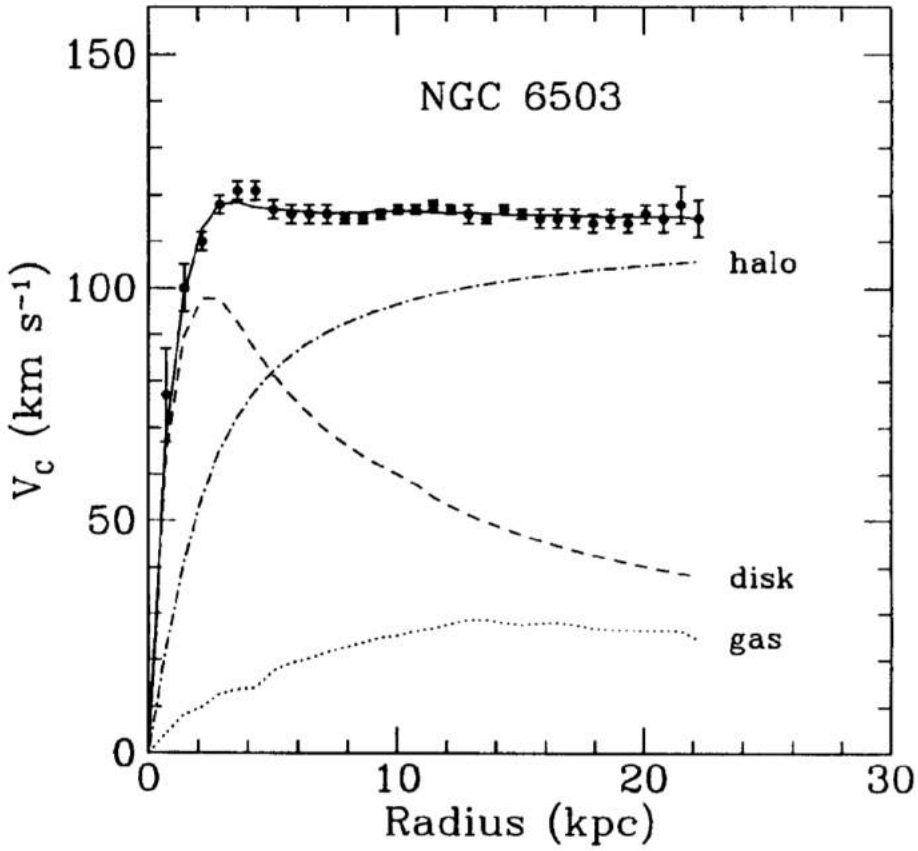

FIGURE 1.2: **Rotation Curves:** An example rotation curve from the circular orbits of galaxy NGC 6503 (34). Observed data given with error bars; the inferred contributions from the Dark Matter halo, stellar disk, and gaseous mass are shown. Dark Matter is the primary contribution. Contributions from the disk and gas display decreasing velocity at large distances; the presence of Dark Matter flattens the curve.

matter (71). By measuring the orbital velocities of stars within the spiral galaxies, it was inferred that Dark Matter was about 6 times more abundant than luminous matter. Shown in fig. 1.2, the flattening of galactic rotational velocity curves is a strong indicator of the presence of Dark Matter in galaxies. Still, the composition of Dark Matter and what types of objects it consists of, remains unknown.

Theoretical progress such as the founding of General Relativity has also increased the capability to test the Dark Matter hypothesis. As an example, the FLRW model of cosmology has been used in conjunction with measurements of the Cosmic Mi-

FIGURE 1.3: **Bullet Cluster:** The Bullet Cluster, imaged by Chandra (55), is made of two colliding clusters of galaxies. The inferred distributions of Dark Matter and Baryonic Matter are shown in blue and red respectively. The collision has resulted in a large offset between the two types of matter. The baryonic matter is slowed via frictional forces while the Dark Matter is not, resulting in the separation.

crowave Background (CMB) to place constraints on the abundance of Dark Matter. For instance, the 2012 WMAP results imply that Dark Matter composes 24% of the energy content of the universe (25). Further, analyses of relativistic phenomena like gravitational lensing and redshifting provide a means to investigate more localized features of Dark Matter.

A possible alternative to the existence of Dark Matter lies in theories of Modified Gravity. These theories suppose our understanding of the gravitational force to be insufficient to explain the orbital dynamics observed in galaxies. In this view, one supposes a different form for the gravitational force law to account for the discrepancies usually attributed to Dark Matter. Some such theories include "Modified Newtonian Dynamics" and "$f(R)$ gravity" (74; 82). These types of theories now face strong tension with modern observations like Chandra's observation of the Bullet Cluster. Shown in fig. 1.3, Chandra infers a significant offset between the luminous center, and gravitational center of the Bullet Cluster merger, casting doubt on

Modified Gravity theories and further suggesting the existence of some form of Dark Matter (56; 14).

1.3.3 Dark Matter Candidates

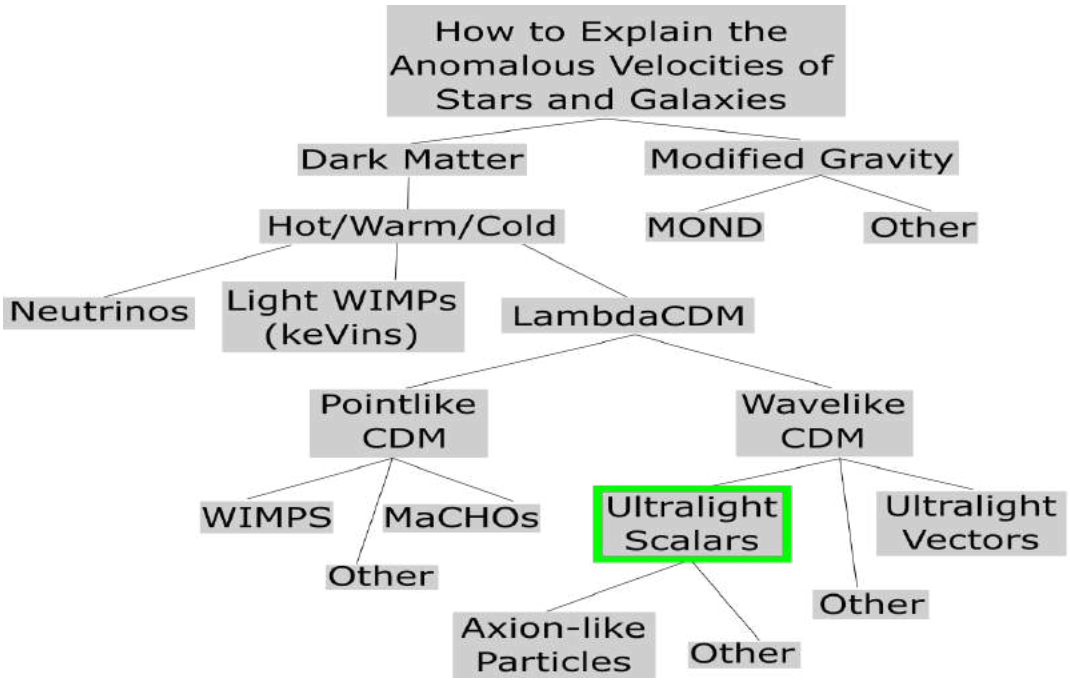

FIGURE 1.4: **DM Candidates:** The problem of DM arises as an effort to explain anomalously large velocities of stars and galaxies. DM arises as a way to explain this motion without changing the gravitational force laws of General Relativity. Cold DM has become the dominant candidate; Hot DM and Warm DM are usually ruled out as they inhibit the formation of galactic scale structure. We make a further dichotomy between Point-like particles and wave-like particles. Candidates for Wave DM include ultralight particles such as ultralight scalars. Point-like DM comprises the majority of traditional DM models, treated with N-body gravity.

In the modern context, "Dark Matter" (DM), refers to a hypothetical form of matter which does not interact via the electromagnetic force but still has gravitational mass. As described, one cannot "see" DM, though one can observe its interactions with other astronomical masses via gravity. Theories of what types of matter or what particles could constitute DM vary, resulting in a myriad of possibilities. Fig. 1.4 presents major categories of DM candidates tailored towards the discussions of this thesis.

The Hot, Warm, and Cold distinction refers to the velocities of DM particles. Hot DM candidates are usually light, weakly interacting particles like neutrinos with relativistic velocities. Theories in which hot DM comprises the majority of DM mass face issues in regards to forming galactic scale structure. This is due to the hot particles having a large free streaming length, resulting in a reduction of structures at the observed galactic scale. In other words, hot DM reduces small scale structure as desired but has the cost of preventing galaxy formation; this often receives the title of the "Catch-22" problem of hot DM. Warm DM, usually thought to consist of weakly interacting particles of a slightly greater mass range than hot DM, faces a similar Catch-22 problem. Cold DM refers to DM particles with low velocity and therefore insignificant free-streaming lengths. Cold DM theories are generally consistent with the observed growth of cosmological structure and are therefore the most strongly favored descriptions of DM in the field of cosmology. We note that more complex DM theories involving mixtures of mostly cold DM and small amounts of warm or hot DM could also be compatible with observation. This is an appealing choice in scope of the large variety of hypothetical DM candidates, but introduces additional difficulties in terms of modelling DM physics (finding the correct mixture proportions for instance). For a more comprehensive review of the Hot, Cold, Warm distinction we refer the reader to (68).

For this thesis, we suggest a further distinction between point-like and wave-like cold DM. Point-like CDM candidates include objects which can be treated as collisionless point particles on galactic and cosmological scales. Point-like CDM candidates include Weakly Interacting Massive Particles (WIMPs), hypothetical particles in the ~ 100 GeV mass range, and Massive Compact Halo Objects (MaCHOs), large and dim objects like black holes or non-luminous stars. MaCHOs are usually ruled out as a DM candidate as they are expected to generate an abundance of gravitational lensing events which have not been observed (4). WIMPs remain the most promising candidates for point-like CDM. Standard values for interaction cross section and particle mass at the scale of the weak interaction are able to produce particles with the same modern abundance as expected for DM. This is often referred

to as the "WIMP Miracle." For a review on WIMPs we suggest (54). Importantly, direct detection efforts for WIMPs have, to date, provided no significant evidence for their existence (77). Therefore, despite the success of the WIMP theory, alternative DM candidates must be considered given the lack of WIMP detection events.

Wavelike particles refer to a class of CDM candidates with cosmologically relevant wavelengths. As such, their wave dynamics must be resolved in cosmological simulations. Candidates for wavelike particles are usually ultralight particles, around the 10^{-22}eV range for ultralight scalars. Wavelike DM particles display unique coherence effects at galactic scales which are relevant in regards to structure formation. This thesis specifically considers the case of ultralight scalar fields. We defer a more detailed description of wavelike DM to section 1.4.

1.3.4 Small-Scale Crises of ΛCDM

ΛCDM faces several issues in regards to modelling structure at galactic length scales. These issues are often grouped and referred to as the "small-scale crisis" of ΛCDM. Specifically, simulations of point-like CDM are associated with the Cusp-Core problem, the Too-big-to-fail problem, and the Missing Satellites problem. The Cusp-Core problem is the direct result of N-body simulations of DM halos. These types of simulations display DM halos which tend towards singular density, cuspy cores. This halo profile was first demonstrated in N-body simulations by Nevarro, Frenk, and White in 1996 and is thus referred to as the NFW profile (63). Writing the functional form of the NFW profile, it is clear that it is cuspy and singular at the origin.

$$\rho_{NFW}(r) = \frac{\rho_0}{\frac{r}{r_s}(1+\frac{r}{r_s})^2} \tag{1.29}$$

The Too-big-to-fail (TBTF) problem and missing satellites problem (MSP) are similar in that they regard the expected distribution of satellite galaxies for larger galaxies like the Milky Way. The MSP gets its name from a discrepancy between the observed number of galaxies satellite to the Milky Way and the number of these satellite predicted by traditional ΛCDM. In other words, ΛCDM predicts more satellites

than are observed, hence the satellites are "missing." A commonly proposed resolution to the MSP is that the missing satellites do exist, but that they do not host luminous matter components and are therefore not visible. The MSP can then, hypothetically, be resolved by a careful consideration of detection efficiency and counting statistics. In other words, if one provides a model for the connection of luminous matter to DM halos, then that model can be used to make inferences about how many satellites should actually be observable with a given detector. It was shown in (46) that this method can resolve the MSP, and in some cases push the problem towards the case of "too many satellites." Importantly, a detailed understanding of DM dynamics and how they affect the connection to luminous matter will help determine the viability of such resolutions. The TBTF problem, somewhat similar but still distinct from the MSP, also regards a lack of Milky Way satellites but at higher masses than those of the MSP. Specifically, these massive satellites are so large that they are expected to host luminous matter with high probability. The name "TBTF" then comes from the notion that such large satellites would be "too big to fail to be luminous." Again, it has been suggested that the TBTF problem results from a lack in understanding of how the dynamics of baryons or DM could affect the observed distribution of galaxies. It can be argued that baryonic effects are insufficient to fully resolve this problem. However, a recent suggestion in (65) argues that the TBTF problem is the result of a naive misinterpretation of satellite statistics, and that the observed satellite counts are consistent with the simulations Illustris and EAGLE.

1.4 Scalar Field Wave Dark Matter

1.4.1 What is Scalar Field Wave Dark Matter?

In this thesis we will focus on a theory of DM in which DM is represented by a scalar field with an ultralight mass parameter (around $m = 10^{-22}$eV). Importantly, the small mass of the scalar results in an extremely large wavelength (around 1kpc for most cases). As a result, the DM exhibits unique wave-like features which can be relevant on galactic and cosmological scales. Theories regarding such ultralight

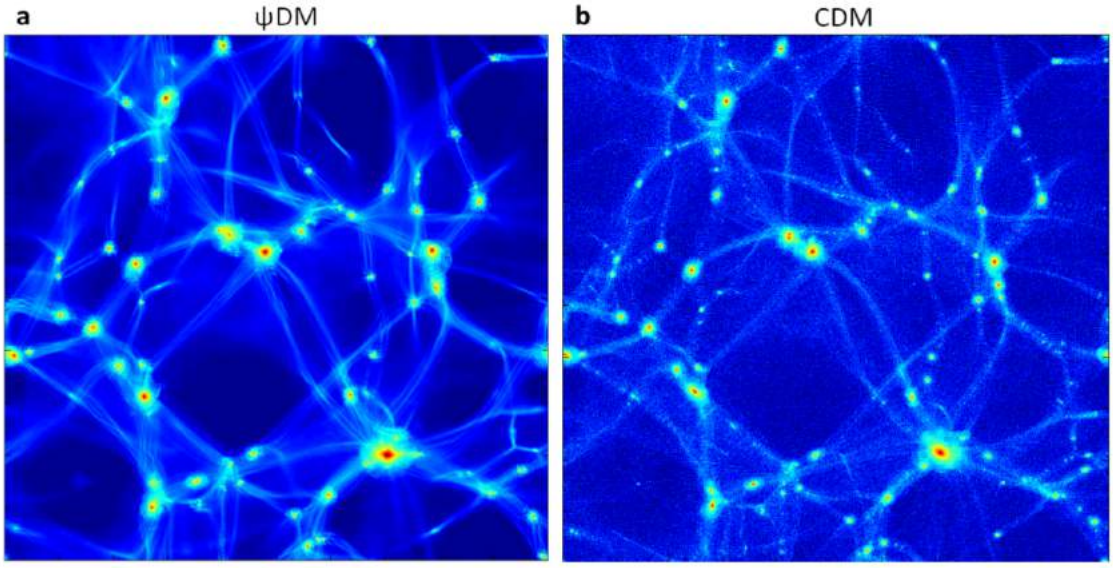

FIGURE 1.5: **ψDM Galactic Filaments:** An example of the galactic filaments as modelled by SFψDM and particle CDM taken from Schive (75). ψDM results in coherent wavelike features which result in a reduction of the smallest scales of structure formation, seen as the lack of granularity in the left picture. SFψDM forms a condensate structure on the largest scales that is otherwise similar to usual ΛCDM.

scalars have been given many names: Fuzzy Dark Matter (FDM), Axion Dark Matter (ADM), Bose-Einstein Condensate Dark Matter (BECDM), and Scalar Field Dark Matter (SFDM) being a few of them. FDM, one of the most popular labels, was coined by Hu to highlight the ultra-dispersed nature of the scalar field as a result of its large wavelength, hence "Fuzzy" (41). ADM respects motivations from particle physics in which the ultralight scalar corresponds to the QCD Axion, a particle which has been investigated outside of DM contexts in interest of solving the strong CP problem (93). The name BECDM comes from the tendency of the scalar field to form a cosmic scale Bose-Einstein condensate with superfluid properties (85; 51). Lastly, SFDM directly respects the representation of DM as a scalar field.

In these cases, DM is usually described by either the Einstein-Klein-Gordon equations (below) or their non-relativistic analogs, the Poisson-Schrödinger equations.

$$\mathbf{G} + \Lambda\mathbf{g} = 8\pi\mathbf{T}_{\phi} \tag{1.30}$$

$$\Box\phi = m^2\phi \tag{1.31}$$

It is their galactic scale, wavelike features that gives these theories their unique character in comparison to other DM theories. We choose to use the name Wave Dark Matter (ψDM) in homage to these wave features. Further, we note that the name ψDM does not strictly require DM be represented by a scalar field; one could consider some other type of ultralight matter field such as a vector or tensor. In the most specific sense, this thesis describes a theory of ψDM which contains a single ultralight scalar field, ***Scalar Field Wave Dark Matter*** (SFψDM). Interestingly, apart from its wavelike features, SFψDM resembles usual ΛCDM at large scales, shown in fig. 1.5.

1.4.2 Cosmological Axions

One way to motivate the theory of SFψDM lies in the interpretation of DM particles as axion-like particles. (57) provides a comprehensive review of Axion Cosmology; we follow this review to provide a basic introduction to the topic. Axion-like particles have been studied at a vast range of particle masses from the ultralight 10^{-33}eV regime all the way to the regime of the QCD axion at 10^{-6}eV. Axion-like particles are so named for their similarity to the QCD axion, a particle which could solve the strong CP problem of QCD. The axion is introduced as a Goldstone boson for a massless complex scalar, χ. Via some form of spontaneous symmetry breaking, the Peccei-Quinn mechanism being a popular choice, the complex scalar takes on its vacuum expectation value (vev), $\langle\chi\rangle$, and can be decomposed into this vev and an angular argument as $\chi = \langle\chi\rangle e^{i\phi/f}$. The angular field, ϕ, is the real-valued axion field and f is referred to as the "axion decay constant." To all orders of perturbation theory, the axion as a goldstone boson is massless. However, at some energy scale, non-perturbative effects can induce a potential and therefore a mass for the axion. Importantly, since the axion is an angular variable, this potential must be periodic. A basic, but certainly not unique representation of the axion potential can be expressed

as

$$V(\phi) = \mu^4 \left(1 - cos(\frac{\phi}{f})\right). \tag{1.32}$$

Here, the value of μ is determined by some form of non-perturbative physics and will depend on the given axion model. To lowest order in ϕ, the axion potential becomes the usual potential of a massive real scalar, $V(\phi) \approx \frac{1}{2}m^2\phi^2$. Here we have the defined the axion mass as $m^2 = \frac{\mu^4}{f^2}$. Terms which are order ϕ^4 and higher describe axion self-interactions. Importantly, higher order interactions of ϕ are further suppressed by the decay constant f, resulting in increasingly small coupling constants. At many scales these couplings can be neglected, though at large cosmological scales they may become relevant towards DM structure formation (noted by (83)). Assuming that matter-radiation inequality occurs at a temperature of order $\sim$ 1eV (as expected from observation), the decay constant can be estimated as $f \sim 10^{17}$ GeV, which is close to the energy scale of Grand Unified Theories of particle physics. At this scale of decay constant, mass values of $m \sim 10^{-22}$eV result in DM relic abundances near the observed value. This is a rather convenient coincidence and has been likened to the WIMP miracle. Citing (42), this abundance can be expressed as

$$\Omega_{DM,0} \sim 0.1(\frac{f}{10^{17}GeV})^2(\frac{m}{10^{-22}eV})^{1/2}. \tag{1.33}$$

In a Friedmann universe with a Hubble constant H, the equation of motion for the scalar field can be written as

$$\ddot{\phi} + 3H\dot{\phi} + m^2\phi = 0. \tag{1.34}$$

For early times such that $m^2 << H$, the field oscillations are damped by the Hubble expansion of the universe. The equation of state at these early times is $w = -1$, allowing DM to contribute to the Hubble expansion. As the universe cools and H continues to decrease, the axion field will begin to oscillate and behave as a condensate, obeying the field's classical equations of motion. In this cooling period

the equation of state transitions from $w = -1$ to values which oscillate around $w = 0$. If the universe becomes DM dominated early enough when w is negative, the scalar field can contribute significantly to the expansion of the universe. Later, when $w = 0$ and the scalar field is oscillating, the field behaves as cold cosmological dark matter with a time averaged pressure of 0. When the mass value is very small, $m \sim 10^{-22}$eV, the large deBroglie wavelength becomes significant in regards to the formation of DM structure. In the following sections we describe such wave effects.

1.4.3 Soliton Condensation

The large scale wave nature of SFψDM gives rise to many interesting phenomena. Cosmological simulations of SFψDM display the formation of a large condensed DM structure referred to as a superfluid or Bose-Einstein Condensate (75; 29; 85). This structure evolves under the influence of gravity but also experiences an outwards scalar pressure which increases with density. Large fluctuations in the DM density can trigger gravitational collapse and lead to a condensation-like process within the Bose-Einstein Condensate. As the field collapses, its increasing outwards pressure eventually reaches an equilibrium with the inwards force of gravity, resulting in a stable droplet-like structure referred to as a SFψDM soliton (described in mathematical depth in chapter 2).

On scales much greater than the scalar field wavelength, these solitons evolve due to gravity in a particle like fashion, similar to other DM theories like the WIMP theory. However, on scales which are comparable to the wavelength, solitons begin to interact with each other as a result of their wavelike nature. Therefore, in adopting the theory of SFψDM, one can retain many of the large scale features of ΛCDM while also gaining a complicated set of wave dynamics that must be resolved at the galactic scale.

Soliton condensation can occur even starting from an almost homogeneous initial condition (50). This has been demonstrated in both the context of an expanding cosmology as well as in the context of virialized clusters of SFψDM. Whether or not this type of condensation occurs depends on the relative sizes of the cluster

and deBroglie wavelength, as well as the timescale of the DM fluctuations. It is an interesting question to ask whether or not soliton condensation can occur within galactic halos which have already formed a central soliton core. If the DM deBroglie wavelength is sufficiently small in comparison to the overall extent of the galactic halo, this may be a possibility. For larger galaxies, this begins to be the case once $m \geqslant 10^{-22}$eV, with the deBroglie wavelength decreasing for higher masses. Whether or not this could occur at physically viable values of m is an open question. This is mainly due to the difficulty which arises when computing galactic scale structure for larger values of m; larger values require greater spatial resolution in order to resolve the relevant wavelengths involved at such scales, greatly increasing required computation time. Notably, the presence of DM self interactions can have significant effects on the condensation process. (28) demonstrates the formation of sub-solitons in a larger DM halo by considering such self-interactions. This case suggests that it is at least plausible for smaller solitons to form in galactic halos in the context of SFψDM.

1.4.4 Galactic Dynamics and SFψDM

Our main contributions in chapters 3 and 4 concern the behavior of SFψDM on the scale of galactic halos. Evaluated for typical galactic velocities (around $100km/s$), the physical deBroglie wavelength scale for SFψDM is

$$\lambda_{dB} = \frac{\hbar}{mv} \approx 0.2kpc \left(\frac{m}{10^{-22}eV}\right)^{-1} \left(\frac{v}{100km/s}\right)^{-1}. \tag{1.35}$$

At sufficiently small values of m, the dynamics of SFψDM are dominated by this wavelength scale. As such, SFψDM paints a rich picture of the shape and dynamics of DM halos. Bottom up style simulations of halos show the formation of a finite density soliton core surrounded by a complicated and turbulent wave structure. The outer halo is characterised by a structure of semi-persistent granules sometimes deemed "quasiparticles," resulting from the interference of its many constituent waves. Describing how to model these halos with the Einstein-Klein-Gordon equations will be

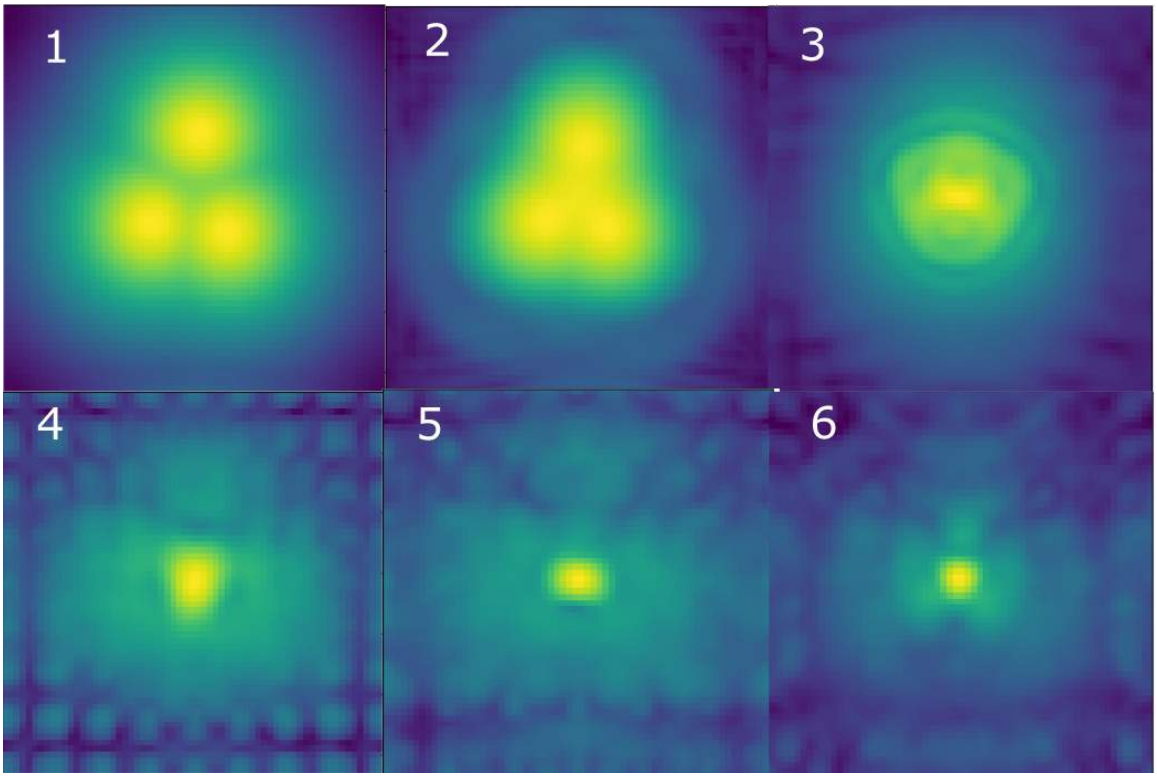

FIGURE 1.6: **Halo Formation:** This demonstrates the merging of 3 equal mass solitons. Density is projected along the line of sight and placed on a logarithmic color scale. As the solitons approach each other, their wave functions begin to overlap and display interference patterns. When the cores finally merge, they release a burst of scalar radiation due to the wave pressure. After a long time, the halo settles to a turbulent and quasistable state with a soliton core at its center. Rectangular features are merely artifacts of the simulation being on a discrete grid.

the primary focus of chapters 3 and 4. We show a basic example of a three-soliton merger in fig. 1.6. Eventually, a quasi-stable system is formed with a soliton at the core.

We depict a quasi-stable SFψDM halo in fig. 1.7. SFψDM halos have many appealing properties in the context of galactic physics. To name a few: the central soliton has a finite density, the outer halo converges to an NFW-like distribution, and their rotation curves are approximately flat. Furthermore, the wave features of the DM can generate some rather unique effects that are potentially observable. For instance, the fluctuations of the halo quasiparticles can generate unique heating effects. Such heating can result in thickening of the galactic disk as well as streams

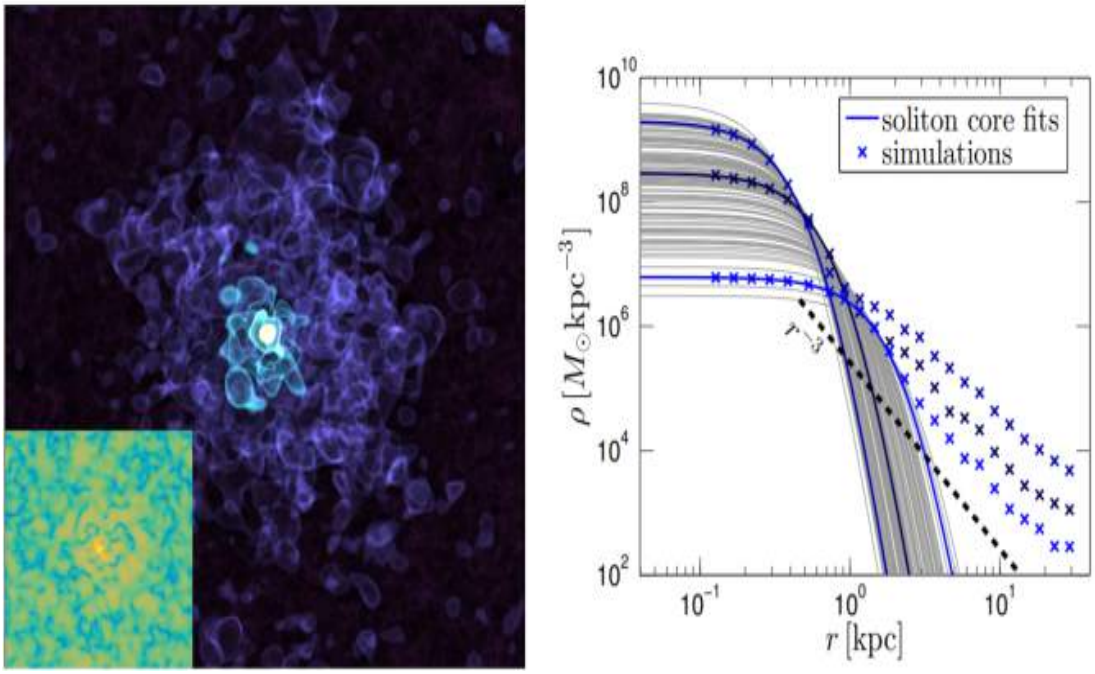

FIGURE 1.7: **Virialized ψDM Halos:** (Left) Visualization of a galactic scale SFψDM halo. (Right) Density profiles for generic halos. Image and graph credited to (62). Halos form stable soliton cores with a finite central density. The core is surrounded by a complicated and turbulent structure resulting from the interference of the halo's many constituent wave modes. In the outer regions, the halo is populated by "quasiparticles," finite density fluctuations which evolve in an N-body fashion.

of stars. The central soliton can exhibit significant density fluctuations. These fluctuations could potentially generate orbital resonances that are observable at the scales of dwarf galaxies.

In chapters 2-4 we explore the properties of galactic SFψDM halos via an analysis of the Einstein-Klein-Gordon equations. In particular, in chapter 3 we discuss the properties of SFψDM rotation curves and their viability for modelling galactic rotation curves. We use this analysis in combination with data from the observed Baryonic Tully-Fisher relation to constrain the possible values of the scalar field mass. In chapter 4, we further the discussions of chapter 3 to include a model for halo oscillations. We detail a possible way to characterize oscillation frequencies of SFψDM halos and then demonstrate the method to produce a halo with a pseudo-stable density oscillation.

1.5 Constraints and SFψDM Phenomenology

This section focuses on SFψDM phenomena and how they can be analyzed to place constraints on the theory. Specifically, we consider constraints on mass parameters in the "Fuzzy Dark Matter Regime" of $m \sim 10^{-22}$eV. This is by no means an exhaustive list of SFψ phenomenology and constraints. Importantly, SFψDM and the investigation of axion-like particles is a growing and active field of modern cosmology. We merely intend to provide an overview and discuss the status of some of the constraints on m.

1.5.1 Heating of the Galactic Disk and Stellar Streams

The outer regions of SFψDM halos are populated with fluctuating quasiparticles. One can naively think of these quasiparticles as semi persistent clumps of DM with a mass scale of

$$M_{fluctuation} = \frac{4\pi}{3}\left(\frac{\lambda_{dB}(r)}{2}\right)^3 \rho_{halo}(r). \tag{1.36}$$

As they pass, these fluctuations can transfer energy into the orbits of stars and generate heating effects. This effect was used to estimate the extent to which quasiparticle fluctuations are able to thicken cold stellar streams (streams of stars stretched out along their orbits, usually due to tidal stripping of star clusters) in (3). By comparing to observations from GAIA regarding six Milky Way stellar streams this returns a constraint of $m \geqslant 1.5 * 10^{-22}$eV. Importantly, since it does not account for heating from subhalos and only considers quasiparticle heating, the model estimates a minimum thickness of the streams to achieve this lower bound. Future observations of thinner stellar streams have the capability of increasing this lower bound. Similar to the thickening of stellar streams, quasiparticle fluctuations can heat and thicken a galaxy's disk. (13) considers the effects of both subhalo heating and quasiparticle heating on galactic disks. By comparing simulated disk thickness to that of the Milky Way one can estimate constraints on m. For sufficiently small values of m, the heating effects are found to be primarily dominated by the quasiparticle fluctu-

ations and can exceed observational bounds. As m becomes large, heating due to subhalos becomes the dominant effect. (13) determines that, in order to not exceed the observed disk thickness, the lower bound on m must be $m \geqslant 0.6 * 10^{-22} eV$.

1.5.2 Black Hole Superradiance

Scalar fields can interact with spinning black holes via a mechanism referred to as *superradiance* (9). Loosely speaking, superradiance occurs when the scalar field reflects at the black hole event horizon and emerges with an increased amplitude via the Penrose process. This can lead to runaway growth of the scalar field which in the process extracts angular momentum from the black hole. Oscillations in the growing scalar field act as a source for gravitational radiation which then disperses the black hole's rotational energy. In summary, the superradiance mechanism allows for the presence of a scalar field to deplete the angular momentum of a spinning black hole. As a result of the superradiance mechanism, only certain combinations of black hole angular momentum and black hole mass are possible in the presence of the massive scalar field. For instance, if the black hole's spin is too high given its mass, the superradiance mechanism is expected to reduce the spin of the black hole by exciting the scalar field.

Through analysis of superradiance, observations of a particular black hole's mass and spin can be used to place constraints on the scalar field's mass parameter, m. By assuming that the superradiance process is insufficient to deplete the observed black hole spin, one can place both upper and lower bounds on m. It was determined in (9) that by observing black holes covering the range of $1M_{\odot} - 10^{10}M_{\odot}$, one could potentially place constraints on the particle mass range of $m = 10^{-21} - 10^{-10}$eV with the heaviest values of m being probed by the smallest black hole masses of order $1M_{\odot}$ and the lightest values of m being probed by the heaviest black holes. The observations of the M87 black hole have been used to provide such constraints in (17). It is found that the M87 observations *exclude* the following mass range:

$$2.9 * 10^{-21} eV < m < 4.6 * 10^{-21} eV. \tag{1.37}$$

Importantly, observational black hole physics is an emerging field. Future developments in black hole observation could provide a means to exclude many regimes of m.

1.5.3 The Subhalo Mass Function

The subhalo mass function (SHMF) describes the expected distribution of subhalos for larger halos like that of the Milky Way. The SHMF of SFψDM was determined by semi-analytical methods in (20). In short, (20) combines a modified Press-Schecter model for halo merger trees with the semi-analytical code Galacticus in order to produce a model for the SHMF. The form of the SFψDM SHMF can be expressed in relation to the SHMF of WIMP-like CDM as

$$\left(\frac{dN}{d\ln M}\right)_{SFDM} = f_1(M) + f_2(M)\left(\frac{dN}{d\ln M}\right)_{WIMP}. \tag{1.38}$$

Determining the form of the functions $f_1(M)$ and $f_2(M)$ was a primary goal of the doctoral thesis (19). These functions are described in (78) and have the effect of suppressing the low mass end of the SHMF. This effect is more prominent for smaller values of m. (78) used this feature to place a lower bound on m by comparing the low mass suppression to that of Warm Dark Matter models. In short, m values which result in greater suppression than WDM models were considered excluded. This results in a conservative lower bound of $m \geqslant 21 * 10^{-22} eV$.

1.5.4 Dwarf Galaxies

There have been a number of efforts to place constraints on SFψDM by comparing theoretical halo profiles to the observed profiles of dwarf galaxies. (73) computes constraints by assuming that SFψDM halos follow a profile modelled by a soliton profile which transitions to an NFW profile at a characteristic distance. This profile gives an inconsistent fit when comparing the profiles of ultrafaint dwarf (UFD) galaxies to those of the Milky Way satellites Sculptor and Fornax. Though Sculptor and Fornax can be fitted by masses of $m > 10^{-22}$eV, the halo mass this would imply for similar

fits to the UFDs is larger than observation by multiple orders of magnitude.

We note that (8) considered modelling dwarf galaxies by using SFψDM excited states to fit dwarf mass profiles as opposed to using soliton cores. Similar values of $m \geqslant 10^{-22}$eV are found for Sculptor and Fornax when assuming a soliton profile. Assuming the profiles are matched by excited states increases the bound. For instance, assuming third and twentieth excited states for Fornax returns bounds of $m \geqslant 4 * 10^{-21}$eV and $m \geqslant 2 * 10^{-20}$eV respectively. Generally, modelling a halo with an excited state allows one to increase the bounds on m. This raises an interesting question in whether or not excited states occur physically. We will discuss the possibility of using excited states as halo models further in the following chapters.

(10) computes a relation between the core density and core radius of SFψDM halos as modelled by a similar soliton-NFW model. They find that the derived relation is inconsistent with the observed relation for dwarf galaxy cores. Lastly, (10) notes that a more detailed description of the transition region between the soliton core and the NFW region might be necessary for resolving this discrepancy.

Data regarding the UFD galaxy Eridanus II has been used to place multiple constraints on the value of m. Eridanus II was first investigated in (58), which combined an analysis of the Milky Way SHMF with a heating model for star clusters in Eridanus II. It was noted that SFψDM could generate core density oscillations in Eridanus II that could result in star cluster heating. Combining this inference with data from Eridanus II's star clusters, (58) claimed a strong bound of $m \geqslant 0.6 * 10^{-19}$eV. This lower bound is significantly higher than most others we discuss, which usually lie in the 10^{-21}eV range. Recently, the stringency of this result has been questioned in (12) which revisits the notion of heating due to density oscillations. The paper concludes via 3D SFψDM simulations that such oscillations produce negligible heating effects in the 10^{-21}eV range. Moreover, it also concludes that the SHMF as used in (58) does not place a strong constraint on m. In final conclusions, (12) suggests that simulations of Milky Way sized SFψDM halos will be important to the understanding of this issue.

1.5.5 Matter Power Spectrum and the Jean Scale

The Matter Power spectrum is an important feature of any particular theory of ΛCDM. In short, the Power Spectrum describes the length scales at which DM structure and substructures form and cluster in the universe. Formally, the Power Spectrum is related to the fluctuation, $\delta(x)$, of the matter density field, $\rho(x)$.

$$\delta(x) = \frac{\rho(x) - \bar{\rho}}{\bar{\rho}} \tag{1.39}$$

The two-point correlation function of the fluctuation, ζ, is then related to the Matter Power Spectrum, $P(k)$, via Fourier transform.

$$\zeta(x - x') = \int \frac{d^3k}{(2\pi)^3} e^{i\vec{k}\cdot(\vec{x}-\vec{x'})} P(k) \tag{1.40}$$

Issues like the Missing Satellites Problem are intimately related to the matter power spectrum. Particle simulations of ΛCDM generally display an excess of small-scale structures in comparison to observation. On the level of the power spectrum, this is manifested as an excess in power at small length scales or high wavenumbers when comparing to observed data. In 2008, Wayne Hu, (41) ,proposed that this small scale power could be suppressed by assuming a FDM version of ΛCDM. The scalar field of SFψDM exhibits an outwards pressure which inhibits the formation of dense small scale structures. As described by Hu, the scale at which SFψDM displays structure formation is described by the Jeans length and wavenumber:

$$L_J = \frac{2\pi}{k_J} = \pi^{\frac{3}{4}} (G\rho)^{-\frac{1}{4}} m^{-\frac{1}{2}}. \tag{1.41}$$

Perturbations smaller than L_J are stable by the Jean analysis and have sufficient pressure support to prevent collapse, while those greater than L_J are unstable, resulting in gravitational collapse of the scalar field. In other words, structure formation and gravitational collapse experience a cutoff at scales corresponding to the Jeans Length, L_J, with structure formation at scales smaller than L_J being suppressed. Using a

simplified 1D model, Hu concluded that masses similar to $m \sim 10^{-22}$eV would result in the suppression of kpc sized cusps and also introduce a cutoff to the low-mass end of the matter power spectrum. Specifically, Hu finds that the cutoff resulting from the Jean scale occurs around $k \sim \left(\frac{m}{10^{-22}eV}\right)^{1/2} Mpc^{-1}$. Hu then suggests that detailed 3D simulations are necessary for fully testing this hypothesis.

1.5.6 Dynamical Friction

Due to its lack of Electromagnetic interaction, DM does not experience friction in the same sense as gases and baryonic matter; a striking demonstration of this feature is the observation of the Bullet Cluster from fig. 1.3. However, via its gravitational interactions, DM can still cause and experience friction-like effects referred to as *dynamical friction*. Dynamical friction plays an important role in many aspects of galactic dynamics, including galaxy mergers, the motion of galactic bars, and the orbital in-fall of satellites.

In the context of SFψDM, dynamics arising from the DM's large wavelength affect the physics of dynamical friction. (42) considers dynamical friction in the context of a point mass moving through a DM fluid as a fundamental example. As the point mass moves through the fluid, its gravity generates an overdensity pattern referred to as a gravitational wake; this wake is associated with a drag-like effect which in turn slows the mass down as it travels through the fluid. For SFψDM, outwards scalar pressure is expected to inhibit the formation of the gravitational wake, thereby reducing the dynamical friction experienced by the passing mass. This reduction was estimated by (42) in the context of the orbital decay of globular clusters in the Fornax dwarf galaxy. Computing the dynamical friction force exerted on an object involves integration of the Energy-Momentum tensor of the DM halo, $\mathbf{\Pi}$, over the surface of the object.

$$F_i = -\int \Pi_{ij} dS_j \tag{1.42}$$

After computing the dynamical friction force exerted by the galaxy's DM halo on the globular clusters, (42) estimates the orbital decay time for each of the Fornax

clusters with a simple formula. Denoting the cluster's angular momentum as L, this is:

$$\tau_{infall} = |\frac{L}{rF}|. \tag{1.43}$$

In the case of a cored SFψDM halo with $m \sim 10^{-22}$eV, the infall time for the Fornax clusters are always increased when compared to the case of particle CDM with a cuspy NFW-like profile. In the case of the shortest infall time, SFψDM results in a time of 2.2Gyr as opposed to 0.37Gyr when assuming particle CDM, raising the possibility of solving the Fornax timing problem with a SFψDM model.

A more detailed treatment of dynamical friction in the context of SFψDM can be found in (47), which uses fully non-linear simulations to resolve the effect. This leads to two primary conclusions. Firstly, particle masses of $m \geqslant 10^{-21}$eV *do not* solve the Fornax timing problem. Secondly, in-falling intermediate massed satellites (around $10^9 M_\odot$) lie outside of valid range for any available analytical theory and warrant further numerical investigations. Ultimately, this regime could be relevant to galactic mergers or in-falling black holes.

1.5.7 Lyman-α Forest

The Lyman-α Forest provides a means to measure the properties of the Matter Power Spectrum along an observational line of sight and can be used to place constraints on DM models. This is possible due to the Lyman-α transition in the neutral hydrogen atom, the transition of the valence electron from the ground state to the first excited state. The transition wavelength, being 121.6nm, can be used to detect clouds of neutral hydrogen. As light from a distant source passes through such a cloud, the 121.6nm wavelengths stimulate the Lyman-α transition, resulting in a "forest" of lines in the absorption signature.

The Lyman-α Forest provides a direct probe to the small scale features of the matter power spectrum. The first constraints on SFψDM resulting from an analysis of the Lyman-α Forest were published in (43), which reports a lower bound of $m \geqslant 2{*}10^{21}$eV. Both (27) and (30) were reported shortly thereafter, and show more or less

similar results. Importantly, this constraint strongly depends on the assumed model for the intergalactic medium (IGM), with (43) noting that assuming a smoother thermal history can increase this bound by at least a factor of 2.

It has been argued that the observable affects SFψDM on the IGM could be mimicked by other IGM physics such as non-trivial gas pressure or large temperature inhomogeneities (42); this highlights the complexity and nuance of using the Lyman-α Forest as a means to constrain SFψDM. The most recent development in regards to the Lyman-α constraint can be found in (70), which improves upon the IGM model used in (43; 27; 30). In short, (70) uses an emulation method as opposed to a brute force method in order to sample the parameter space relevant for producing the matter power spectrum. Combining this method with AxionCAMB and Gadget-MP hydrodynamics resulted in an updated bound of $m \geqslant 2 * 10^{-20}$eV. Importantly, (70) notes that the exact impact of choosing more flexible IGM models on the bound for m is non-trivial. Further, it is suggested that these bounds could be strengthened by probing even smaller scales in the Lyman-α data.

1.5.8 Resolution to Small-Scale Crises?

Whether or not SFψDM solves the many "small-scale crises" of ΛCDM is more or less inconclusive at this point. There are many reasons one may wish to use SFψDM to address these problems - SFψDM's lack of cuspy density profiles for instance. On the other hand, the non-linear wave features of SFψDM require in depth simulations in the relevant regime of $m \sim 10^{-22}$eV.

As the value of m increases, the capability of SFψDM to directly affect the small-scale crisis becomes lessened, but at the same time, the spatial resolution required to simulate the non-linear dynamics of SFψDM also increases. Herein lies one of the most challenging aspects of SFψDM theory; small scale wavelike dynamics must be resolved to make strong conclusions about the 10^{-22}eV regime. This becomes particularly challenging when simulating the effects of small-scale SFψDM physics on larger scale structures like that of galaxies and galaxy clusters.

There are several senses by which SFψDM does not solve the small scale crisis.

Constraints from the Lyman-α forest (43; 27; 30; 70) seem to be most at tension with the overall notion, preferring higher values of m ($m \sim 10^{-20}$eV) than those originally proposed as candidates for solving these small scale issues ($m \sim 10^{-22}$eV). However, uncertainties and modelling difficulties arising from the IGM cause some to question the Lyman-α constraints. Independently, results from quasar lensing and the SHMF (78) seem to be more or less consistent with the Lyman-α constraints, bringing the possibility of resolving small scale issues with SFψDM into question. On the other hand, simulations of Milky-Way sized SFψDM halos are required to provide a full picture of what SFψDM implies for the SHMF.

As a final note, we re-emphasize that simulating the effects of SFψDM on structure formation is very computationally intense if one wishes to resolve all relevant length scales. In order to understand the effects of SFψDM on structure formation, one must resolve the scales of galaxies and galaxy clusters as well as the deBroglie scale of the SFψDM particles which can often be orders of magnitude smaller. At this point, such a level of resolution has not been achieved by any 3D simulation of SFψDM. Ultimately, higher resolution simulations of SFψDM may be necessary to understand the full impacts of SFψDM on small-scale structure. Alternatively, this opens the door for developing new and creative ways to model SFψDM physics which might reduce the computational power required for such models.

2

General Relativity and the Einstein Klein Gordon Equations

2.1 The Hilbert Action

The Einstein Field Equations as posed in eq. 1.23 are the fundamental equations of GR. Attributed to Hilbert in 1915, the EFEs are attainable via an action principle formulation. That is, the EFEs are known to be the critical points of the Einstein-Hilbert Action

$$S_H = \int dV(R - 2\Lambda + 16\pi L_M) = \int d^4x\sqrt{-\det(\mathbf{g})}(R - 2\Lambda + 16\pi L_M). \tag{2.1}$$

Here, R refers to the scalar curvature [1] (eq. 1.22) and L_M denotes a matter Lagrangian. Computing the critical point of the action, and thereby the EFEs, amounts to solving the condition of $\delta S_H = 0$. Then, a common scheme for this computation is to consider variations with respect to the metric coefficients, $g_{\mu\nu}$. The variation of terms involving L_M leads to a natural definition for the components of the SE

[1] In this chapter, R is assumed to be the Levi-Civita form of the scalar curvature.

tensor:

$$T_{\mu\nu} = \frac{-2}{\sqrt{-\det(\mathbf{g})}} \frac{\delta(L_M \sqrt{-\det(\mathbf{g})})}{\delta g^{\mu\nu}}. \tag{2.2}$$

The variation of the terms involving the scalar curvature reproduces the common formula for the Einstein Curvature Tensor

$$\frac{1}{\sqrt{-\det(\mathbf{g})}} \frac{\delta(R\sqrt{-\det(\mathbf{g})})}{\delta g^{\mu\nu}} = R_{\mu\nu} - \frac{1}{2} g_{\mu\nu} R = G_{\mu\nu}. \tag{2.3}$$

Lastly, we list the variation of the cosmological constant term

$$\frac{1}{\sqrt{-\det(\mathbf{g})}} \frac{\delta\sqrt{-\det(\mathbf{g}))}\Lambda}{\delta g^{\mu\nu}} = \frac{1}{2}\Lambda g_{\mu\nu}. \tag{2.4}$$

Combining these variations results in the coordinate version of eq. 1.23.

$$\delta S_H = \frac{\delta S_H}{\delta g^{\mu\nu}} \delta g^{\mu\nu} = 0 \tag{2.5}$$

$$G_{\mu\nu} + \Lambda g_{\mu\nu} = 8\pi T_{\mu\nu} \tag{2.6}$$

2.2 The Einstein-Klein-Gordon Action

In GR, one can include the dynamics of matter fields at the action level by choosing a form for the matter Lagrangian, L_M. For this thesis, we are particularly interested in including the dynamics of a massive scalar field ϕ, with a mass parameter m. Taking inspiration from classical field theory, this is achieved by assuming the following Lagrangian for the scalar

$$L_\phi = -\frac{1}{2}|\partial_\mu \phi|^2 - \frac{1}{2} m^2 |\phi|^2. \tag{2.7}$$

We note that this equation is valid for both real and complex scalar fields. The corresponding SE tensor can be computed as defined in eq. 2.2. We express this

quantity in coordinate free form as

$$\mathbf{T}_\phi = \frac{\mathbf{d}\phi \otimes \mathbf{d}\bar{\phi} + \mathbf{d}\bar{\phi} \otimes \mathbf{d}\phi}{2m^2} - \left(\frac{|\mathbf{d}\phi|^2}{2m^2} + \frac{|\phi|^2}{2} \right) \mathbf{g}. \tag{2.8}$$

Performing the variation with respect to the metric as in section 2.1 then results in the EFEs with the above SE tensor. In addition, since ϕ is included at the action level, one must consider the variations with respect to ϕ itself; this variation is well known to produce the Klein-Gordon (KG) equation. We therefore reach the coupled Einstein-Klein-Gordon (EKG) equations.

$$\mathbf{G} + \Lambda \mathbf{g} = 8\pi \mathbf{T}_\phi \tag{2.9}$$

$$\Box\phi = m^2\phi \tag{2.10}$$

This set of equations describes a massive scalar field evolving under the influence of its own self-gravity. Importantly, the coupling of the scalar to the metric can be seen in the d'Alembert operator $\Box\phi = \frac{1}{\sqrt{-\det(\mathbf{g})}} \partial_\lambda (\sqrt{-\det(\mathbf{g})} g^{\lambda\mu} \partial_\mu \phi)$.

2.3 Geometry and SFψDM

2.3.1 Weyl's Uniqueness Theorem

The Einstein-Hilbert action of eq. 2.1 can be "derived" by making a few geometric assumptions. To demonstrate these, let us first consider the part of the action integral containing the scalar curvature. We can expand this term in coordinate expression as

$$R = (g^{ik}g^{jl} - g^{ij}g^{kl})g_{ij,kl} + \tag{2.11}$$

$$g_{ij,k}g_{ab,c}\left(\frac{3}{4}g^{ia}g^{jb}g^{kc} - \frac{1}{2}g^{ia}g^{jc}g^{kb} - g^{ia}g^{jk}g^{bc} - \frac{1}{4}g^{ij}g^{ab}g^{kc} + g^{ij}g^{ac}g^{kb} \right)$$

Upon inspection, we can make several notes about this expression: (1) It contains derivatives of the metric up to second order; (2) It is linear in the second derivatives

of the metric; (3) It is a geometric invariant. It is an interesting fact that, up to an additive constant, R is the unique invariant that satisfies these properties. This was originally proven by Weyl in (94), though is sometimes referred to as Lovelock's theorem due to Lovelock's further study of the theorem in (53). Most formally stated, up to an additive constant, the most unique action which satisfies properties (1)-(3) is, for a constant, c,

$$S_H = c \int dV(R - 2\Lambda). \tag{2.12}$$

2.3.2 Actions with Non-Trivial Connections

One could think of the criteria for Weyl's uniqueness theorem as a set of axioms for formulating the action of GR. It is an interesting venture to try to modify these criteria. For instance, we could suppose that the action contains other types of geometric couplings. (7) proved that if one allows the action to contain not only derivatives of the metric, but also derivatives of the connection, that one can reproduce the EFEs with a coupling to the KG equation. Following their procedure, we can state this formally by modifying the assumptions (1)-(3) of Weyl's theorem. Suppose that we instead assume that the action functional: (1*) Contains the metric and its derivatives up to second order. (2*) Is of linear order in the second derivatives of the metric. (3*) Contains the connection coefficients and their first derivatives. (4*) Is quadratic in the connection and its derivatives. (5*) Is a geometric invariant. These axioms allow the inclusion of terms involving the Difference and Torsion tensors from eqs. 1.14 and 1.17. Actions obeying (1*)-(5*) can then be written rather concisely as

$$S = \int dV(R - 2\Lambda - \frac{c}{24}|\mathbf{d}\gamma|^2 + Quad(\mathbf{D})). \tag{2.13}$$

The expression $\mathbf{d}\gamma$ is the exterior derivative of the three form defined by the fully antisymmetric part of the difference tensor. As well, this is the only object involving derivatives of the Torsion tensor which obey (4*). Explicitly, γ can be written in

coordinate form in terms of the Torsion tensor as

$$\gamma_{ijk} = \frac{1}{6}(T_{ijk} + T_{jki} + T_{kij}). \tag{2.14}$$

The expression $Quad(\mathbf{D})$ is a function which is at most quadratic with respect to the difference tensor. This expression can be build out of the irreducible components of the difference tensor. Still following the discussion of (7), we will consider a simplified case where these irreducible components are all zero, other than the fully antisymmetric component, γ. Importantly, connections with a fully antisymmetric difference tensor have the same geodesics as the Levi-Civita connection. Thus, the connection which results from this simplification will have geodesics which are equivalent to those of standard GR. We thereby reach the following action:

$$S = \int dV(R - 2\Lambda - \frac{c}{24}|\mathbf{d}\gamma|^2 + \frac{c_2}{6}|\gamma|^2). \tag{2.15}$$

2.3.3 Deriving the Einstein Klein Gordon Equations

At this point, we need just evaluate the equations of motion. The three-form γ can be rewritten in terms of a vector field, $\mathbf{v}$ which is related to the Hodge dual of γ. Explicitly, denoting the Hodge star as *, we have $\gamma = *(\tilde{\mathbf{v}})$ where we have denoted the one-form dual of $\mathbf{v}$ as $\tilde{\mathbf{v}}$. This brings the action to the form of

$$S = \int dV(R - 2\Lambda - c(\nabla \cdot \mathbf{v})^2 + c_2|\mathbf{v}|^2). \tag{2.16}$$

We now compute the variations of the action similarly to section 2.1, but also including the variations of the newly introduced vector field. Following the exact computation in (7), the resulting equations of motion are

$$\mathbf{G} + \Lambda\mathbf{g} = c\tilde{\mathbf{v}} \otimes \tilde{\mathbf{v}} - \frac{1}{2}(c_2(\nabla \cdot \mathbf{v})^2 + c_2|\mathbf{v}|^2)\mathbf{g} \tag{2.17}$$

$$\nabla(\nabla \cdot \mathbf{v}) = \frac{c}{c_2}\mathbf{v}. \tag{2.18}$$

This system is equivalent to the EKGEs from eqs. 2.9 and 2.10 with a particular choice of parameterization. That is, if we make one last redefinition and take $\phi = (\frac{c}{c_2})^{\frac{1}{2}} \nabla \cdot \mathbf{v}$ (equivalent to taking $\mathbf{v} \propto \nabla\phi$) we finally reach the expected form

$$\mathbf{G} + \Lambda \mathbf{g} = c \left(\mathbf{d}\phi \otimes \mathbf{d}\phi - \frac{1}{2} \left(|\mathbf{d}\phi|^2 + \frac{c_2}{c}\phi^2 \right) \mathbf{g} \right) \tag{2.19}$$

$$\Box\phi = \frac{c_2}{c}\phi. \tag{2.20}$$

Finally, we need just identify the relevant constants as $m = \frac{c_2}{c}$ and $c = 16\pi$ to reproduce the EKGEs.

2.3.4 Some Comments Regarding Connections

The fact that the EKGEs can be reproduced from purely geometric arguments as in the previous section is extremely interesting in the context of the theory of GR. In short, this computation demonstrates that having a connection which is not Levi-Civita can have physical consequences. In the case of section 2.3.3, that consequence is interpreted as a dark matter density. Importantly, the form of eq. 2.16 was reached by restricting to a small subset of connections for which the difference tensor was antisymmetric, thereby producing the same geodesics as the standard Levi-Civita connection. Effectively, this means that the theory derived was physically equivalent to usual GR in the presence of a scalar field SE tensor.

We emphasize, one could consider a more generic set of connections and arrive at a different, more complicated result. That is, if one considers the other components of the difference tensor, the theory will be distinct from GR in that it contains a connection with geodesics different from those of the Levi-Civita connection. What this implies and what such theories represent in a physical context is an open question. In principal, one could modify the procedure of section 2.3.2 to include actions which allow for such connections. Going further, interpreting the SFψDM theory as being inspired by a non-trivial connection is an interesting alternative to the usual particle physics inspired approach, and has the potential to make physically distinct

predictions.

2.4 Spherically Symmetric Static Solutions

Complex valued scalar fields admit static solutions to the EKG equations which are well characterized in the case of spherical symmetry (45; 72). These spherically symmetric static (SSS) solutions can be described with the following ansatz for the metric line element and the scalar field (35):

$$ds^2 = -e^{2V(r)}dt^2 + \Phi(r)^{-1}dr^2 + r^2 d\theta^2 + r^2 \sin^2(\theta) d\phi^2 \tag{2.21}$$

$$\phi(r,t) = \Psi(r)e^{-i\omega t}. \tag{2.22}$$

Here, we have written the scalar field ϕ in terms of its radial component, Ψ, multiplied by an angular argument. In this ansatz, the function $V(r)$ is interpreted as the gravitational potential and $\Phi(r) = (1 - 2\frac{M(r)}{r})$ contains the mass enclosed by a radius, $M(r)$. The variable ω is referred to as the static state's *frequency*, which we will see later is related to the total mass of the state. Inserting this above ansatz into the EKG equations of eqs. 2.9 and 2.10 results in the following system of ordinary differential equations (ODEs):

$$M_r = \frac{4\pi r^2}{2m^2}\left[(m^2 + \omega^2 e^{-2V})\Psi^2 + \Phi\Psi_r^2\right] \tag{2.23}$$

$$\Phi V_r = \frac{M}{r^2} - \frac{4\pi r}{2m^2}\left[(m^2 - \omega^2 e^{-2V})\Psi^2 - \Phi\Psi_r^2\right] \tag{2.24}$$

$$\Psi_{rr} + \frac{2}{r}\Psi_r + V_r\Psi_r + \frac{\Phi_r}{2\Phi}\Psi_r = \Phi^{-1}(m^2 - \omega^2 e^{-2V})\Psi. \tag{2.25}$$

Bounded and physically realizable solutions require that $M(0) = 0$, $\Psi_r(0) = 0$, $\lim_{r\to\infty} M(r)$ and $\lim_{r\to\infty} V(r)$ to be finite, and $\lim_{r\to\infty} \Psi(r) = 0$. The central conditions ensure regularity at the origin, while the limits ensure a finite mass, compact solution. We will take the usual convention that $V(r)$ is negative and $\lim_{r\to\infty} V(r) = 0$,

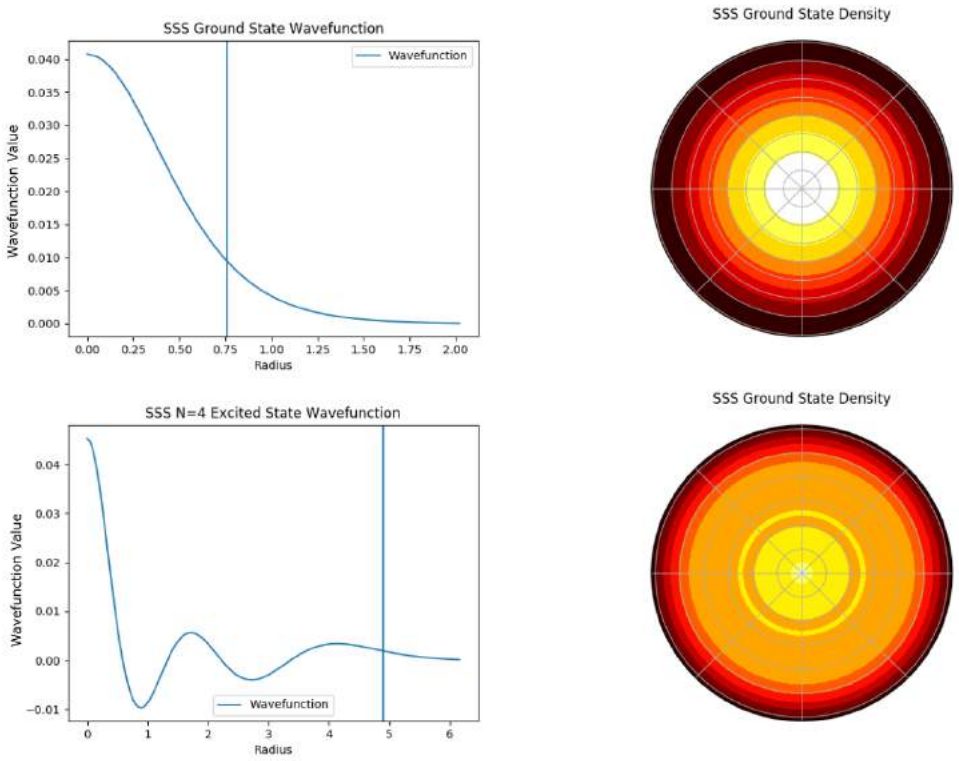

FIGURE 2.1: **SSS States:** Visualization of SSS State wavefunctions and corresponding density profiles. Top row depicts the ground state, bottom row depicts the 4th excited state. Density profiles (right) are projected along the line of sight and placed on a logarithmic color scale for visualization. The excited state is characterised by the nodes of the wavefunction (left).

so that the potential $V(r)$ converges to the usual form of the Newtonian potential. We note that this is not strictly required to compute bounded and compact solutions, but can easily be achieved once such a solution is found. The equations are preserved under the transformation of $\{V, \omega\} \rightarrow \{V + \tilde{V}, \omega e^{\tilde{V}}\}$. At the level of the metric line element, this is equivalent to rescaling the time coordinate by a factor of $e^{2\tilde{V}}$; adding a constant to the potential $V(r)$ amounts to a change of coordinates.

The behavior of the SSS wavefunctions, $\Psi(r)$, can be understood by considering the right hand side of eq. 2.25. The term $k^2(r) = (m^2 - \omega^2 e^{-2V})$ determines whether or not Ψ displays oscillatory or exponential behavior. Since the potential $V(r)$ is negative, solutions with $\omega > m$ are always oscillatory, having an always negative

$k^2(r)$; such solutions constitute an infinite mass, and are nonphysical. Likewise, only solutions with $\omega < m$ can display exponential behaviors, allowing exponential decay to zero value. These solutions, given sufficiently negative $V(r)$, can have an initially negative value of $k^2(r)$ and thus an oscillatory central region. Eventually, the solution reaches a decay radius, R_d, at which $k(R_d) = 0$ and the oscillatory behavior converts into an exponential decay. Each wavefunction, $\Psi(r)$, will therefore have a finite number of nodes before eventually exhibiting an exponential decay. Counting the number of nodes as n, the $n = 0$ solution is referred to as the *ground state* solution, while the $n > 0$ states are referred to as *excited states*. Generically, we will refer to a state of order n as an "nth-excited state."

As described, bounded static solutions form a three-parameter family specified by 2 continuous parameters and 1 discrete parameter. A particularly intuitive parameterisation is fix the total mass and excitation number, n, of the solution by choosing $\{m, M_{tot}, n\}$. In other words, for a fixed value of the particle mass, m ,and a fixed value of total dark matter mass, M_{tot}, there exists a countable number of solutions which are nth-excited states. There exists other ways to parameterize the states, $\{m, \Psi(0), \omega\}$ for instance; fixing m and the central density amplitude $\Psi(0)$, there is a discrete set of ω which determine the nth-excited states.

Finding a family of nth-excited states is a computationally intensive process, but can be achieved through basic numerical integration techniques. In the case of eqs. 2.23 - 2.25, finding an nth-excited state requires one solve a shooting problem for the initial conditions $\Psi(0)$ and $V(0)$, as well as the frequency ω. We detail this procedure in the Appendix for those who wish to compute the SSS excited states.

2.5 The Poisson Schrödinger Equations

The Poisson-Schrödinger Equations (PSEs), or sometimes dubbed the Schrödinger-Newton Equations, are the non-relativistic and low-field analogs of the EKGEs. The PSEs can be thought of as a modification of the usual Schrödinger equation in which the relevant potential energy is taken to be the gravitational potential energy of

the Schrödinger wave's density as computed by the Poisson equation. This rather intuitive construction can be immediately written down for a complex scalar field ψ as

$$i\frac{\partial\psi}{\partial t} = -\frac{1}{2m}\nabla^2\psi + mV\psi \tag{2.26}$$

$$\nabla^2 V = 4\pi|\psi|^2. \tag{2.27}$$

Here, we identify the gravitational potential energy mV as being sourced from the wave's corresponding density $|\psi|^2$. This system of equations was studied long before the theory of Wave Dark Matter was founded in the context of boson stars (45; 72). Boson stars are hypothetical objects formed by bosonic particles bound by their own self gravity, usually motivated by studies of axion-like particles.

It is important to understand how the PSEs can be derived as the low-field and non-relativistic limit of the EKGEs. We will describe two simple constructions which are equivalent in this limit, one in which the scalar field is taken to be complex at the level of the EKGEs and one in which the scalar field is taken to be strictly real. Both of these cases can be *effectively described* by the PSEs for a *complex* scalar field as in eqs. 2.26 and 2.27.

2.5.1 PSEs from a Real Klein-Gordon Field

The case of assuming a real scalar field at the level of the EKGEs comes with the possibility of interpreting the scalar as an axion-like particle. We start from eqs. 2.9 and 2.10, taking ϕ to be a real scalar field and taking $\Lambda << 1$. The $\Lambda << 1$ approximation simply allows us to restrict to small scales at which the expansion of spacetime is negligible, similar to galactic length scales. To apply the low-field non-relativistic limit, we take the gravitational potential to be small, $V << 1$. This can be achieved by assuming the following weak-field metric line element (detailed in (40)).

$$ds^2 = -(1+2V)dt^2 + (1-2V)(dx^2+dy^2+dz^2) \tag{2.28}$$

To obtain the PSEs we must also ensure that the boson is non-relativistic (i.e.

low energy). This is usually done by parameterizing the real field, ϕ, as the real part of a complex field, ψ, and then assuming that the energy of ψ is small. That is, we write ϕ as

$$\phi = \frac{1}{\sqrt{2}}(\psi e^{imt} + \psi^* e^{-imt}). \tag{2.29}$$

The small energy condition can then be expressed as

$$E_\psi = i\frac{\partial \psi}{\partial t} << 1. \tag{2.30}$$

This energy condition is equivalent to assuming that the energy of the real field, ϕ, is close to its rest mass energy. In other words, this condition ensures the velocity of the wave to be small. By taking the assumptions expressed in eqs. 2.28 thru 2.30 at the level of the EKGEs in eqs. 2.9 thru 2.10 and lastly, retaining only leading order terms of the potential, V, and its derivatives, one arrives at the PSEs of eqs. 2.26 and 2.27.

2.5.2 PSEs from a Complex Klein-Gordon Field

Assuming a complex scalar field at the level of the EKGEs is highly convenient in the sense that it simplifies many computations. Moreover, complex scalar fields admit solutions to the EKGEs which are long-time stable, something which real scalars can only achieve in the low-field limit. Of course, irrespective of these benefits, the low-field and non-relativistic limit is equivalent to the real case and is expressed by the PSEs. This limit is taken similarly to the real case in that we can assume the weak-field metric from eq. 2.28. The small energy condition can still be applied, but must be slightly modified to account for the fact that Φ is already taken to be complex. This results in expressing Φ in terms of a low energy complex scalar, ψ.

$$\phi = \psi e^{-imt} \tag{2.31}$$

$$E_\psi = i\frac{\partial \psi}{\partial t} << 1 \tag{2.32}$$

Combining these assumptions with the EKGEs of eqs. 2.9 and 2.10, again results in the PSEs from eqs. 2.26 and 2.27, this time expressed in terms of a complex scalar field ψ.

2.5.3 PSEs in Fluid Form: Madelung Transformation

The PSEs describe the density amplitude of the Schrödinger wave as ψ. By applying the well known Madelung Transformation, one can convert eqs. 2.26 and 2.27 to a form describing the density and velocity of a fluid (84). This transformation appears as

$$\psi = \sqrt{\rho} e^{iS} \tag{2.33}$$

$$\vec{v} = \frac{1}{m} \nabla S. \tag{2.34}$$

Here, we interpret $\rho = |\psi|^2$ as the density of the fluid and $\vec{v}$ as the corresponding fluid velocity. Inserting these parameterizations into eqs. 2.26 and 2.27 results in the fluid form of the PSES:

$$\frac{\partial \rho}{\partial t} + \nabla \cdot (\rho \vec{v}) = 0 \tag{2.35}$$

$$\frac{\partial \vec{v}}{\partial t} + (\vec{v} \cdot \nabla)\vec{v} = \frac{1}{m} \nabla (Q + V). \tag{2.36}$$

Here, we have expressed the "quantum potential" as Q, which represents the following formula:

$$Q = -\frac{1}{2m} \frac{\nabla^2 \sqrt{\rho}}{\sqrt{\rho}}. \tag{2.37}$$

Further, the pressure of the scalar field can be written as a tensoral object:

$$\mathbf{P} = \frac{1}{4m^2} \rho \nabla \otimes \nabla (\ln(\rho)). \tag{2.38}$$

Lastly, we can express the energies and angular momenta of the wave. The kinetic energy, potential energy, and angular momentum densities are respectively

$$k = \frac{1}{2m}|\nabla\psi|^2 \tag{2.39}$$

$$u = \frac{1}{2}mV|\psi|^2 \tag{2.40}$$

$$\vec{l} = \vec{r} \times (\rho\vec{v}). \tag{2.41}$$

The total mass, $M = \int(d^3x\rho)$, total energy, $E = \int(d^3x(k+u))$, and total angular momentum $\vec{L} = \int(d^3x\vec{l})$ are conserved quantities of the PS system and thus constant in time.

2.5.4 Scaling Relations of the PS Equations

A well known and useful property of the PSEs is that they admit a set of exact scaling relations (81). That is, once a solution to the system is found, another solution can be generated by appropriately re-scaling the values of the original. There are two scalings of interest: spatial dilation of the form $x \to \alpha x$, and scalings of the boson mass of the form $m \to \beta m$. Under a spatial dilation, we can express the scaling as follows for a positive scaling constant α:

$$\{m, x, t, V, \psi\} \to \{m, \alpha x, \alpha^2 t, \alpha^{-2}V, \alpha^{-2}\psi\}. \tag{2.42}$$

Likewise, for scalings of the boson mass we take β to be positive, stating the relation as:

$$\{m, x, t, V, \psi\} \to \{\beta m, x, \beta t, \beta^{-2}V, \beta^{-1}\psi\}. \tag{2.43}$$

These two sets of scaling relations can of course be combined into a single line to display the full scaling properties of the PSEs. For completeness this gives

$$\{m, x, t, V, \psi\} \to \{\beta m, \alpha x, \alpha^2\beta t, \alpha^{-2}\beta^{-2}V, \alpha^{-2}\beta^{-1}\psi\}. \tag{2.44}$$

One could choose to express this relation for different types of re-scalings. For instance, instead of considering spatial dilation like $x \rightarrow \alpha x$ one could consider a scaling of the wavefunction amplitude as $\psi \rightarrow \gamma\psi$. In this case we need only identify the relationship between these scalings by taking $\alpha^{-2} = \gamma$.

All relevant physical quantities can be rescaled by an appropriate application of eq. 2.44. For instance, to rescale the density, ρ, we make use of the relationship of $\rho = |\psi|^2$, resulting in a scaling of $\rho \rightarrow \alpha^{-4}\beta^{-2}\rho$. Likewise, the DM mass values, energies, angular momentum scales transform respectively as

$$\{M, E, L\} \rightarrow \{\alpha^{-1}\beta^{-2}M, \alpha^{-3}\beta^{-4}E, \alpha^{-1}\beta^{-3}L\}. \tag{2.45}$$

An interesting and useful result of the scaling relationships just described is that each solution is associated with many scale-invariant quantities. The most illustrative example is the following product of half of the solution total mass, M_h, and the radius containing half that mass, R_h:

$$I = m^2 M_h R_h. \tag{2.46}$$

One can see that no matter what values of α and β are chosen from eq. 2.44, the value of I is unchanged. Another way to read eq. 2.46 is that for any given solution the value of $M_{tot}R_h$ lies on a hyperbola defined by the boson mass, $M_h R_h = \frac{I}{m^2}$ (see fig. 2.2). Finally, this means that for any particular value of m, the product $M_h R_h$ is constant. Larger values of M_h necessarily correspond to smaller values of R_h and vice-versa. For the case of a ground state soliton, the mass-radius relation can be evaluated as in (42) to yield the following relation

$$R_h = .335kpc \left(\frac{10^9 M_\odot}{M_{tot}}\right) \left(\frac{10^{-22}ev}{m}\right)^2. \tag{2.47}$$

Any particular product of DM mass and radius corresponding to the PSEs will form a similar invariant as in eq. 2.47. For instance, one can replace M_h with the total mass, M_{tot}, instead and compute a similar relation. Going further, one can

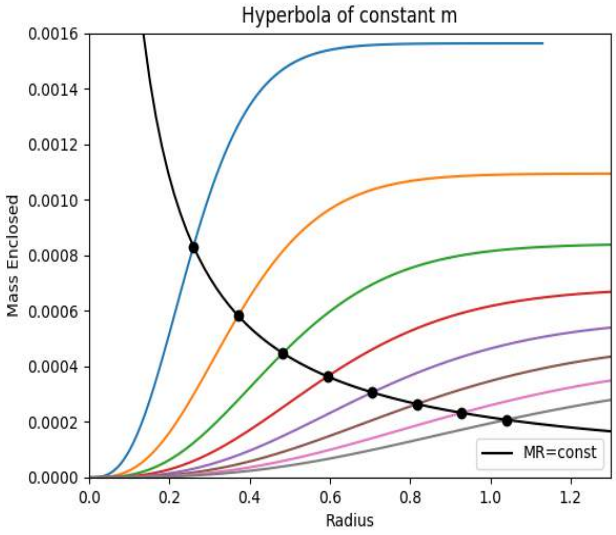

FIGURE 2.2: **Hyperbolas of Constant m:** Plot rendered with computational units of $m = 100$. Various re-scalings of the ground state mass profile are shown. The half-mass radius is denoted on each curve by a black point. A hyperbola is superimposed, demonstrating that $M_h R_h = constant$ for a fixed value of m.

construct characteristic functions which are invariant under rescaling. To illustrate, we define the following function

$$C(r) = m^2 M(r) r. \tag{2.48}$$

Here, we denote the DM mass contained within a radius r as $M(r)$. We can see that under a scaling as in eq. 2.44, that $C(r)$ transforms as $C(r) \rightarrow C(\alpha r)$. Hence, if we re-parameterize the function in terms of some characteristic radius, $x = \frac{r}{R_h}$ for instance, we will have a function, $C(x)$, which is unchanged by the scaling of eq. 2.44.

$$C(x) = m^2 M(x) R_h x \tag{2.49}$$

For an illustrative example of the scaling relations, we refer the reader to fig. 2.4.

2.5.5 Poisson-Schrödinger Equations in SSS Case

It will be instructive as well as useful to describe the SSS states in the non-relativistic and low-field limit. We will describe two ways of attaining the SSS equations for

this limit. Firstly, we will directly apply the limit to the SSS EKG system in eqs. 2.23-2.25. Secondly we will attain the same set of equations by applying a similar harmonic ansatz to eq. 2.22 to the already low-field and non-relativistic form of the PSEs in eq. 2.26 and 2.27.

First, we consider the SSS EKGEs in eqs. 2.23-2.25. To apply the low-field and non-relativistic limit, we apply two sets of approximations. To ensure the low-field criteria we take the approximations that $V << 1$, $\Phi \approx 1$, $V_r << 1$, and $\Phi_r << 1$. These are equivalent to assuming the metric to be close to the Minkowski metric. The non-relativistic limit corresponds to taking the approximations of $\frac{\omega}{m} \approx 1$ and $\Psi_r << 1$. This is equivalent to taking the group velocity of the DM to be small in comparison to the speed of light. Applying these approximations then results in the SSS version of the PSEs

$$M_r = 4\pi r^2 |\Psi|^2 \tag{2.50}$$

$$V_r = \frac{M}{r^2} \tag{2.51}$$

$$\Psi_{rr} + \frac{2}{r}\Psi_r = 2m(m - \omega + mV)\Psi. \tag{2.52}$$

Eqs. 2.50 and 2.51 are the analog to the Poisson Equation. This can be seen by computing the Laplacian of $V(r)$ in spherical coordinates and inserting the eqs. 2.50 and 2.51.

$$\nabla^2 V = V_{rr} + \frac{2}{r}V_r = \frac{M_r}{r^2} - 2\frac{M}{r^3} + \frac{2}{r}4\pi r^2|\Psi|^2 = 4\pi r^2\Psi^2 = 4\pi r^2|\psi|^2 \tag{2.53}$$

Taking the low-field and non-relativistic limit therefore recovers the effective DM density again as $|\Psi|^2$.

Equation 2.52 plays the role of the Schrödinger equation of eq. 2.26. This equation can be computed directly by assuming the harmonic ansatz of $\psi = \Psi e^{i(m-\omega)t}$ and applying it to eq. 2.26. We note that this is effectively the same as taking the slightly different harmonic ansatz of eq. 2.22 at the level of the EKGEs and then

applying the low-field and non-relativistic limit as described in section 2.5.2. The additional factor of e^{imt} cancels with the factor of e^{-imt} from the approximation in eq. 2.31, ensuring that the Klein-Gordon field matches the appropriate ansatz from eq. 2.22. Further, we can identify the quantity of $(m - \omega)$ as an energy eigenvalue for the static state. The low energy condition can be thought of as equivalent to the low group velocity condition stated earlier, $\frac{\omega}{m} \approx 1$.

Solutions to the SSS PSEs are analogous to the ones described for the SSS EKGEs described in section 2.4. Namely, they can be specified by their total mass and number of wavefunction nodes, forming a family of excited states. We identify the relevant wavenumber in this case as $k^2(r) = -2m(m - \omega + mV(r))$.

2.6 Properties of Solitons and Excited States

The SSS states have been studied in many contexts. The first instance of considering the EKG system can be traced to (45) in which they were used to model systems of self gravitating scalar particles commonly referred to as "Boson Stars." Importantly, complex scalars admit boson star solutions with the harmonic form of eq. 2.22. These solutions form quasibound states, with only the ground state being long time stable upon perturbations. The ground state boson star, otherwise known as the SFψDM soliton has a critical mass value, M_c, above which the state will either collapse into a black hole or reduce its mass by emission of scalar radiation. This mass value was first computed by (44), and can be expressed in standard units as

$$M_c \approx \frac{0.633\hbar c^3}{Gm} \approx 8.5 * 10^{11} M_\odot \left(\frac{10^{-22} eV}{m}\right). \tag{2.54}$$

For comparison, in the $10^{-22} eV$ regime, this mass value is comparable to that expected for large supermassive black holes (with M87 having a mass of $\sim 10^9 M_\odot$). Soliton masses that are small in comparison to M_c can be considered in the low-field regime, and are well approximated by the Poisson Schrödinger system. The soliton itself will have a density distribution which is well approximated by the "core-halo"

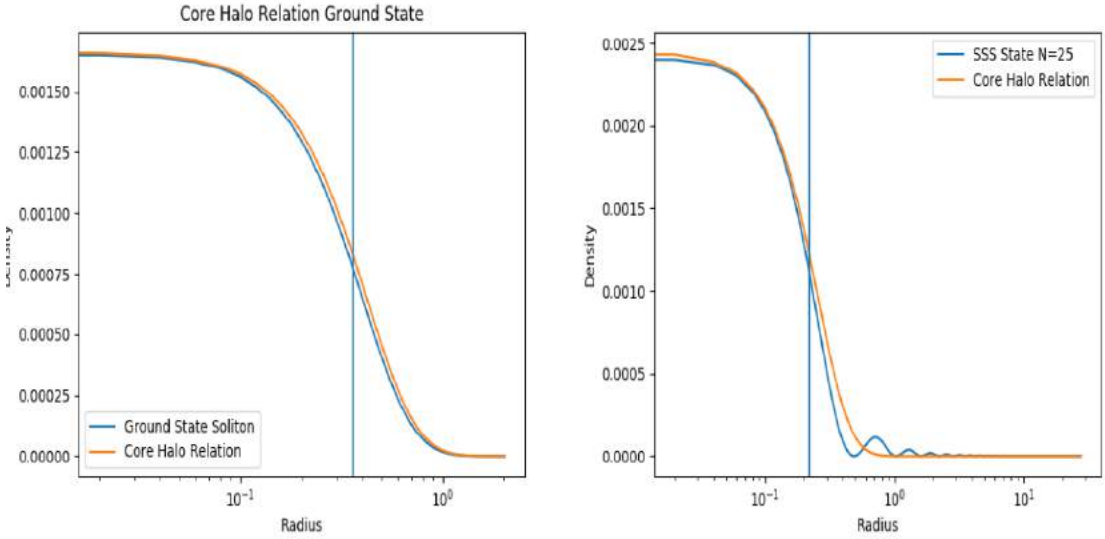

FIGURE 2.3: **Core Halo Relation:** The Core Halo relation plotted for the ground state (left) as well as a 25th excited state (right). Plots rendered using units of $m = 100$ and value of $\omega = 0.999m$. The core-halo relation describes the density behavior well, at least to leading order. Excited states generically have more compacted central cores but greater total spatial extent.

relation from (76) (see fig. 2.3).

$$\rho_c(r) = \rho_0 \left(1 + .091 \left(\frac{r}{r_c}\right)^2\right)^{-8} \tag{2.55}$$

Here, ρ_0 is the central density and r_c is the "core-radius" at which the density has fallen to half of its central value. We note that while this relation is a good fit to the ground state soliton, it also describes the leading order behavior of the excited states fairly well, this can be seen in fig. 2.3. Importantly, the effective radius of any particular state can be determined by its total mass. This is a result of the scaling relations in eq. 2.44 for a constant value of m. The mass and radius of a ground state soliton are given by eq. 2.47. Similar relations can be computed for the excited states.

In a dark matter only context, the fact that excited state boson stars are unstable is well established. In fact, it can be proven analytically that the ground state is the

only SSS state with long time stability, at least in the low-field case (59). Generically, the excited states will decay via emission of scalar radiation until a stable soliton is formed. However, the presence of external gravitational potentials sourced from other matter can have non-trivial effects on the stability of the states. In principle, a sufficient amount of external gravity may allow some excited states to be stabilized. This has been demonstrated for the first excited state in (59).

How excited states may manifest themselves in a physical context is an interesting question. As seen in fig. 2.5, excited states have rotation curves which are naturally flat at large distance. This is quite appealing in regards to reproducing galactic rotation curves. The transient properties of excited states, such as their oscillation frequencies and interference patterns, may carry over into the dynamics of more complicated halos. Moreover, how superpositions of excited states might be seen in galactic halos is actively researched (6; 37). The modelling of rotation curves will be the primary focus of chapter 3, while a basic description of superposition states is discussed in chapter 4.

2.7 Real Scalar Field Oscillatons

The case of the SSS states in section 2.4 are strictly for a complex field. Real scalar fields do not admit time stationary solutions in the same sense. It is worth noting that real scalar fields do admit "quasi-breather" solutions which are approximately time periodic and approximately local in space; such solutions are referred to as "oscillatons." This was first demonstrated in (80). While the form of oscillatons from (80) was not analytically verified as a solution to the EKGEs, numerical solutions rapidly converge to the expected behavior. It is noted that the solutions may be only "quasi-periodic" in that non-linear effects may be able to alter the oscillation frequency. Nonetheless, (80) demonstrates the stability of oscillations on time scales which are orders of magnitude greater than the oscillation period. Moreover, such solutions were demonstrated to form under generic initial conditions, resulting from Jean instability. Oscillatons were further pursued in (91), which computed their

critical mass value as $\frac{0.607\hbar c^3}{Gm}$, which is quite similar to the critical mass in the case of complex scalars. (91) further pursued the study of oscillations and investigated the low-field version of oscillations, which can be described as a semi-analytic solution to the PSEs. As a final note, this thesis is primarily concerned with the case of complex scalars. Though the low-field limit of the real and complex cases coincide, real scalar oscillations could display distinct properties at the level of the EKGEs which might be relevant towards the growth of structure.

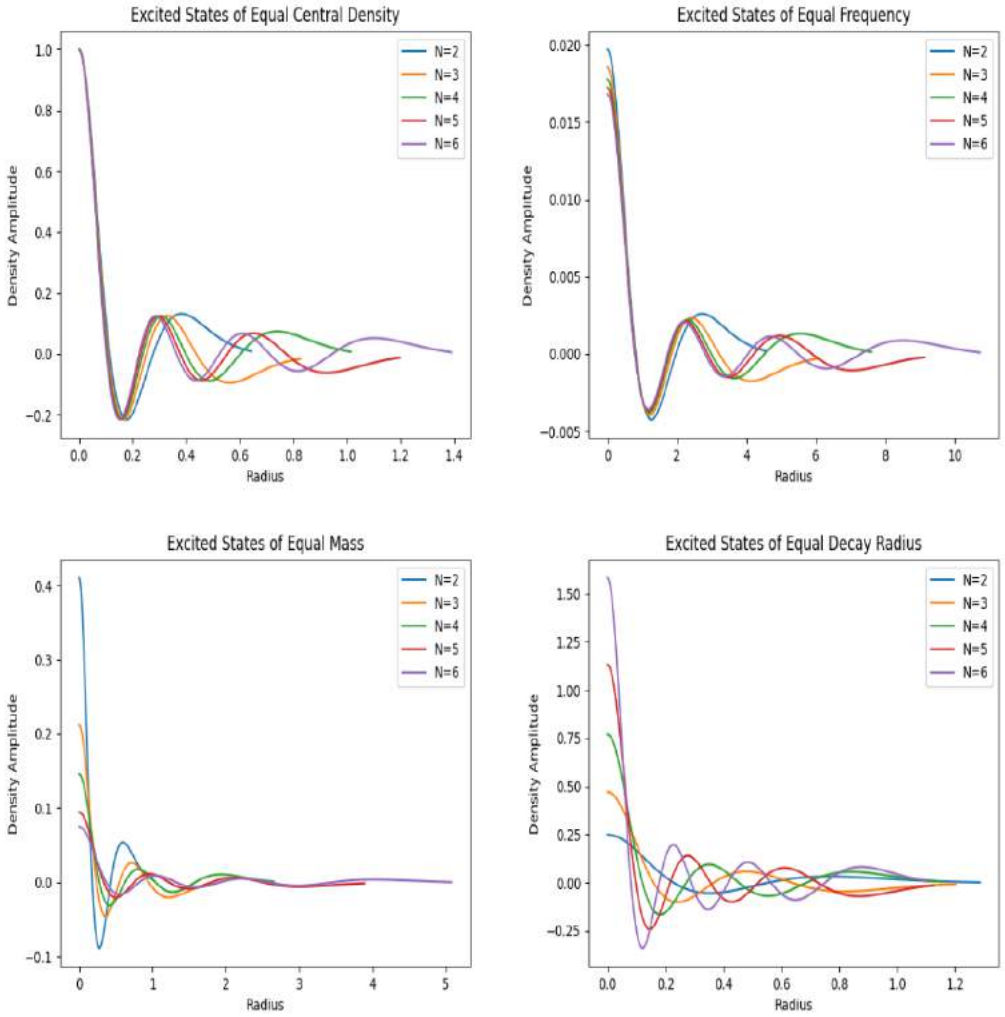

FIGURE 2.4: **Excited State Scalings:** Here we show excited state solutions of the SSS PSEs for $n \in [2, 6]$. Each panel applies a different scaling condition. (Top Left) States scaled to have the same central density. Higher excitation numbers in this case correspond to greater spatial extent. (Top Right) States scaled to have the same frequency value. The resulting solutions have central density decreasing with n. (Bottom Left) States scaled to have the same total mass. Generically, higher excitation numbers correspond to lower densities but greater spatial extent. (Bottom Right) States scaled to have the same value of decay radius R_d. In this case, higher excitation numbers correspond to halos with greater density and total mass.

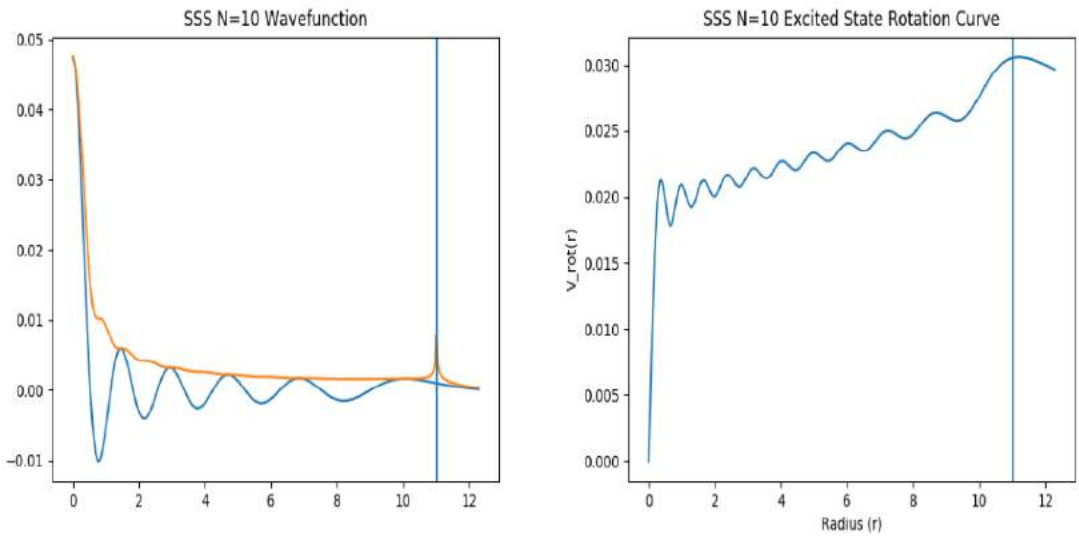

FIGURE 2.5: **SSS Excited State Rotation Curve:** Plot rendered with units of $m = 100$ and frequency $\omega = 0.999m$. The rotation curve of the $N = 10$ excited state and its wave function are shown. Left: The wave function along with its effective amplitude (see section 3.3.1). Right: The corresponding rotation curve. The rotation curve displays a step rise due to the high density soliton-like core. The rotation curve is then approximately flat, with a gradual rise. Once the decay radius (indicated by the vertical line) is reached, the rotation curve increases briefly, but then begins to fall once the majority of the mass is enclosed.

3

Wave Dark Matter and the Baryonic Tully-Fisher Relation

This chapter is a documentation of my own work,(39), regarding the Baryonic Tully-Fisher Relation (BTFR) and its relation to the Wave DM theory. In fact, we will see that Wave DM provides a unique motivation for the existence of this empirically measured relationship. This is a rather surprising result, and provides a novel model for the BTFR unique to Wave DM theory. We follow with a discussion of how this relation can be used to constrain the theory, placing a bound on the mass parameter m.

3.1 The Baryonic Tully-Fisher Relation

3.1.1 The Tully-Fisher Relation

The TFR (distinct from the BTFR) is an empirical relationship first reported in 1977 by Brent Tully and Richard Fisher, originally suggested as a measure for the distance to spiral-type galaxies (90). This relation states that the width of a spiral galaxy's 21cm spectral line, a distance independent observable, can be related to its absolute magnitude. This is particularly useful in that the derived absolute magnitude of the galaxy can then be compared to its apparent magnitude, providing a tool to measure

the distance to that galaxy.

The TFR, stated more formally, relates a spiral galaxy's absolute magnitude, L, to its 21cm spectral width, δ, through the following proportion, for some positive exponent, x:

$$L \propto \delta^x. \tag{3.1}$$

The galaxy's absolute magnitude can be converted to its total *stellar mass*, M_s through the stellar-mass-to-light ratio, Υ_*.

$$M_s = \Upsilon_* L \tag{3.2}$$

The galaxy's 21cm spectral width relates directly to its maximal rotational velocity, v_m. This can be understood as a result of the relativistic Doppler effect; one side of the galaxy will experience a redshift as it rotates "away from us" while the other side will experience a blueshift as it rotates "towards us," resulting in a spreading of the 21cm hydrogen emission line. For galaxies with an "edge-on" inclination, one expects the line width and rotational velocities to relate as

$$\delta \propto v_m. \tag{3.3}$$

Combining eqs. 3.1, 3.2 and 3.3, the TFR can be restated as a proportionality between a spiral galaxy's stellar mass and its rotational velocity. Put simply, it states that more massive spiral galaxies rotate faster.

$$M_s \propto v_m^x \tag{3.4}$$

3.1.2 The Baryonic Tully-Fisher Relation

The *Baryonic* TFR (BTFR) was suggested in 2000 by Stacy McGaugh (60) as a modified version of the original TFR. McGaugh noticed that the TFR, as stated in eq. 3.4, failed to describe low surface brightness (LSB) galaxies. This was explained by noting that LSB galaxies have a higher fraction of their mass contained in gas than do higher brightness spirals. Due to this higher gas fraction, LSB galaxies have greater rotational velocities than one would infer by only considering their measured stellar

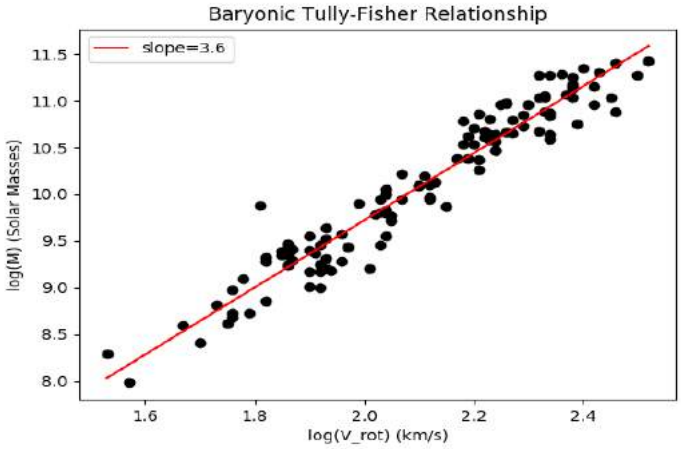

FIGURE 3.1: **Observed BTFR:** The BTFR as reported by the SPARC Survey (omitting error bars). On a logarithmic scale the relation appears as linear. This visualization assumes a stellar-light-to-mass ratio of $\Upsilon_* = 0.5\frac{M_\odot}{L_\odot}$. Qualitatively, higher values of Υ_* correspond to steeper slopes.

mass; the TFR therefore underestimates the velocities of LSB galaxies. McGaugh proposed that this issue could be resolved if one modified the relation of eq. 3.4 to include the *total baryonic mass*, M_b, of the galaxy instead of only its stellar mass. This results in the BTFR,

$$M_b \propto v_m^x. \tag{3.5}$$

The value of the BTFR exponent, x, is a topic worthy of discussion and an actively researched topic. Various systematic choices affect the inferred value of x. For instance, it is shown in (48) that the treatment of the stellar-mass-to-light ratio, Υ_*, directly impacts the measured value of x. More so, one would expect different galaxy samples to have different values of Υ_*, depending on their stellar content. Even further, the value of Υ_* may vary within individual galaxies (5), adding to the difficulty of determining a sample's mass distribution. It is suggested in (48) that this issue can be avoided, or at least remedied, by considering luminosity measurements in the near-infrared wavelength bands. Systematics aside, x usually takes some value between $x = 3$ and $x = 4$.

3.1.3 The SPARC Survey

In the later parts of this chapter, we will use a SFψDM model to compute a fit to the actual BTFR. This section is dedicated towards describing the observational data sample that we use for the fitting procedure, known as the Spitzer Photometry and Accurate Rotation Curves (SPARC) survey (49). SPARC consists of 175 extended rotation curves collected from the 21cm Hydrogen (H1) emission observations of several large surveys: the Westerbork Synthesis Ratio Telescope (WRST), the Very Large Array (VLA), the Australia Telescope Compact Array (ATCA), and the Giant Metrewave Radio Telescope (GMRT). The rotation curves are paired with infrared images from the Spitzer archive which detail the stellar distributions of the corresponding galaxies. The total sample contains both spiral and irregular galaxies, spanning 3 degrees of magnitude (dex) of surface brightness, 5 dex of stellar mass, and a variety of gas fractions.

Each galaxy in the SPARC survey is decomposed into its various mass components. The galaxy total mass is computed from the rotation curve by inverting the Newtonian rotational velocity, eq. 3.9. To infer the dark matter mass, one must then decompose this total into the DM and baryonic mass contributions.

$$M_{tot} = M_{DM} + M_B \tag{3.6}$$

SPARC reports the baryonic mass as decomposed into several components: gaseous mass, M_g, the mass of the stellar disk, M_s, and the stellar bulge, M_b. Described in detail in (49), this decomposition is computed as follows:

$$M_B = M_g + \Upsilon_* L_s + \Upsilon_b L_b. \tag{3.7}$$

Here, we have introduced the notation of the *stellar-light-to-mass ratios* represented by Υ_* and Υ_b. These ratios are used to convert observed luminosity data into data regarding total stellar mass. For instance, the stellar disk mass is computed as $M_s = \Upsilon_* L_s$. For most cases, it is a reasonable approximation to take $\Upsilon_b = \Upsilon_*$. However, some adjustments should be made for cases in which the stellar bulge is

particularly prominent. In those cases, SPARC uses the value of $\Upsilon_b = 1.4\Upsilon_*$.

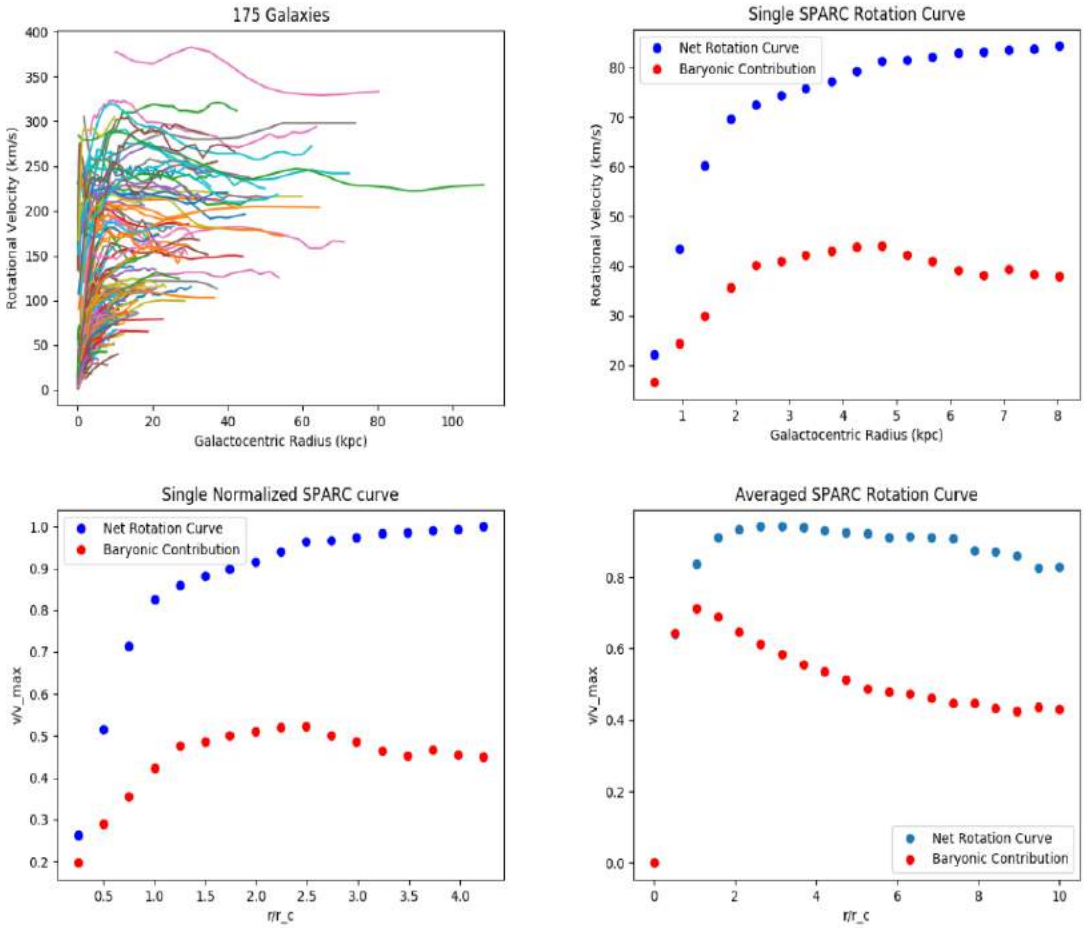

FIGURE 3.2: **SPARC Data Sample:** (Top left) All 175 SPARC Rotation Curves plotted in physical units. (Top right) A single rotation curve isolated from the survey and the corresponding contribution from baryons. (Bottom left) The same curve as in the top right, but parameterized in terms of the maximum circular velocity and core radius. (Bottom right) An equal weighting average of all SPARC curves. Average is computed by taking a spline of each rotation curve, and then averaging all splines for each value of $\frac{r}{r_c}$. If an individual curve lacks data at a radius, it is not included in the average for that radius. This is similar to the averaging procedure used in (24).

The stellar luminosities of each galaxy, L_s and L_b, are computed by performing a disk-bulge decomposition of its 3.6μm surface brightness distribution. The wavelength of 3.6μm is chosen for SPARC since it is expected that the value of Υ_* is approximately constant between galaxy samples at this value. The particular

decomposition used for SPARC assumes a stellar disk with an exponential vertical distribution and a stellar bulge with a strictly spherical distribution. It is noted that the uncertainties in this procedure are dominated by the value of Υ_* as opposed to the particular choice of geometry. Finally, the gaseous mass is inferred from H1 surface density profiles. To adjust for the presence of Helium, the total gaseous mass is taken to be a multiple of the total H1 mass $M_g = 1.33 M_{H1}$.

We use a specific set of 118 samples from the SPARC survey that were prepared in (48) to generate the observed BTFR. These samples were selected based on having flat rotation curves as well as small angles of inclination with respect to the line of sight. For the sake of preparing this sample, the total baryonic mass of each galaxy is estimated with the total luminosity in the 3.6μm band, $L_{[3.6]}$.

$$M_b = M_g + \Upsilon_* L_{[3.6]} \tag{3.8}$$

We note that this is equivalent to taking the assumption that $\Upsilon_b = \Upsilon_*$ in eq. 3.7. The corresponding circular velocity for the BTFR is extracted from that galaxy's SPARC rotation curve. (48) takes this velocity to be that of the "flat" part of the rotation curve and details an averaging procedure to compute this velocity. This procedure first computes the average of the two outermost points of the rotation curve; then, the average is recomputed by including the next outermost point, stopping the procedure once the next point differs by more than 5% of the previous average.

3.2 Wave Dark Matter and the BTFR

3.2.1 A Wave Dark Matter Tully-Fisher Relation

Though the BTFR describes a galaxy's baryonic mass content, the galaxy's rotational velocity is a function of its *total* mass content. This can be understood through the Newtonian formula for a galaxy's circular orbits, and therefore rotational velocity.

$$v(r) = \sqrt{\frac{M(r)}{r}} \tag{3.9}$$

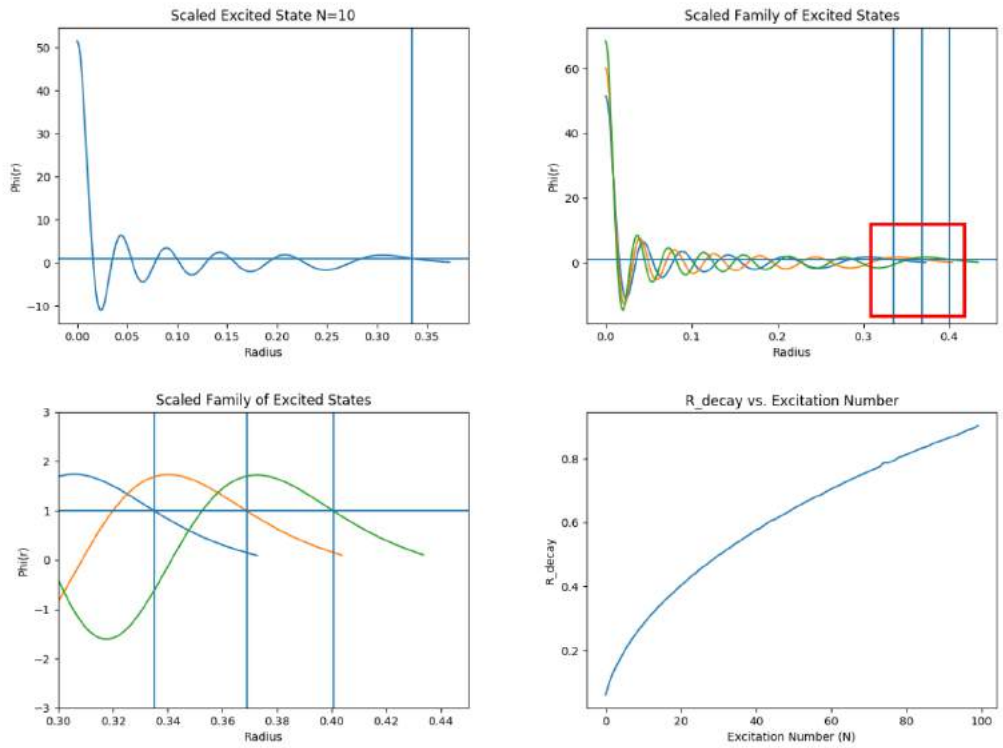

FIGURE 3.3: **Tully-Fisher Boundary Conditions:** A depiction of the boundary conditions applied by Goetz (35). Each excited state is scaled to have the same amplitude at its decay radius. (Top Left) A single excited state, vertical line denoting the decay radius, horizontal line denoting the boundary amplitude. (Top Right) Three consecutive excited states under the same boundary condition. (Bottom Left) Zoom of the red boxed region showing the boundary condition applied at each decay radius. (Bottom Right) The decay radii for this boundary problem increase empirically as $R_d \propto \sqrt{n}$.

The function $M(r)$ describes the total mass contained within a galactocentric radius of r. The maximal velocity from the BTFR, $v_m = \max(v(r))$, therefore depends both on the distribution of baryonic matter, as well as the distribution of dark matter. In fact, most galaxies have rotation curves which are highly dominated by the distribution of dark matter, with upwards of 90% of their mass being contained in the form of dark matter. In this regard, the BTFR, though observed through the dynamics of baryons, can be considered a result of the behavior of dark matter.

A possible connection between the BTFR and the Wave Dark Matter theory was observed in the thesis of Andrew Goetz (35). Goetz observed that a relationship

similar to the BTFR could be recovered from Wave-Dark Matter excited states. This relationship was recovered by imposing a particular type of boundary condition to the excited states at their decay radius (as defined in section 2.4). Formally, given an nth excited state radial wave function, Ψ_n, with decay radius R_n, the boundary condition is stated as

$$\Psi_n(R_n) = \bar{\Psi}. \tag{3.10}$$

In other words, fixing the same amplitude of the radial wave function at the decay radius for each excited state recovers a family of solutions which obey a *Tully-Fisher-Like* relationship for dark matter halos. That is, extracting the rotation curves from these states results in the following relational form for the excited states,

$$M_{n,tot} \propto v_{n,max}^{x}. \tag{3.11}$$

Even further, analytical arguments in (35) suggest that the boundary condition of eq. 3.10 produces a Tully-Fisher slope of $x \approx 3.4$ in the low field regime. Importantly, this boundary condition is always applied at the decay radius, marking the transition of the halo's oscillatory behavior to an exponential decay. In a qualitative sense, this boundary condition can be thought of as setting a density scale in the outer regions of the halo (seen in fig. 3.3), with the decay radius being the scaling point. In other words, at the decay radius, each excited state will have the same density given this condition. The relation corresponding to eq. 3.11 can be seen in fig. 3.4.

3.3 A Toy Model for a Wave Dark Matter Galaxies

The primary goal of this chapter is to simulate the BTFR using SFψDM theory in order to place a constraint on the SFψDM mass, m. We will compare and fit the simulation to the observed BTFR as reported by the SPARC survey. Since the BTFR relates a galaxy's baryonic mass to its rotational velocity, a quantity depending on both its baryonic *and* dark matter content, making this comparison will require us to provide a good model for both the baryonic and dark matter contributions of Tully-Fisher galaxies. We will organize this section into four primary parts: The first

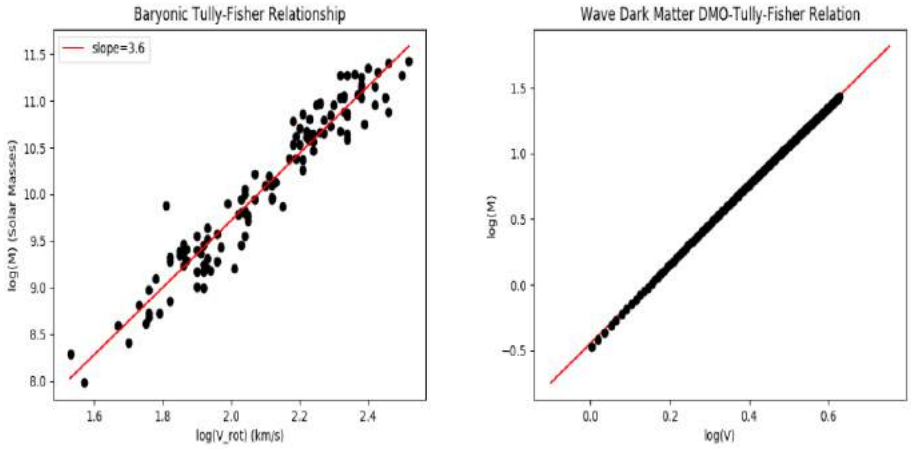

FIGURE 3.4: **SFψDM TF-like Relation:** Result of the boundary problem shown in fig. 3.3. (Left) Observed BTFR from SPARC. (Right)Dark matter only (DMO) analog of the BTFR generated from the first 200 solutions of the boundary problem. This illustrative case chooses $\bar{\Psi} = 1$. Slope of relation converges to 3.4 for large values of n.

part will describe how to model SFΨDM halos as generic solutions to the EKGEs; the second section will describe various quantities and properties of Spherically SSS SFψDM halos in a purely DM-only context; thirdly, we will discuss how to include a baryonic contribution at the level of the PSEs; finally, we will describe a SSS model for both components which will be used in the following to model the BTFR.

3.3.1 Generic SFψDM Halos

In section 1.4.4, we described SFψDM halos as complicated and turbulent wave structures. Simulations of halos formed in a bottom up fashion display finite density soliton cores surrounded by a region of fluctuating "quasiparticles" which eventually converges to an NFW-like profile. Our ultimate goal will be to model these halos with generic solutions to the EKGEs represented by a wavefunction $\psi(\vec{r}, t)$. The main difficulty in computing these solutions stems from the coupling of the Klein-Gordon equation to the spacetime metric determined by the Einstein equations. This results in non-linearity which is difficult to approach in a general context. We can attempt to circumvent this issue by fixing the spacetime metric and effectively decoupling the Klein-Gordon equation from the Einstein equations. In the case of

a fixed metric, the Klein-Gordon equation itself becomes linear. One could then expand the wavefunction $\psi(\vec{r}, t)$ as a linear combination of functions involving the spherical harmonics, $Y_l^m(\theta, \phi)$. For the case of a complex scalar field these terms appear as

$$\psi_{nl}^m(\vec{r}, t) = r^l Y_l^m(\theta, \phi)\Psi_{ln}(r)e^{i\omega_{nl}t}. \tag{3.12}$$

We note that a similar model has been used in (7) for the case of a real scalar field with a flat background metric. Hypothetically, if a halo resides in a fixed gravitational potential, one could compute the best linear combination of these functions to represent the halo. In reverse, understanding such solutions could give insight to the dynamics of halos.

As a first step towards understanding more general solutions to the EKGEs we consider the case of $l = 0$ for a single frequency. This results in the ansatz for the SSS states discussed in section 2.4.

$$\psi(\vec{r}, t) = \Psi(r)e^{-i\omega t} \tag{3.13}$$

Even reintroducing the coupling to the spacetime metric, the case of the SSS states can be categorized as in Chapter 2. Importantly, this provides a justification for modelling SFψDM halos as SSS excited states, at least to the leading order. We will explore the viability of using this leading order approximation in the context of producing the BTFR. Specifically, we will generate each halo with a single SSS excited state. In chapter 4, we will extend this discussion to include basic superpositions of such states.

3.3.2 Dark Matter Only SSS Halos

The SSS solutions described thus far are DMO states. Though ultimately we want to describe states which include baryonic matter, itemizing and understanding the properties in the DMO case is instructive and useful. We show an example of a DMO halo in fig. 3.5. Firstly, for the sake of simplicity, we will take SSS form of the PSEs in eqs. 2.50 - 2.52. We identify the following quantities:

- m: The SFψDM particle mass.
- $\psi(r,t)$: The halo total wavefunction.
- $\Psi(r)$: The radial wavefunction component.
- $V(r)$: The halo gravitational potential.
- $M(r)$: The DM mass contained within a sphere of radius r.
- n: The SSS state excitation number.
- $v_{circ}(r) = \sqrt{\frac{M(r)}{r}}$: The velocity of a circular orbit at radius r.
- ω: The static state frequency.
- $\rho(r) = \Psi(r)^2$: The DM density.
- $k^2(r) = -2m(m - \omega + mV(r))$: The halo spatial frequency.
- $\lambda(r) = \frac{2\pi}{k(r)}$: The halo local wavelength.
- $A^2(r) = \Psi^2(r) + \frac{\Psi_r^2}{k^2(r)}$: The wavefunction amplitude (described below).
- R_d: The decay radius specified by $k(R_d) = 0$.
- $\lim_{r\to\infty} M(r) = M_{tot}$: The total DM mass.
- $\lim_{r\to\infty} V(r) = V_\infty$: Potential at infinity set by convention.

The set $\{\Psi(r), V(r), M(r), \omega\}$ describes a physically reasonable solution if V_∞, M_{tot}, and $\Psi(r)$ are finite. Moreover, to avoid singular behavior at the origin, $\Psi_r(0) = M(0) = 0$ must be enforced. The only such solutions are the SSS states as described in section 2.4. The value of V_∞ is a convention; we will take the usual value of $V_\infty = 0$. It should be noted that the ability to shift V_∞ by a constant remains a useful feature of this set of ODEs.

The wavelength and amplitude functions, $\lambda(r)$ and $A(r)$, are constructed specifically for the purpose of modelling the BTFR. The main reason for this is that the quantity $\lambda^2 A$ forms a scale invariant which will be useful for applying halo boundary conditions. Discussion of this quantity is contained later in section 3.4.2. The amplitude function is constructed by assuming the radial wavefunction to have local behavior similar to the following

$$\Psi(r+R) = A(R)\sin(k(R)r + \delta(R)) \tag{3.14}$$

This essentially decomposes the oscillating behavior from its amplitude, at least in an approximate sense. The wavelength quantity is a direct result of the form of the ODE in eq. 2.52. Importantly, the wavelength and amplitude quantities diverge and begin to lose their physical interpretations at the decay radius, R_d since $k(R_d) = 0$. This is merely a result of the transition of the wavefunction from its oscillating behavior to its exponentially decaying behavior. The value of ω can be related to the total mass of the halo. For the case of a fixed excitation number, n, and assuming $V_\infty = 0$, smaller values of ω will correspond to halos with a greater total mass. This can be understood by considering the energy eigenvalue of the wavefunction ψ at the level of the Schrödinger equation. The energy relates to ω as $E \propto (m - \omega)$. Smaller ω then correspond to greater energy and therefore larger total mass. Interestingly, for a fixed value of ω, the mass of halos scales in an approximately linear fashion with excitation number (36).

$$M_\omega(n) \approx (n+1)M_\omega(0) \tag{3.15}$$

3.4 On Halo Boundary Conditions

3.4.1 Physical Motivation

As described in section 3.2 and (35), the global properties of SFψDM excited states can vary greatly depending on the imposed boundary conditions. Importantly, choosing the boundary condition of eq. 3.10 which is imposed at the halo decay radius reproduces a trend very similar to the BTFR. We wish to specify a set of physically

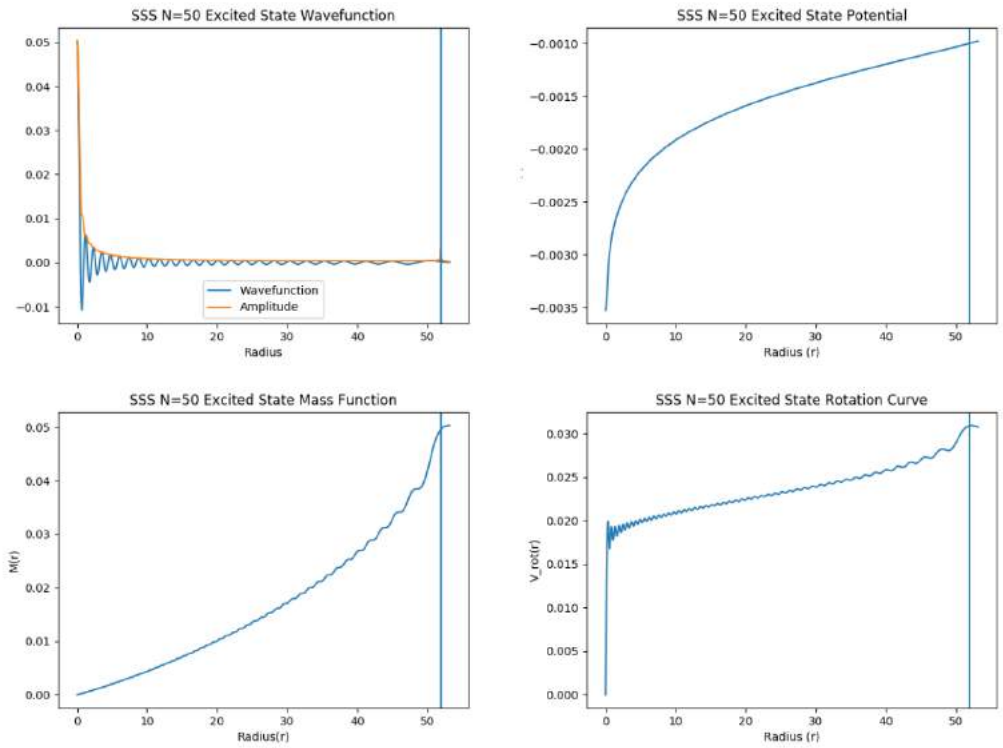

FIGURE 3.5: **Example DM-Only Halo:** Example of the $n = 50$ SSS Excited state. State prepared with units of $m = 100$ and $\omega = 0.999m$ for ease of computation. All vertical lines correspond to the decay radius R_d. (Top left) Radial wavefunction and corresponding amplitude function as defined in section 3.3.1. (Top right) Corresponding gravitational potential using the convention $V_\infty = 0$. (Bottom left) The mass function. (Bottom Right) The rotation curve.

motivated boundary conditions that will reproduce this property that can be applied to our model of the BTFR.

In fig. 3.6, we depict a SFψDM halo as an N-body system of DM particles (or quasiparticle fluctuations). This image will serve as the *motivation* for our boundary conditions. We compare this to an N-body system of stars forming a globular cluster. Though these two systems would occur at vastly different physical scales, we only wish to compare the qualitative properties resulting from the N-body dynamics. In the central region of the halo, the individual DM particles overlap significantly due to their number density. In comparison, the particles in the outer region are further separated and can be seen as individual points. We suggest that SFψDM

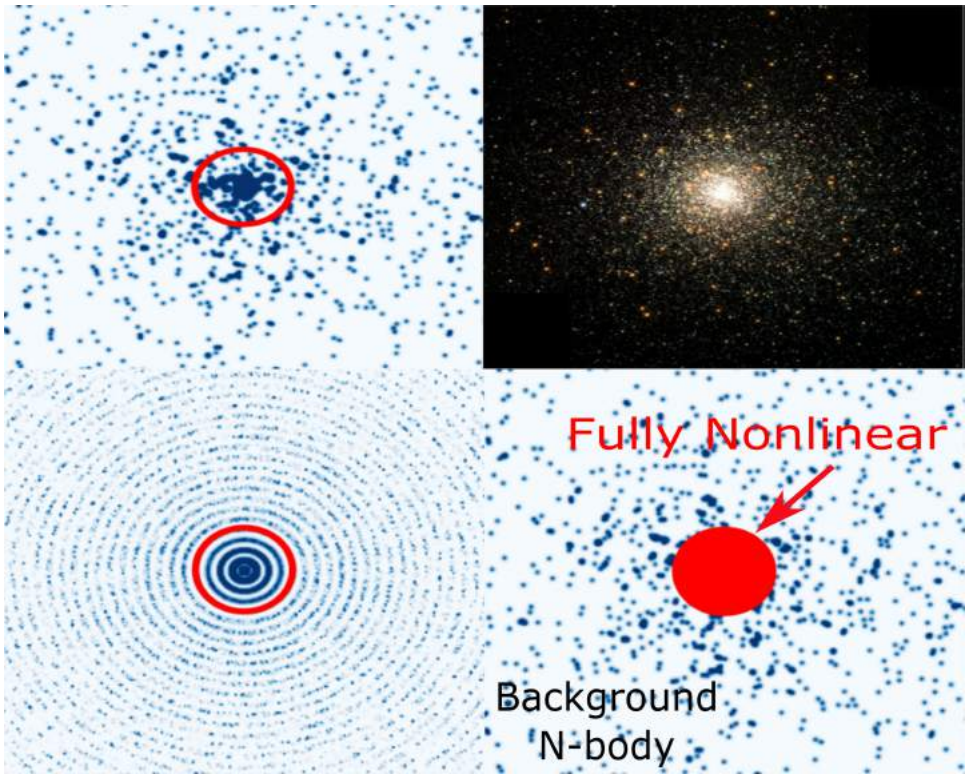

FIGURE 3.6: **Background Boundary Conditions:** A motivation for SFψDM boundary conditions. Top left: A system of DM particles placed to emulate an N-body system; particles are uniformly distributed by radius, and randomly distributed by angle. Saturation effects are applied for visualization. Top right: A globular cluster demonstrating a real N-body system. Bottom left: The same as the top left image, but distributed uniformly in angle to compare to a spherically symmetric setting. Bottom right: A possible description of SFψDM halos. As seen in the top left image, the particles become densely packed in the central regions of the halo resulting in a large amount of interference and overlap. In the bottom left image, we can identify the radius at which the particles begin to display substantial overlap, this is shown with a red circle. Outside of this boundary the particles can be individually resolved while inside the boundary they cannot. The bottom right image suggests describing the central region as a fully nonlinear solution to the EKGEs, characterized by the overlap of the halo's many DM particles. The outer region of the halo can then be thought of as an N-body problem of DM particles evolving in the gravitational well of the halo.

halos display a boundary between two such regions, indicated by the red circle in the figure.

We depict the same image in a spherically symmetrized setting in the bottom left panel. Importantly, the number density of the DM particles becomes great enough in comparison to the particle size that the particles begin to overlap. We suggest that the particle size and density are related to the wavelength and density of the aggregate DM halo. Denoting the amplitude and wavelength scales as ρ_{DM} and λ_{DM} this gives us our first notion of a galactic boundary condition. That is, at some generic radius depending on the halo, R, the halo has a preferred scale

$$(\rho(R), \lambda(R)) = (\rho_{DM}, \lambda_{DM}). \tag{3.16}$$

We then account for the fact that the halo itself will display density oscillations of the order ρ_{DM} by considering the amplitude function, $A(r)$, as opposed to the wavefunction. We therefore define a boundary value A_{DM}, and propose the boundary problem to be

$$(A(R), \lambda(R)) = (A_{DM}, \lambda_{DM}). \tag{3.17}$$

Finally, we present a more generic depiction of our boundary condition in the bottom right panel of fig. 3.6. Conceptually this can be thought of as follows: DM particles are sufficiently dispersed in the outer regions of the halo, and thus form an approximate N-body system. Eventually, as one moves towards the center region, the particles begin to significantly overlap and can no longer be individually resolved. This overlap causes a non-linear interference between the particles and should be thought of as being governed by the EKGEs.

As a last point regarding fig. 3.6, we note that there are various interpretations of the DM particles. It is a tempting analogy to think of each DM particle as a SFψDM soliton since the soliton state is the only truly stable SFψDM configuration. On the other hand, such an interpretation has never been realized in simulation. Simulations of halos formed in a bottom-up fashion from solitons generally display an outer region populated with quasiparticle fluctuations. In regards to our boundary

condition, the values of λ_{DM} and A_{DM} should reflect the relative size and amplitude of these quasiparticles. It is a separate question to ask whether or not sufficient quasiparticle fluctuations can result in the condensation of solitons within galactic halos. This has never been demonstrated, though one would expect this process to occur if the quasiparticle region reaches the "kinetic regime" as in (50). This becomes more and more likely at higher values of the m where the quasiparticle wavelength becomes smaller in comparison to the overall halo. Further, in the case that SFψDM has a self interaction term, it has been shown that multiple solitons can form within a halo (11). This then begs the question "Does soliton condensation occur within galactic halos, and if so does it have a preferred length scale?"

3.4.2 Amplitude-Wavelength Boundary Conditions

We now detail the boundary problem which we will solve in order to generate the BTFR. We wish to fix the amplitude and wavelength scales of the SSS states following the discussion of the prior section. This requirement can be stated as

$$A_n(R_n) = A_{DM} \tag{3.18}$$

$$\lambda_n(R_n) = \lambda_{DM}. \tag{3.19}$$

In other words, we wish to choose some characteristic scales denoted by A_{DM} and λ_{DM}, and fix them at some *generic value* of radius R_n for each excited state. This boundary problem can be straightforwardly solved using shooting problem methods. However, it is faster and more revealing to make use of the PS scaling relationships described in section 2.5.4. Firstly, we will consider scalings for the case of a fixed boson mass, m. This is equivalent to taking the rescaling parameter $\beta = 1$ in eq. 2.44. As a result of the scaling relationships in eq. 2.44, we can define a function based on the amplitude and wavelength functions which is invariant upon rescalings for constant values m.

$$I_n(x) = \lambda_n^2(x) A_n(x) \tag{3.20}$$

Here, for convenience, we define the dimensionless radius, x, as the fraction of the decay radius, $x = \frac{r}{R_{d,n}}$. The boundary problem posed in eq. 3.17 can then be solved by locating the characteristic radii, X_n, for each excited state which allows the following product condition be satisfied.

$$I_n(X_n) = I_{DM} = \lambda_{DM}^2 A_{DM} = \lambda^2(X_n)A(X_n) \tag{3.21}$$

Once each radius, X_n, is found, we identify this point as the scaling boundary. While this radius ensures λ and A have the correct product, it does not necessarily ensure the individually desired values of λ_{DM} and A_{DM}. To completely solve the boundary problem and produce the correct amplitude and wavelength for the excited state boundary, one then applies the scaling relations in eq. 2.44 so that the correct values are attained.

To summarize, we can use the following procedure to solve the boundary problem for a particular excited state: (1) Choose a value of m and boundary values for A_{DM}, λ_{DM}; (2) Compute a SSS excited state of order n; (3) Compute the function $I_n(x)$ for that state; (4) Find the intersection of $I(x)$ with I_{DM} and denote this intersection point as X_n; (5) Choose a value of the scaling parameter α which gives the excited state the appropriate value of A_{DM}.

We depict a family of Amplitude-Wavelength functions, eq. 3.20, and the corresponding boundary value in fig. 3.7. In the left panel we depict the boundary problem with a single excited state. On the right panel we show the corresponding functions for the first 25 excited states. The functions $I_n(X_n)$ display several features which have important implications for the boundary problem in eq. 3.17: Each I_n has a minimum value and also diverges at the decay radius $X_n = 1$. The divergence at $X_n = 1$ can be easily understood as due to the divergence of λ_{DM} and A_{DM} at the decay radius. Further, for any given $n = N$, $I_N(X_N)$ bounds all the $I_n(X_n)$ of greater excitation number from above. That is, $I_N(X) > I_n(X)$ for all $n > N$. This property is an observed trend from on our computational results. In combination with each I_n having a global minimum, this feature allows one to determine whether or not a

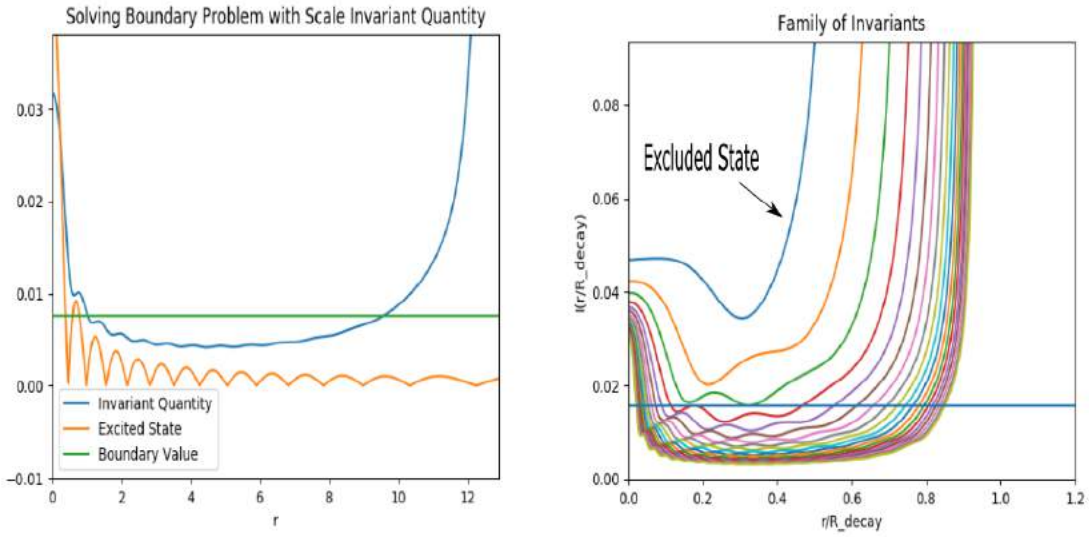

FIGURE 3.7: **Amplitude-Wavelength Functions:** (Left) The Amplitude-Wavelength boundary problem plotted for a single excited state. The excited state density as well as the invariant corresponding to eq. 3.20. (Right) The family of excited state invariants for a fixed m. Each excited state is bounded by above by the prior state. All states display a divergence at the decay radius. Some states can be excluded from the boundary problem by the choice of I_{DM}, as they will display no real intersection.

particular I_n is capable of achieving the prescribed boundary value. If $I_{DM} < I_{N,min}$, then the state will never intersect the boundary value and can therefore never achieve the prescribed values. Further, all other states with $n < N$ will have the same issue. One could, in principle, use this to exclude low excitation states from the family of solutions by appropriately decreasing I_{DM}.

Given a state I_N and a value of $I_{DM} > I_{N,min}$, there will be two values of X_N which are candidates for the boundary radius defined by the two intersections of I_{DM} with I_N. We note that applying the boundary condition at the leftmost intersection point, closest to the origin, *does not reproduce a BTFR-like relation.* This is due to the fact that the intersection points for successive values of N will be at smaller and smaller values of X_n, making the boundary radius a smaller fraction of the overall halo size. This directly conflicts with the expectation of more massive galaxies to have higher excitation and therefore greater spatial extent. For these reasons, we do

not consider the leftmost intersection. The rightmost intersection point generically occurs in the outer regions of the DM halo. In fact, as one takes the limit of $n \to \infty$, the intersection point limits to the decay radius $X_n = 1$. This will generate the same boundary problem as investigated by Goetz in eq. 3.10, scaling the DM halos at their decay radius. Further, this implies that the prescribed value of I_{DM} will not affect the limiting behavior of the boundary problem as long as $I_{DM} > 0$ is strictly enforced.

3.5 Including Baryonic Contributions in SSS States

Though the gravity which generates a galaxy's rotation curve is mostly sourced from DM, the BTFR directly relates the rotation curve to the galaxy's baryonic content. Simulating the BTFR for SFψDM will therefore require us provide a working description of that baryonic content as well as how it alters the shape of the DM halo. At the level of the PS system, this can be thought of as including additional sources of gravity via the gravitational potential, V. Thus, we will consider the inclusion of spherical external densities, ρ_{ext}. The corresponding gravitational potential, V_{ext}, is taken to be a solution to the Poisson Equation

$$\nabla^2 V_{ext} = 4\pi\rho_{ext}. \tag{3.22}$$

We then reach a slightly modified version of the PSEs which include this gravitational potential.

$$i\frac{\partial\psi}{\partial t} = -\frac{1}{2m}\nabla^2\psi + m(V + V_{ext})\psi \tag{3.23}$$

$$\nabla^2(V + V_{ext}) = 4\pi(|\psi|^2 + \rho_{ext}) \tag{3.24}$$

Given that the SSS SFψDM states described in the prior sections reproduce such a promising trend in their rotation curves, we would like to preserve the SSS ansatz as much as possible. To achieve this, we still assume the DM wavefunction ψ to have the SSS form from eq. 2.22. In addition, we consider external densities which are as well spherical and static, $\rho_{ext}(r)$. We therefore reach the analogous versions of eqs.

2.26 and 2.27 but with an external baryonic contribution.

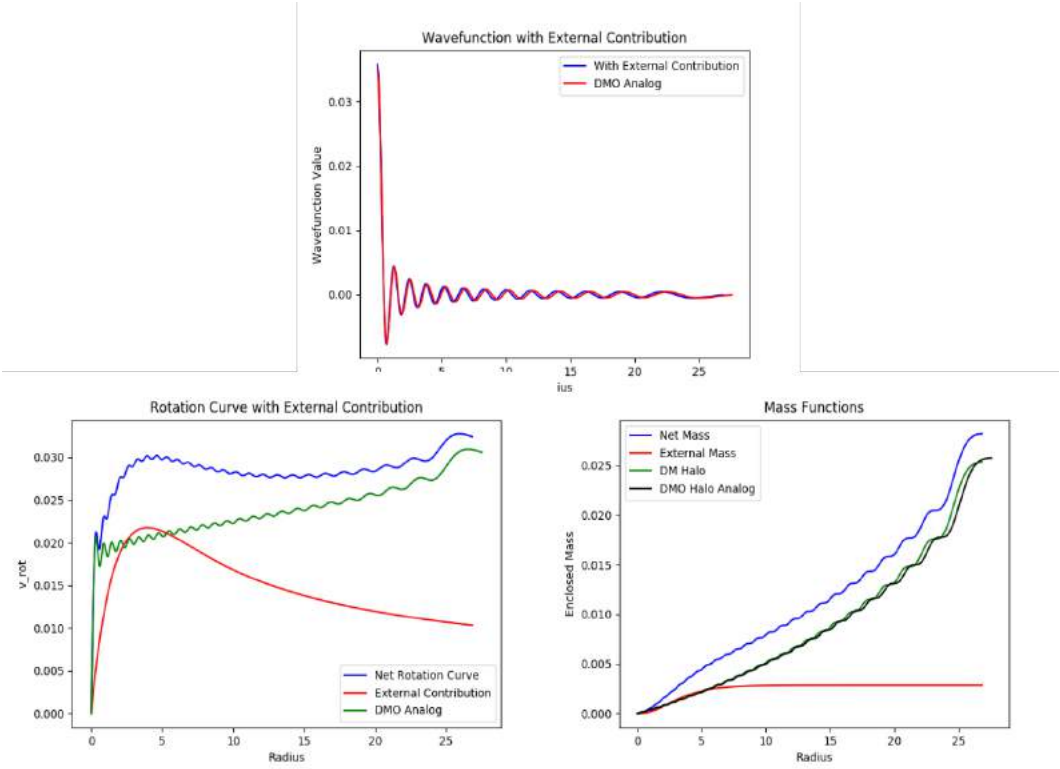

FIGURE 3.8: **SFψDM Halo with Baryonic Contribution:** Figures rendered using units of c = G = $\hbar$ = 1, m = 100, and frequency of ω = 99.9. The effects of including additional matter contributions. An external density of $\rho(r) = Ke^{-Cr}$ (described later in section 3.6.1) is used. Total dark matter fraction is set to 90%. The DM fraction at the baryon half mass radius is set to 50%. Top: The overall DM wavefunction displays minimal change from the inclusion of the external component. Bottom left: Including external components can greatly affect the overall shape of the rotation curve. Sizeable contributions near the central region tend to flatten the overall rotation curve. An analogous DMO halo is included for comparison. Bottom right: Mass functions corresponding to the top two plots, again including a DMO analog. A contraction of the overall galaxy as a result of including the external matter is evident, and can be seen by comparing the two DM halos.

This ansatz now describes a SSS distribution of DM, represented by the wavefunction ψ, under the influence of SSS external potential sourced by ρ_{ext}. The solutions to these equations should be thought of as similar to those of the DM-only setting but with alterations in shape which depend on the relative size and distribution of

the external density in comparison to the DM density. An example of such an alteration is shown in fig. 3.8. In most galactic contexts, the relatively small ratio of baryonic mass to DM mass will result in small changes to the overall solution for ψ in comparison to the DM-only setting. However, the resulting appearance of the rotation curve can change significantly, even from small external contributions.

Computing the analog of SSS excited states in the presence of a background baryon density can be achieved with similar methods to the DM-only case. Using a method similar to (59), we compute these states by the use of a continuation parameter, γ. That is, we solve the system in eqs. 2.50-2.52 with the substitutions of

$$M \to M + \gamma M_{ext} \tag{3.25}$$

$$V \to V + \gamma V_{ext} \tag{3.26}$$

The parameter γ is initially set to 0, resulting in a DM-only state. Then, the value of γ is increased in small increments and the system is resolved until $\gamma = 1$, including the full external contribution. Otherwise, the solving routines are analogous the the DMO case in the Appendix.

Later, once we compute solutions with appropriate baryonic contributions, we will want to rescale the solutions to match the observed BTFR. In this case, we need to make use of the scaling relations of the PSEs in section 2.5.4. This can be achieved as long as the same relations are applied to the external components V_{ext} and ρ_{ext}. That is, as long as the external density and potential are rescaled in the same way as their DM analogs, then the scaling relations can be applied.

3.6 Modelling the BTFR with SSS Excited States

In this section we detail a particular method for using the BTFR to constrain the mass parameter of the SFψDM theory, m. This method will combine the various aspects of the SSS excited states discussed so far. Described briefly, we solve for the SSS excited states in the presence of a static baryon density. We will choose

the baryonic component to have mass fractions comparable with observation and well known galactic simulations. Finally, we will apply a version of the Amplitude-Wavelength boundary condition detailed in section 3.4.2 to each excited state in order to fix the density scale of the halo's outer regions. We then extract the relevant velocity and mass data and vary this boundary condition until a best fit to the observed BTFR is reached.

3.6.1 Spherical Baryonic Contributions

First, we choose the baryonic component to be spherically symmetric and static so that the methods from the prior section can be applied to the excited states. Specifically, we choose the external baryonic density to be of the following exponential form

$$\rho_{ext}(r) = Ke^{-Cr}. \tag{3.27}$$

Assuming that this distribution solves the Poisson equation, it corresponds to a gravitational potential of

$$V_{ext}(r) = \frac{-4\pi K}{C^3}\left(\frac{2}{r}(1-e^{-Cr}) - Ce^{-Cr}\right). \tag{3.28}$$

Conveniently, the values of K and C relate to the total mass and the effective radius of the external baryonic component. Solving for the total mass and half mass radius of this distribution yields

$$M_{ext,tot} = \frac{8\pi K}{C^3} \tag{3.29}$$

$$R_{ext,h} = \frac{2.67}{C}. \tag{3.30}$$

In order to choose values for C and K, we will fix the values of the total dark matter fraction, $f_{tot} = \frac{M_{DM}}{M_{tot}}$ and the dark matter fraction at the baryon half mass radius from eq. 3.30, f_h. This can be achieved through standard shooting problem methods. We will sample fractions which are consistent with the IllustrisTNG simulations in (52), using fractions in the ranges of $f_{tot} \in [0.7, 0.9]$ and $f_h \in [0.5, 0.9]$.

To summarize, we compute SSS excited states, paired with an appropriately proportioned baryonic density with the following procedure: (1) Choose target values for f_{tot} and f_h and compute the excited state without an external contribution. (2) Choose the constant C for the external contribution to be some reasonable value in comparison to the length scale of the excited state. (3) Compute a value of K which gives the correct total external mass such that the desired fraction f_{tot} is satisfied. (4) Using the chosen values of K and C, include the external density via the continuation parameter method described in section 3.5. (5) Extract the attained values for f_{tot} and f_h. The value of f_{tot} should be close to the target but f_h may or may not. (6) Adjust the values of C and iterate starting at step (2) so that the attained f_h is closer to the target. Usually, a larger value of C will correspond to a larger value of f_h. (7) Repeat this procedure until the desired fractions are reached.

3.6.2 Applying Boundary Conditions

The SSS states with their external baryonic components can be computed as in the prior section at any convenient scale. For instance, we choose to first compute the states for a constant value of the frequency parameter ω in order to simplify the computational routine. We will wish to apply scalings so that the family of excited states reproduces a BTFR, similar to the relation described in section 3.2. Specifically, for each value of the mass parameter, we will apply the Amplitude-Wavelength boundary condition to fix the amplitudes of the excited states at some large radii.

Once the SSS states and their corresponding baryon distribution are found, the process for solving this boundary problem is rather straightforward. We first choose a value for $m^{-1}I_{DM} = \lambda_{DM}^2 A_{DM}$. Specifically, we choose a value which is sufficiently large so that no SSS states are excluded from the boundary problem as described in section 3.5. Using computational units of $m = 100$, we find that a value of $m^{-1}I_{DM} = 0.4$ suffices for this purpose. We then compute the function $I(x)$ as defined in section 3.4.2 for each excited state, find its outermost intersection with I_{DM}, and use this intersection point as a scaling point. We then specify the value of

A_{DM} and scale each state to have that amplitude at the scaling point. The result is a family of excited states with similar amplitude and wavelength scales in the outer regions that also reproduces a BTFR-like relation.

3.6.3 Fitting the BTFR and Constraining m

For each value of m, the prescribed value of A_{DM} will determine the physical scale of the corresponding DM halos and baryonic distributions. This will directly correspond to a scaling of the baryonic mass and rotational velocity corresponding to the BTFR. Solving by using the scaling relations of eq. 2.44, the scaling of $A_{DM} \rightarrow \alpha A_{DM}$ corresponds to taking $\{M_{ext}, v_{rot}\} \rightarrow \{\alpha^{1/2} M_{ext}, \alpha^{1/2} v_{rot}\}$. Since the baryonic mass and rotational velocity are both scaled by the same factor, the result on the BTFR is a simple translation in logarithmic space. In other words, it takes $\{\log(M_{ext}), \log(v_{rot})\} \rightarrow \{\log(M_{ext}) + \frac{1}{2}\log(\alpha), \log(v_{ext}) + \frac{1}{2}\log(\alpha)\}$, effectively transposing each point of the relation by the same vector in log space. As a result, for each value of m there will be a best fit value of A_{DM} which will overlap with the observed BTFR. This procedure is demonstrated in fig. 3.9.

The most striking and useful feature of the prescribed boundary condition is that one can exclude certain values of m based on its best fit to the BTFR. This is due to the fact that as m decreases, the excited states corresponding to a best fit tend to have larger masses for any given excitation number. As a result, if m is chosen to be too small, then all of the excited states will have masses larger than the smallest observed members of the SPARC data set. We use this to place a lower bound on m. As seen in fig. 3.10, masses of the order $m = 10^{-24} eV$ are not capable of describing the lower mass end of the BTFR. Depending on how one defines the criteria for modelling the BTFR one may derive different lower bounds. For instance, if one supposes that Tully-Fisher galaxies be modelled by excited states with $n \geqslant 2$ then one can push the bound up to $10^{-22} eV$. In general, BTFRs produced by more highly excited states are consistent with greater values for m.

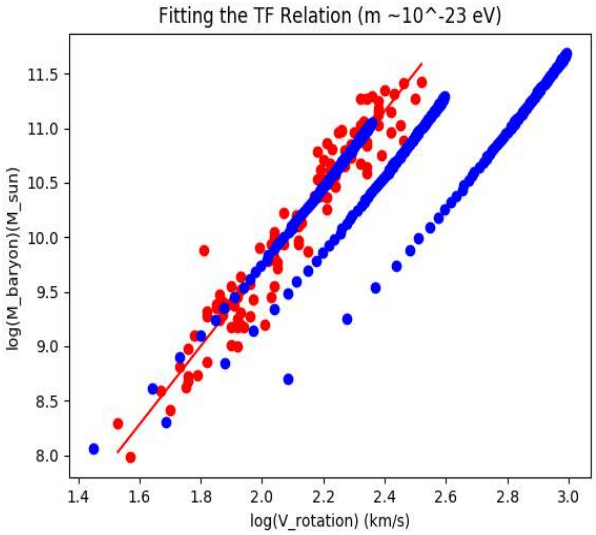

FIGURE 3.9: **Fitting the BTFR via Boundary Conditions:** An example of the fitting routine for the BTFR using $m = 10^{-23}$eV. First, the boundary problem is imposed on sequence of excited states, resulting in a BTFR-like relation. Next, the boundary values are adjusted until the simulated relation overlaps the data (shown as the progression of the 3 simulations in blue). Scaling the boundary values shifts the entire relation, maintaining its slope. The relation extends indefinitely towards higher masses, but the minimum mass is bounded from below by the ground state profile.

3.7 Results and Discussion

The following subsections discuss various results and features of our BTFR model. In addition to the constraints on the particle mass, our main results are included in figs. 3.13, 3.12, 3.10 and 3.11. In fig. 3.11, we consider the affects of changing the total DM fraction of each simulated galaxy. We conclude that this results in rather negligible change to our computed fits to the BTFR. In fig. 3.13 we compare our simulated rotation curves to those of the SPARC survey. Specifically, we normalize and average our results in the same manner as described in figure 3.2. Lastly, in fig. 3.12, we show the dependence of BTFR properties on the state excitation number. Namely, we extract the dependence of the baryonic mass content and circular velocity corresponding to the BTFR. In addition, we extract a relation between the excitation number and the scale of the DM fluctuations corresponding to the red boundary in

fig. 3.6.

3.7.1 Bounds on m

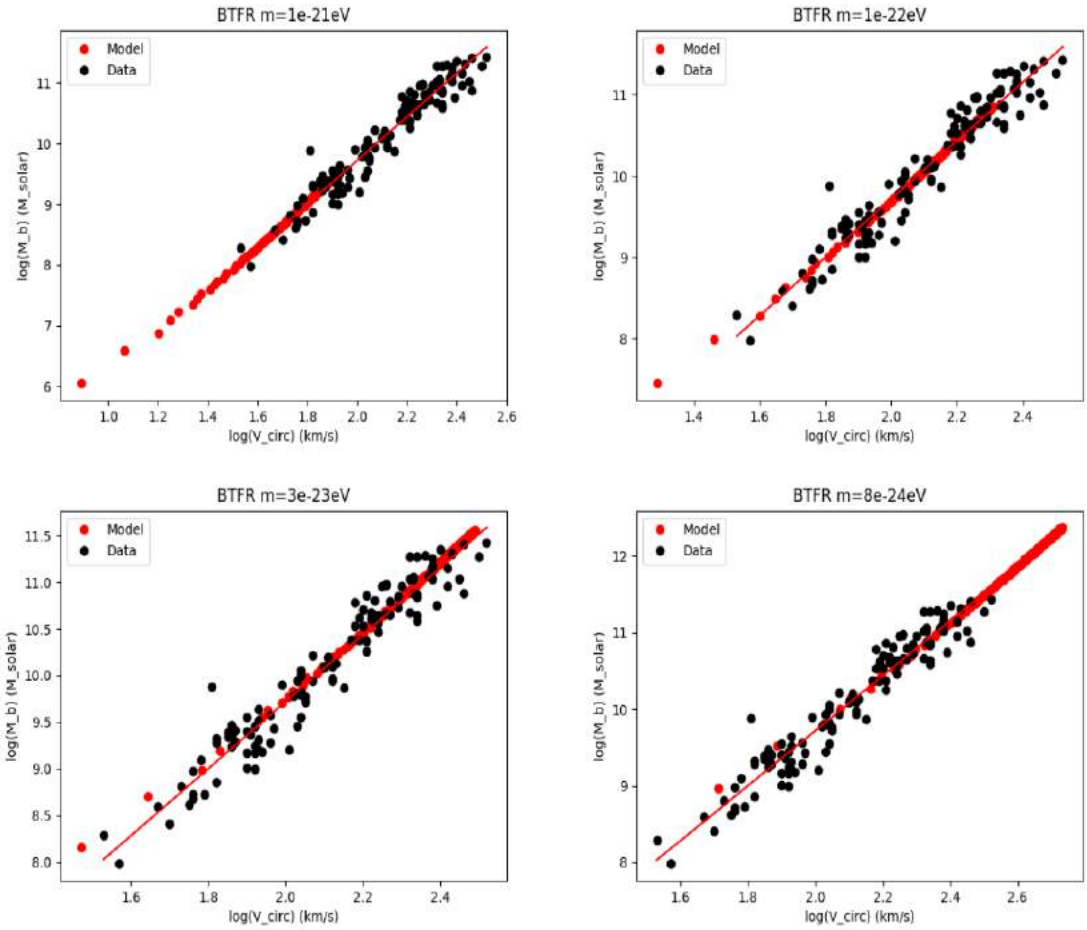

FIGURE 3.10: **BTFR Fits:** Example fittings of the BTFR for multiple values of the SFψDM mass, m. Generically, higher values of m correspond to smaller overall masses, shifting the simulated fit towards the lower mass region. For sufficiently small mass values, the simulated fit does not overlap the observed data points (see the bottom right panel). This allows one to constrain the possible values of m. For instance, assuming states $n \geqslant 0$ results in a constraint of $m \geqslant 10^{-23}$ whereas assuming $n \geqslant 3$ results in $m \geqslant 10^{-22}$. The first 200 excited states are used for generating the plot. Using more states will extend the linear trend further into the high mass regimes.

Returning to fig. 3.10, we observe that each value of m has a corresponding best fit to the BTFR. Qualitatively, larger values of excitation number correspond to larger galaxies in our simulations. The lowest excitation numbers therefore provide a lower bound on the rotational velocities and mass values which are consistent with modelling the BTFR using SSS states. Decreasing the value of m results in halos which are more and more massive for a fixed value of n. Eventually, for sufficiently small m values, there will be no SSS excited states which are small enough to overlap with the lower mass end of the observed BTFR.

We conservatively determine a bound of $m \geqslant 10^{-23}$eV. This is achieved by taking the criteria that the BTFR must be modelled by states with $n \geqslant 1$. In other words, we observed that the $n \geqslant 1$ state overlaps the smallest mass data point of the SPARC survey at $m = 10^{-23}$eV, and becomes too massive once m is further decreased. By strengthening the criterion for n, one can push this lower bound to higher values. For instance, if we take $n \geqslant 3$, the bound becomes $m \geqslant 10^{-22}$eV. In addition to placing a lower bound of m by choosing a lower bound on n, one could hypothetically place an upper bound on m by enforcing some upper bound on n for Tully-Fisher galaxies. To summarize, restricting the range of allowed n restricts the range of allowed values for m. Conversely, stating a range of possible values for m could allow one to estimate the excitation numbers of Tully-Fisher galaxies.

This constraint on m remains true even when varying the relevant DM fractions of the simulated galaxies. The value of the half-fraction, f_h, does not affect the overall fit. This is due to the fact that the baryon half mass radius almost always occurs at a radius much smaller than the radius at which the flat rotational velocity is measured, and therefore does not change the measured value. This is consistent with the rotation curves in the SPARC survey. Changing the total DM fraction, f_{tot}, can change the overall fit to the BTFR, though the range of potential values for f_{tot} is too small to make a qualitative difference. This is depicted in fig. 3.11. Adjusting f_{tot} will adjust the value of the rotational velocity and therefore shift the fit. In principle, this can change the bound on m. However, observed values of f_{tot} lie in a narrow range, making this effect rather negligible for the purposes of fitting

the BTFR.

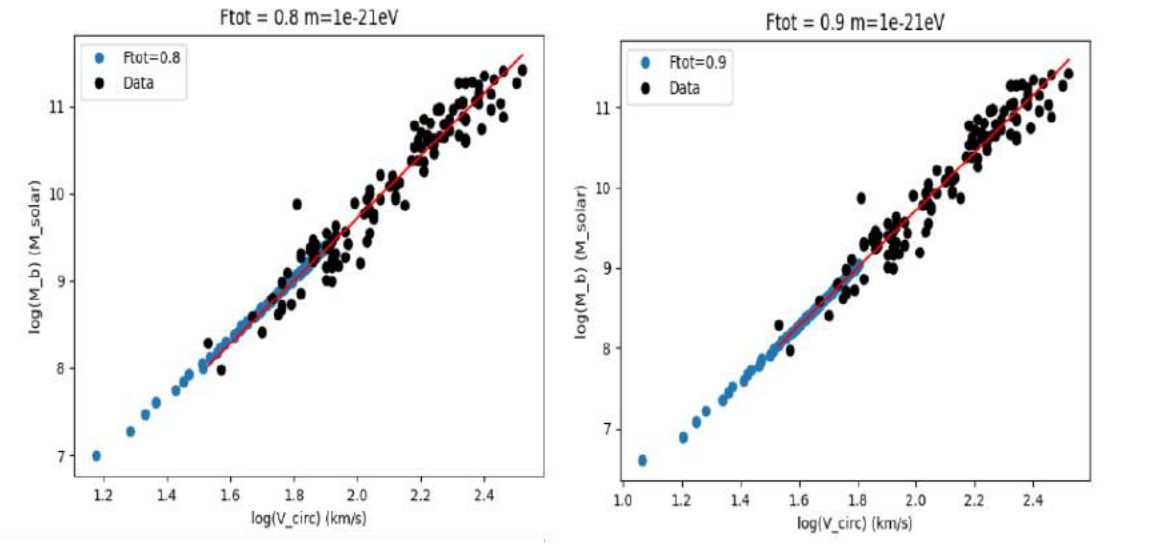

FIGURE 3.11: **Varying DM Fractions:** Example of varying the total DM fraction. Increasing the total fraction has the effect of shifting the entire BTFR towards lower masses. However, the range of reasonable value of the total fraction is too small to make a qualitative difference to the overall fit.

We did not consider the effects of varying the stellar-light-to-mass ratio, Υ_*. Importantly, changing the assumed value of Υ_* can change both the slope and intercept of the observed BTFR. Taking the value of Υ_* to be constant for Tully-Fisher type galaxies is a large simplification. We used a value of $\Upsilon_* = 0.5\frac{M_\odot}{L_\odot}$, which provided an excellent fit for the purposes of our analysis. Moreover, $\Upsilon_* = 0.5\frac{M_\odot}{L_\odot}$ minimizes the scatter in the observed BTFR. We expect that a careful treatment of Υ_* would produce the same overall trend in the simulated BTFR but with increased scatter. One possibility would be to vary Υ_* from galaxy to galaxy by sampling a distribution of values of Υ_* centered around the preferred value of $0.5\frac{M_\odot}{L_\odot}$. This would likely result in an increased scatter in the simulation.

Our lower bound of $m \geqslant 10^{-22}$eV is consistent with most other independent constraints (those presented in Chapter 1 for instance). We note that our analysis does not provide a clear preference for m so long as it is above this bound. However,

when comparing to other constraints and values, this analysis of the BTFR provides a unique interpretation in regards to the energetic aspects of galactic halos. In other words, the BTFR provides a means to estimate the excitation numbers of galactic halos for a given value of m; we discuss this feature in the coming subsections. Considering the lower end of constraint values for m, near 10^{-22}eV, comes with the interpretation that galactic halos have relatively low excitation numbers ($n < 100$). In contrast, higher values of m like those preferred by the Lyman-α Forest ($m \sim 10^{-20}$eV) come with the interpretation that galactic halos have much higher excitation levels ($n \sim 1000$). This is particularly important when one considers modelling individualized galactic halos, as the spatial extent of equally massed halos varies strongly with excitation number (see fig. 2.4).

3.7.2 BTFR Excitation Numbers

The halo excitation number is an important feature of our simulated BTFR galaxies. The value of the excitation number will determine where the galaxy lies on the BTFR, and is directly related to its expected baryonic mass content. Shown in fig. 3.12, we see that the baryonic mass is related to n by an approximate power law

$$M(n) \propto n^{1.3} \tag{3.31}$$

$$M(n) \approx C n^{1.3}. \tag{3.32}$$

We can use this relation to place an estimate on the excitation numbers for the BTFR. For instance, if we identify $M(1) = C$, then we can relate the mass of the Nth excited state as

$$\frac{M(n)}{M(1)} \approx n^{1.3} \tag{3.33}$$

Suppose then, for instance, we want to cover 4 orders of magnitude in M, similar to the BTFR, starting with the first excited state. With the above relation this would require $\frac{M(n)}{M(1)} = 1000$, implying that $n \approx 200$. Thus, if we want to cover the BTFR, starting with the first excited state, we require around 200 states. We verify

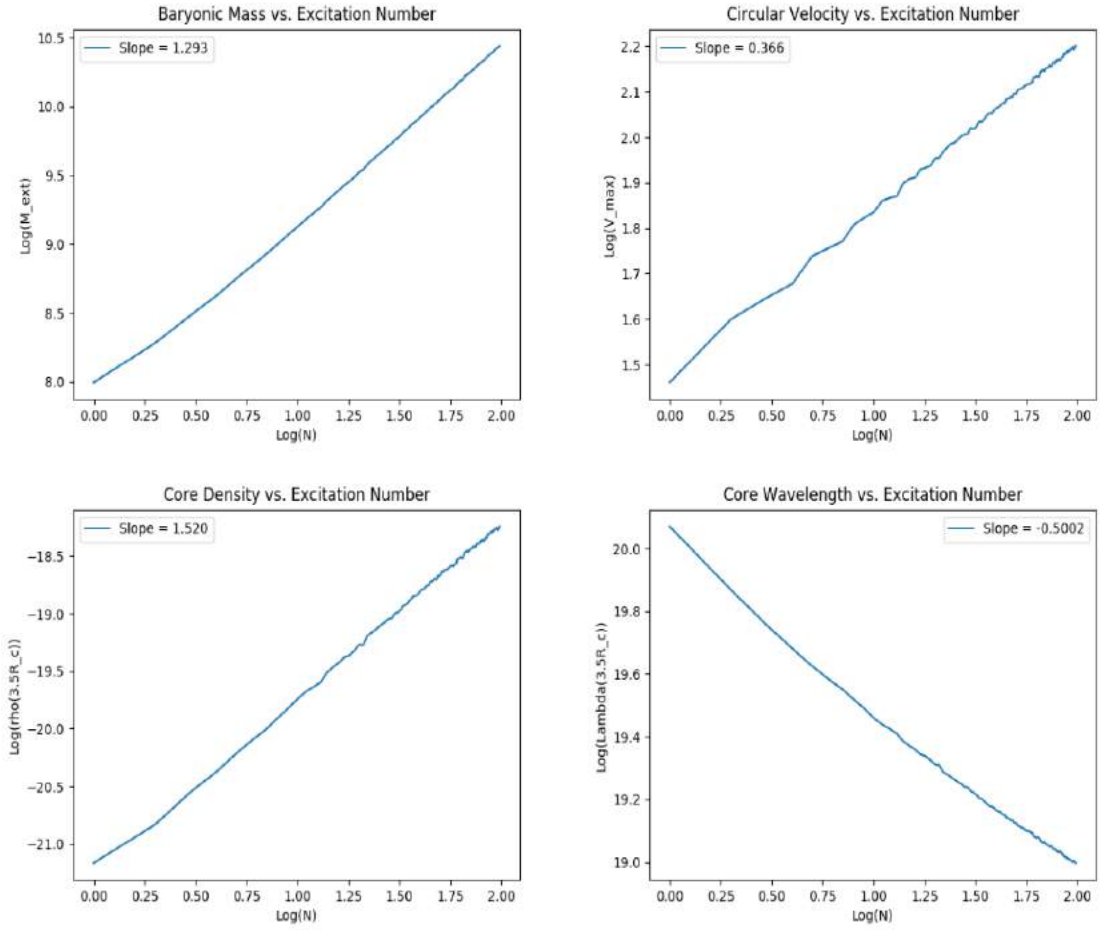

FIGURE 3.12: **Halo Properties vs. n:** Several trends for the $m = 10^{-22}$eV fit. Approximate power laws are extracted for the: Total baryonic mass (top left), "flat" circular velocity (top right), density at $3.5R_c$ (bottom left), and wavelength at $3.5R_c$ (bottom right). The bottom two relations imply a mass value at $3.5R_c$ which is held constant versus excitation number, namely $M = \frac{4\pi}{3}\lambda^3\rho$.

this result by referring to fig. 3.10 where we use 200 states and effectively cover the relation.

3.7.3 Individual Rotation Curves

The fact that SFψDM excited states can produce such a striking fit to the BTFR suggests that they can also be used to model the rotation curves of individual galaxies. We display our resulting rotation curves and a comparison to the SPARC survey for the $m = 10^{-22}$eV case in fig. 3.13. The rise of the rotation curve takes about 1kpc

while the flat portion can extend to the order of 10kpc or larger depending on the excitation number. We compute an averaged rotation curve similar to the averaging procedure from fig. 3.2, and compare it to that of the SPARC survey. While the baryonic contribution does not display a perfect fit, we suggest that this could be improved by a more rigorous treatment of the fraction f_h and the light-to-mass ratio Υ_*. We note that the case of $f_h \approx 0.5$ most closely resembles the case of real rotation curves. Nonetheless, the average rotation curve gives a good qualitative fit to the SPARC sample.

We used a spherically symmetric model of the baryonic contribution to the galactic rotation curve. This is a theoretically convenient choice, but nonetheless will affect the shape of the rotation curve. In reality, most Tully-Fisher galaxies have exponentially thin, disk-shaped, baryonic distributions. Our spherically symmetric profile of eq. 3.27 is merely meant as an approximation. This is likely one source of the discrepancy between our simulated rotation curves and the observed samples from SPARC. Given an improved model of the baryonic component, the methods in this paper remain valid as long as the model is spherically symmetric. A profile that resembles an exponential disk would require a more sophisticated treatment of the SFψDM excited states with such external contributions.

In regards to the BTFR fit, we do not expect the spherically symmetric approximation of the baryonic component to significantly affect our results. This is, again, due to the fact that the majority of the baryonic component is already enclosed by the time the flat rotational velocity is achieved. As a result, the flat rotational velocity will be affected only marginally by the shape of the baryon distribution. In other words, two different baryon distributions with the same total mass will contribute similarly to the flat rotational velocity in the outer parts of the halo, reproducing the same data point on the BTFR. Changing the model for the baryonic component will have a significant affect on the inner part of the rotation curve, but the outer part corresponding to the BTFR velocity will remain similar.

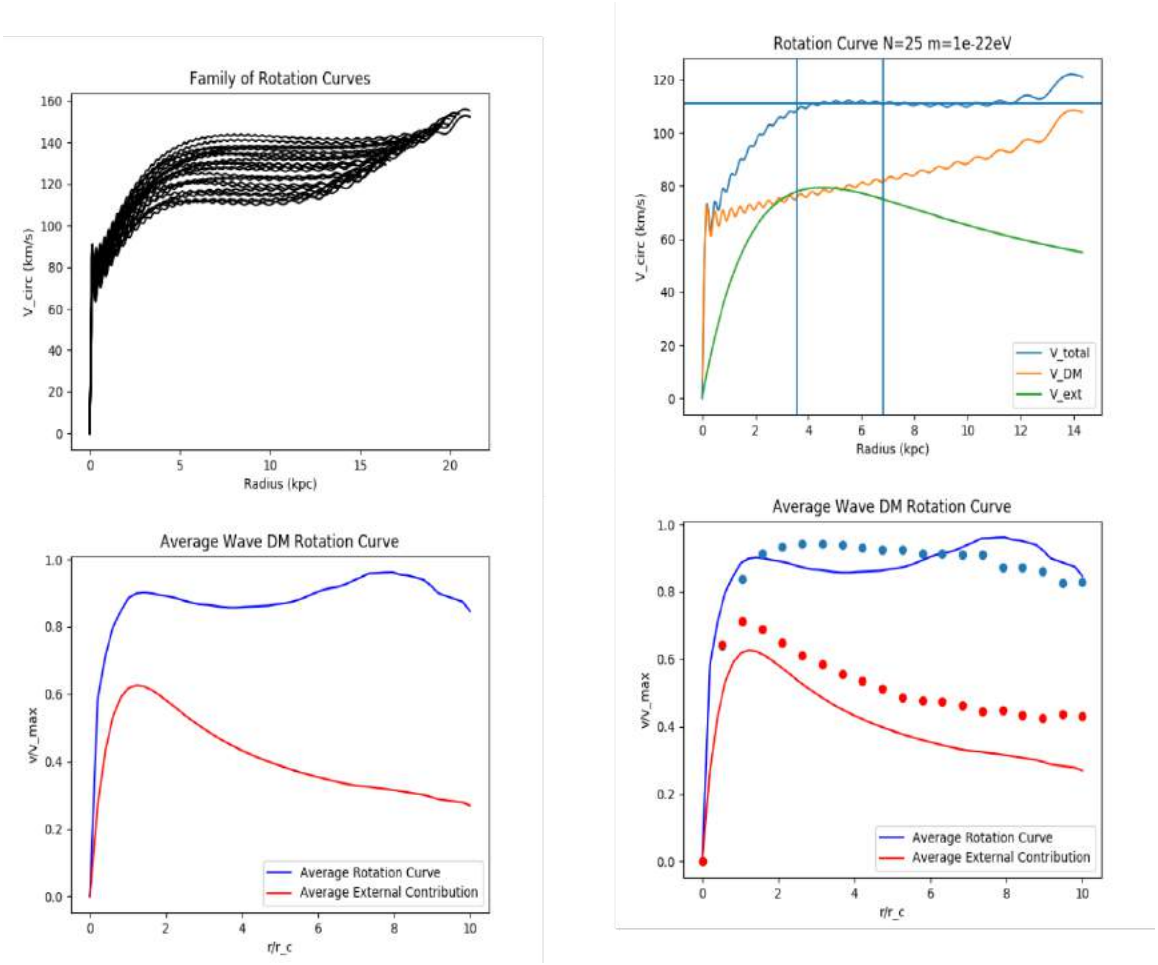

FIGURE 3.13: **Resulting Rotation Curves:** Rotation curves corresponding to the BTFR fit at $m = 10^{22}eV$, ftot = 0.9, and fb = 0.5. Units converted to kpc and km/s for realistic values. Top left: A selection of rotation curves with excitation numbers ranging from 25-50. Top Right: A single rotation curve. Vertical lines denote the values of R_h and $0.5R_d$ respectively. Horizontal line denotes the "flat rotational velocity." Bottom left: The averaged SFψDM rotation curve following the averaging procedure as in fig. 3.2. Bottom right: The same as the bottom left, but with the SPARC data superimposed for comparison.

3.7.4 Interpretation of Boundary Conditions

In simulating the BTFR, we solved a boundary value problem defined by eq. 3.17 to fix the amplitude and wavelength scales of the family of DM halos. Namely, we found that fixing a value of $\lambda^2 A$ for fixed values of m produces a BTFR-like trend which can then be scaled to overlap the observed BTFR. Each state was scaled to

have a similar density amplitude at the point where the product condition $I_n = I_{DM}$ is satisfied. In a sense, the "boundary radii" of R_n which achieve the product of I_{DM} are a computational convenience; they pick out the locations in the halos which are capable of being scaled to the same amplitude and wavelength. The physical interpretation is less clear, as this location almost always occurs in the outer regions of the halo. We wish to instead consider a boundary closer to the inner regions of the halo which reflects the discussion regarding fig. 3.6. In this section we provide a possible interpretation for this inner boundary.

If one interprets the DM halo as a central region surrounded by a region of quasiparticle fluctuations, a natural question would be "what is the fluctuation size at the inner boundary from fig. 3.6?" This boundary should hypothetically separate the inner core region from the outer quasiparticle region. A reasonable choice for this boundary is the radius of $r = 3.5r_c$, where r_c is the core radius defined as in eq. 2.55. It was shown in (62) that generic halos display a transition at this radius, corresponding from a transition from the inner soliton core to the outer N-body like region. We choose to extract the mass fluctuation size at this radius of $3.5r_c$ so as to make a comparison with the 3D simulation of (62). To do so, we consider the density amplitude as the approximate fluctuation density and the wavelength as its corresponding length scale. Returning to fig. 3.12, we display the dependence of $\lambda(3.5r_c)$ and $\rho(3.5r_c)$ on the excitation number, n. Interestingly, we find the following approximately rational power laws

$$\lambda(3.5r_c) \propto n^{-0.5} \tag{3.34}$$

$$\rho(3.5r_c) \propto n^{1.5}. \tag{3.35}$$

Combining these results in a relation between the density and wavelength of the DM halo at this transitional radius.

$$\rho(3.5r_c) \propto \lambda^{-3}(3.5r_c) \tag{3.36}$$

This relation provides a possible interpretation of the inner boundary in figure 3.6.

Notably, this boundary corresponds to a fluctuation mass which is approximately the same for all values of n, $M_{fluctuation} \approx \frac{4\pi}{3}(\frac{\lambda(3.5r_c)}{4})^3\rho(3.5r_c)$. We use the factor of $\frac{4\pi}{3}$ somewhat arbitrarily as an assumption that the fluctuations condense in a spherical manner; this factor may vary depending on the nature or shape of the fluctuation and should be further investigated. For the case of $m = 10^{-22}$eV, we extract this mass as on the order of $10^7 M_\odot - 10^8 M_\odot$. If such a mass fluctuation condensed into a stable soliton, it would correspond via eq. 2.47 to a radius of $R_{1/2} \approx 1kpc$, putting it on similar length and mass scales to that of globular clusters and galaxy cores. We suggest that this mass scale could be related to the galaxy formation process or to its parent subhalos. In practice, one may wish to identify the radii at which the proportions in eqs. 3.34 and 3.35 are exactly satisfied. This could give a more rigorous definition for the inner boundary between the soliton core and quasiparticle region.

4

Wave Dark Matter Superpositions and Oscillations

So far we have focused on describing SFψDM halos with generic solutions to the EKGEs and PSEs. In particular, we have explored the SSS solutions and used them to develop a first description of DM halos. The strength of this method lies in the fact that it allows one to explore the properties of halos in purely theoretical and mathematical context. Outside of the case of spherical symmetry, the equations which describe generic halos become increasingly and overwhelmingly complicated. This difficulty stems mostly from the non-linearity and complexity of the Einstein Equations. On the other hand, these difficulties can be addressed with computational methods like the ones used in (62; 75; 79) to simulate images like figs. 1.7 and 1.6. Such techniques are vital towards understanding how SFψDM halos form, behave, and evolve in a general context.

A purely numerical approach lacks the same descriptive power as a theoretical approach in which solutions can be decomposed and characterized in a mathematically precise fashion. Moreover, three dimensional numerical simulations of SFψDM can be slow and extremely expensive if one wishes to appropriately resolve the smaller scale wavelike nature of halos. In this section we focus on making a bridge between

these two methods. In particular, we will consider superpositions of states like the ones suggested in eq. 3.12 to create precise models of halos and their time evolution. We will then construct and demonstrate these solutions with numerical integration techniques to show correspondence between the methods. Finally, we will discuss the implications for physical SFψDM halos.

4.1 Halo Decomposition in Static Potentials

Returning to the discussion from section 3.3.1, we would like to describe SFψDM halos as solutions to the EKGEs. Ultimately, an expansion of the wave function in terms of spherical harmonics as in eq. 3.12 should provide a complete description of a halo. In practice, solving such an ansatz is difficult due to the non-linearity that arises from the couplings to the Einstein equations. This issue can be avoided if one assumes that the metric, and therefore the gravitational potential which influences the halo, is fixed in time. Effectively, this decouples the Klein-Gordon and Einstein equations. In this case, SFψDM can be described by the KG equation with a fixed potential, drastically simpler than the case of the coupled EKGEs.

As an illustration, we will consider the case that the halo resides in an approximately spherical and static gravitational potential. This should closely resemble the behavior of an isolated halo long after it has formed. We denote this potential and its corresponding mass distribution as $\{V_{gal}(r), M_{gal}(r)\}$. At the level of the metric line element, this is written as

$$ds^2 = -e^{2V_{gal}(r)}dt^2 + \left(1 - 2\frac{M_{gal}(r)}{r}\right)^{-1} dr^2 + r^2 d\theta^2 + r^2 \sin^2(\theta) d\phi^2. \tag{4.1}$$

We can then suppose that the SFψDM wave function can be decomposed in terms

of spherical harmonics as in eq. 3.12. That is, we define eigenfunctions ψ_{nlm} as

$$\psi_{nlm}(\vec{r},t) = r^l \Psi_{nl}(r) Y_l^m(\theta,\phi) e^{-i\omega_{nl}t}. \tag{4.2}$$

Then, we write the wavefunction as

$$\psi(\vec{r},t) = \sum_{nlm} A_{nlm}\psi_{nlm}(\vec{r},t). \tag{4.3}$$

The dynamics of the wavefunction are then determined by the KG equation with the metric of equation 4.1. Referring to the Appendix for details of the computation, the resulting equation for Ψ_{nl} is

$$\omega^2 e^{-2V} r^l \Psi_{nl} + \Phi(r^l\Psi_{nl})_{rr} + V_r(r^l\Psi_{nl})_r - \frac{1}{2}\Phi_r(\Psi_{nl}r^l)_r + \frac{2}{r}(\Psi_{nl}r^l)_r + \frac{l(l+1)}{r^2}\Psi_{nl}r^l = m^2\Psi_{nl}r^l. \tag{4.4}$$

The low field analog of this equation is rather simple, and can be found by taking $\Phi = 1$, and $V << 1$ in the above equation, or by simply applying the ansatz of eqs. 4.2-4.3 to the PS equation as opposed to the KG equation. Either way, the result is

$$(r^l\Psi_{nl})_{rr} + \frac{2}{r}(\Psi_{nl}r^l)_r = (2m(m-\omega+mV) - \frac{l(l+1)}{r^2})r^l\Psi_{nl}. \tag{4.5}$$

Simplifying further by applying the derivatives of r^l we reach

$$\Psi_{nl,rr} + \frac{2(l+1)}{r}\Psi_{nl,r} = 2m(m-\omega+mV)\Psi_{nl}. \tag{4.6}$$

One can notice that this is almost identical to the SSS version of the PS equation in eq. 2.52, except for the newly introduced $(l+1)$ term and a now static potential, V. The solutions for each value of l are analogous to the SSS excited states, and can be indexed by their number of nodes, n. Moreover, the eigenfunctions Ψ_{nl} and their corresponding frequencies, ω, can be well characterized with the Sturm-Liouville

theory for second order ODEs. This will be the focus of the following sections.

4.2 Sturm-Liouville Theory of the KG Equation

The equation describing the halo, eq. 4.4, is a linear, second order, ordinary differential equation. If one assumes the background potential is dominated by some static DM distribution, this equation can be thought of as describing the perturbations on that distribution. Solutions to such ODEs can be well categorized and decomposed in terms of orthogonal functions described by Sturm-Liouville (SL) theory. For those who are not familiar with, or would like a refresher on SL theory and its results, we include a discussion in the Appendix. We also defer the bulk of the computations regarding the SL form of eq. 4.4 to the Appendix.

4.2.1 Spherical Modes

As an illustration of the SL theory, we will first consider the spherically symmetric, $l = 0$ case of eq. 4.4. Importantly the properties of the non-spherical modes with $l > 0$ are quite analogous. Taking $l = 0$ only for the wave-function expansion we have

$$\psi = \sum C_{n0}\Psi_{n0}(r)e^{-i\omega_{n0}t}. \tag{4.7}$$

Taking $l = 0$ in eq. 4.4, each spherical mode is described by the following ODE:

$$\Psi_{n0,rr} + \left(\frac{2}{r} + V_{gal,r} + \frac{\Phi_{gal,r}}{2\Phi_{gal}}\right)\Psi_{n0,r} = \Phi_{gal}^{-1}(m^2 - \omega_n^2 e^{-2V_{gal}})\Psi_{n0}. \tag{4.8}$$

Again, we define $\Phi_{gal} = (1 - \frac{2M_{gal}}{r})$. We then enforce the separable boundary conditions that $\Psi_{n0}(0) = 1$ and that $\lim_{r\to\infty}\Psi_{n0}(r) = 0$. We note that in a computational sense, the condition at infinity must be artificially enforced at some large finite value of R; in such a case, the problem is a regular SL problem. SL theory then enforces that there is a lowest value of the frequency eigenvalue ω_n which generates a solution

with zero nodes. In general, the value of ω_0 is found via computational methods similar to those used to compute the SSS excited states. Further, there exists a countable number of frequencies of increasing value which denote solutions with integer numbers of nodes. Naturally, we can identify the integer n with this number. In the physical case of $R \to \infty$, the results are somewhat more complicated since the problem becomes a singular SL problem. We will see in the following discussion that this results in having two sets of orthogonal functions, a countable set representing finite and bounded modes, and a continuum set representing unbounded modes.

Case I. Discrete Bounded Modes, $\omega_0 < \omega_n < m$: In the case that $\omega_n < m$, solutions to eq. 4.4 are analogous to those of the SSS states. The behavior of Ψ_n will be oscillatory but eventually converge to exponential decay as V_{gal} tends towards zero at large distance. In principle, there exists an infinite and countable number of these modes in this finite frequency domain. In practice, computing these modes is limited by both the prescribed value of the computational boundary, R, and the precision with which one can estimate the eigenvalues. The frequencies become more and more closely spaced as n gets large. This is akin to the behavior of hydrogenic wave functions with energy eigenvalues becoming more closely spaced at higher excitation. In fact, in the low field equivalent, one can identify the energy eigenvalue as proportional to $(\omega_n - m)$, giving a direct analogy to energy eigenvalues. Importantly, these energy eigenvalues are negative. This is because the eigenfunctions constitute a finite total mass and have wavefunctions which decay at infinity. In other words, the energy is negative because the state is *gravitationally bounded* by the background potential. Sometimes, such states are referred to as *gravitational atoms*.

Case II. Unbounded Continuum Modes, $\omega > m$: For frequencies which exceed m, all solutions to eq. 4.4 are infinitely oscillatory. Moreover, such solutions correspond to an infinite amount of mass and have positive energy eigenvalues. We interpret these modes as unbounded or radiative modes. For a given choice of compu-

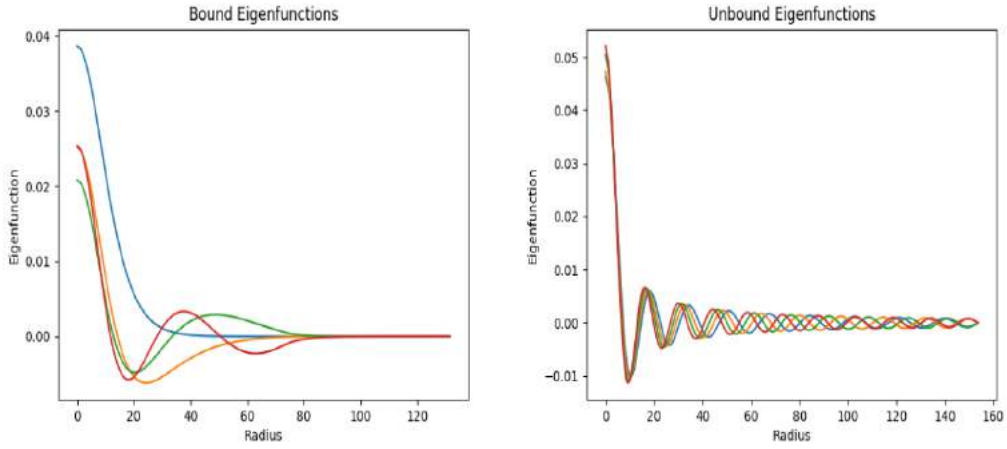

FIGURE 4.1: **Bounded and Unbounded Eigenfunctions:** We show the two distinct types of SL-Eigenfunctions which correspond to KG equation with a fixed spherical potential. Plots correspond to the functions Ψ_{nl} of eq. 4.4. Left: Bound eigenfunctions with $\omega < m$ are similar to the SSS states from chapter 3. These eigenfunctions display a countable number of zeros and then converge to zero via exponential decay. Right: Unbound eigenfunctions with $\omega > m$ oscillate indefinitely with an amplitude that converges to zero.

tational boundary, R, such modes can be used to describe matter which escapes the gravitational well of the simulation. In the case of $R \to \infty$, this would correspond to scalar radiation which is not gravitationally bounded to the DM halo and has velocity sufficient to escape the halo. We depict both the bounded and unbounded modes in fig. 4.1.

4.2.2 Non-Spherical Modes and Generation of Angular Momentum

The $l \neq 0$ cases of eq. 4.3 correspond to describing the non-spherical features of the halo. For the most part, the radial wavefunctions of Ψ_{nl} are similar to those of the $l = 0$ case in that there exist a countable number of bounded modes and a continuum of unbounded modes for each value of l. We note that only the $l > 0$ states have a non-zero angular momentum eigenvalue. This is directly resulting from the fact that the spherical harmonics, Y_l^m, are the eigenfunctions of the angular Laplacian. In other words, each mode has an angular momentum eigenvalue of $l(l+1)$. At the

level of the wavefunction, the rotational behavior can be explicitly seen when writing the spherical harmonics in terms of the associated Legendre polynomials P_l.

$$\psi_{nlm}(\vec{r},t) = r^l \Psi_{nl} P_l(\cos(\theta)) e^{i(m\phi - \omega_{nl}t)} \tag{4.9}$$

We see that each ψ_{nlm} is associated with a time dependent angular phase of $m\phi - \omega_{nl}t$. If superimposed with another mode, an $l = 0$ mode for instance, this will result in a rotating density interference pattern. As an example, we could encode some rotational motion into a soliton by having a wave function of the form

$$\psi(\vec{r},t) = A_{000}\Psi_{00}(r)e^{i\omega_{00}t} + A_{111} r \Psi_{11}(r) P_1(\cos(\theta)) e^{i(\phi - \omega_{11}t)}. \tag{4.10}$$

4.3 Pseudospectral Simulations

We choose to verify our SL analysis by comparing its conclusions to a full 3-dimensional simulation of the PSEs. Specifically, we will use the pseudospectral solving method from (62). This method utilizes unitary operations in combination with the Fourier transform to solve for the time evolution of the PSEs. Firstly, the values for $\psi(\vec{r})$ are placed onto a cubical grid with a resolution of N units per side. Denoting the Fourier transform and its inverse as F and F^{-1}, the Poisson Equation can be solved as

$$V = F^{-1}\left(\frac{F(4\pi|\psi|^2)}{k^2}\right). \tag{4.11}$$

This can be easily achieved in a computational sense by use of fast discrete Fourier transform (DFFT) algorithms. The time evolution of the wave function is then separated into three parts. First, denoting the time-step as Δt, the wave function evolves due to the potential for half of a time step through the operation of

$$\psi \rightarrow \exp\left(i\frac{\Delta t}{2} m V\right)\psi. \tag{4.12}$$

This is referred to as a "kick" by the potential. Next, the wave function must evolve due to the kinetic term $\frac{\nabla^2}{2m}$ of the Schrödinger equation. This is most easily achieved by applying a similar operation but in Fourier space. That is, the wave function's "kinetic drift" is computed as

$$\psi \rightarrow F^{-1}\left(\exp\left(i\Delta t\frac{k^2}{2m}\right)F(\psi)\right). \tag{4.13}$$

Lastly, the time evolution is completed by applying another potential kick for a half time step, repeating the transformation of eq. 4.12. This numerical method can then be iterated for the desired number of time steps. For accuracy and to maintain the stability of the solving routine, Δt must be chosen to be appropriately small. Criterion for a suitable Δt were determined in (79) as

$$\Delta t \leqslant \max\left\{\frac{m}{6}(\Delta x)^2, \frac{1}{m|V|_{max}}\right\}. \tag{4.14}$$

4.3.1 Boundary Conditions for Spectral Methods

The spectral methods described in the previous section naturally give rise to a solution with periodic boundary conditions and conserved total mass. Due to this feature, matter escaping one side of the simulation boundary will necessarily re-enter on another side. As such, halos simulated with spectral methods will be constantly disturbed by the presence of incoming and outgoing waves. This feature may be relevant for halos which are formed in a cosmological context, being disturbed from the formation of other nearby halos (62).

For simulations of more isolated halos, one may wish to reduce the level of interference which results from the periodic boundary. Conceptually, this can be achieved by removing matter which traverses the boundary. A "sponge" method for achieving this effect was proposed in (38) and utilized for simulations of isolated halos

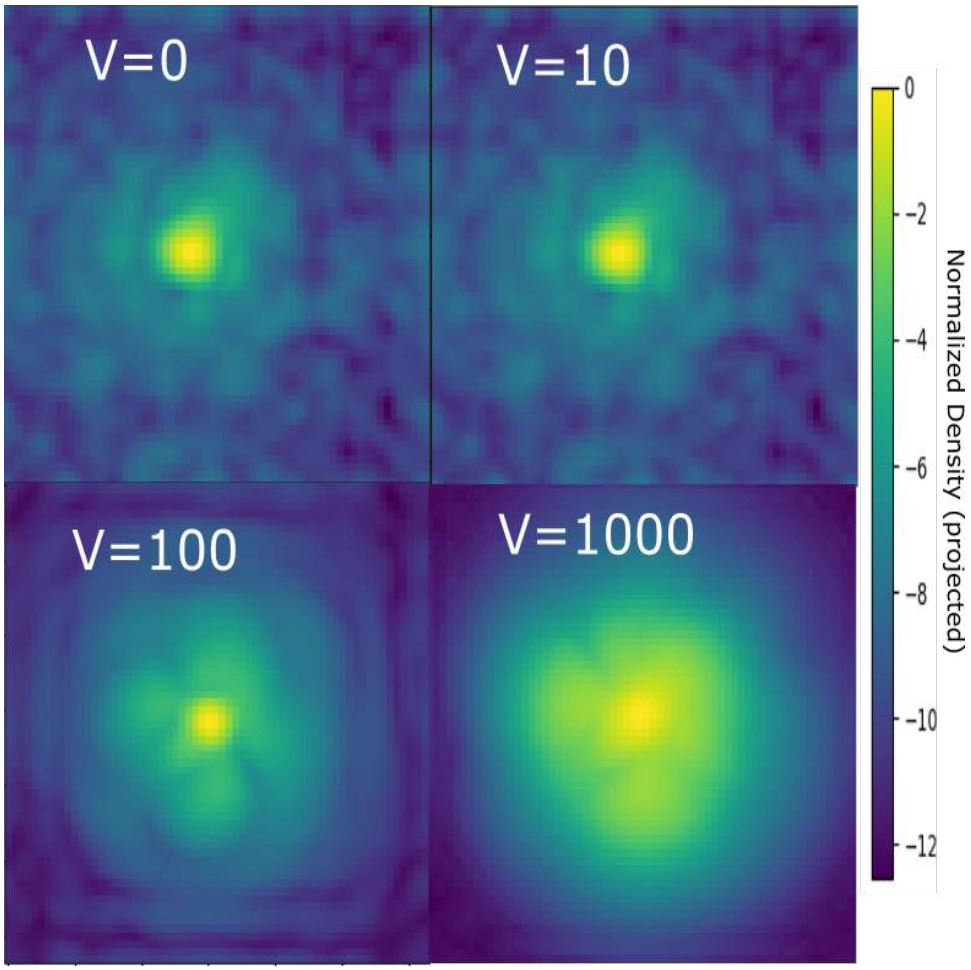

FIGURE 4.2: **Sponge Boundary Conditions:** Example of including sponge boundary conditions as in section 4.3.1. Each panel displays the result of a 3 soliton merger, each with equivalent initial conditions. Density is projected along the line of sight, normalized to the maximum value, and placed on a logarithmic color scale. V corresponds to the "height" of the sponge. A spherical sponge is placed at approximately half of the frame radius. (Top Left) With no sponge, boundary conditions are effectively periodic, allowing disturbances from waves entering and exiting at the boundary. This results in a turbulent region caused by the attenuation of such waves. The sponge acts as a "sink" for matter, causing densities to drop off at the sponge. (Bottom Left) For larger values of V, boundary conditions more closely represent those for undisturbed and isolated halos. Disturbances from travelling waves are greatly reduced, resulting in a less turbulent halo. (Bottom Right) As the sponge height is further increased, the halo disperses at an increasing rate, losing matter to the sponge and expanding due to scalar pressure.

in (79). One can include a "sponge" which removes matter by adding an imaginary potential to a boundary region. In other words one adjusts the potential as

$$V \to V + iV_{sponge}. \tag{4.15}$$

In the regions which contain the sponge, matter density is constantly lost. This can be understood by evaluating the corresponding continuity equation analogous to eq. 2.35. The imaginary part of V appears as a density source or sink, depending on its sign. Explicitly we have

$$\frac{\partial \rho}{\partial t} = \frac{\partial}{\partial t}(\psi^* \psi) + \nabla \cdot (\rho \vec{v}) = 2V_{sponge}\rho. \tag{4.16}$$

Regions with negative values of V_{sponge} will display density loss at a rate proportional to the magnitude of ρV_{sponge}. This can be used to impose an artificial boundary at which matter is removed from the simulation. Explicitly, we will use a sponge boundary of the form

$$V_{sponge} = -V_s \Theta(r - R_s). \tag{4.17}$$

We therefore define the sponge boundary with two parameters: the sponge height, V_s, and the radius at which the sponge is "turned on," R_s. For an example of the results of imposing a sponge boundary, see fig. 4.2.

4.4 Consistent SFψDM Superpositions States

It is a natural question to ask whether or not SFψDM halos can exist in a multi-state or superposition state configuration. In fact, multi-state boson star configurations have been considered in regards to modelling DM halos in multiple contexts (6; 37). In this chapter, we have defined how to attain superposition solutions to the KGE in terms of sets of orthogonal eigenfunctions. Computing these functions requires one approximate the galactic gravitational potential as spherically symmetric and static.

Once this potential is specified, the halo can be decomposed in terms of well defined eigenfunctions as in section 4.1. In this section, we will use these results to consider the notion of basic superposition halos.

Firstly, we need a working model of the gravitational potential in which the DM halo resides. Ultimately, this potential should be chosen to be consistent with the mass distribution of the halo itself, and for our purposes be SSS. One option to achieve this would be to start with a known solution to the EKGEs like a SSS excited state or a ground state soliton. For example, suppose we assume that the majority of the potential is determined by a soliton. We can compute a soliton solution $\psi(r,t) = \Psi_\Omega(r)e^{-i\Omega t}$ similar to that of eq. 2.22. Then, solving the SSS EKGEs, we can compute the wavefunction, potential, and mass distribution of the soliton and denote them as $\{\Psi_\Omega, V_\Omega, M_\Omega\}$.

Next, we use the soliton solution to pose the Sturm-Liouville problem, resulting in eq. 4.4, but with $V_{gal} = V_\Omega$ and $M_{gal} = M_\Omega$. There are a few features we can note for the eigenfunctions for fixed values of l. There will exist a countable set of solutions with $\omega_n < m$ that will be gravitationally bound to the galaxy. These solutions are finite in mass and are similar to the SSS states. There will also be a continuum of solutions with $\omega > m$ that are unbounded, akin to scalar radiation. Finally, for $l = 0$, one bounded state will necessarily have $\omega_n = \Omega$, and be a scalar multiple of the background soliton or excited state. This is merely the zero mode, an artifact of choosing to model the background with a SSS ground state.

Once the SL problem is solved and the bounded states are computed, we can explore the possibilities of halo superposition states. We can suppose the halo wave function to be of the form

$$\psi(r,t) = \Psi_\Omega(r)e^{-i\Omega t} + \sum_{nlm} A_{nlm}\psi_{nlm}(r)e^{-i\omega t}. \tag{4.18}$$

As long as the coefficients A_{nlm} are sufficiently small (that is $|A_{nlm}\Psi_{nl}|^2 << |\Psi_\Omega|^2$), then this wavefunction will be consistent with the background potential, V_Ω, to leading order. For the discussion in this section, we will consider only the gravitationally bound modes with $\omega < m$. The density of the halo can be computed by taking $|\psi|^2$. For the sake of simplicity, we show the resulting density for the case that only $l = m = 0$ contribute to the sum.

$$\rho(r,t) = \Psi_\Omega^2(r) + \sum_n |A_n\Psi_n|^2 + \tag{4.19}$$

$$\Psi_\Omega(r)\sum_n \left(A_n^*\Psi_n(r)e^{i\Omega_n t} + A_n\Psi_n(r)e^{-i\Omega_n t}\right) + \sum_{nm} A_n^* A_m \Psi_n(r)\Psi_m(r)e^{i\omega_{nm}t} \tag{4.20}$$

Here we identify halo oscillation frequencies of $\Omega_n = \Omega - \omega$ and $\omega_{nm} = \omega_n - \omega_m$. Mathematically, all values of n and m contribute to the sum, but in a practical application one will take finitely many terms. We see that each bound state contributes a small but constant density offset, represented by the second term in the sum. The third term, with the frequencies Ω_n, result in the largest density fluctuations. Importantly, these fluctuations are of order $|A_n\Psi_n\Psi_\Omega|$ as opposed to order $|A_n\Psi_n|^2$. One could interpret this set of oscillations as resulting from the interference of the bound states with the dominant soliton mode of the DM halo. The last set of oscillations, with the frequencies ω_{nm}, result from the interference of the bound states with each other, and are significantly smaller than the first set. Importantly, the halo oscillation frequencies are formed by differences of frequencies which are of order m. In the low field limit and non relativistic limit, the values of $(m - \omega_n) << 1$, thus the halo frequencies will satisfy $\Omega_n << 1$ and $\omega_{nm} << 1$ in that regime.

In this section, we have seen that a SFψDM halo in a static gravitational potential can host a variety of gravitationally bound modes that can cause density interference patterns throughout the halo. In full generality, the non-spherical modes with $l, m \neq$

0 as well as the gravitationally unbound modes with $\omega > m$ should be included. We will demonstrate these cases via numerical simulation in the following sections.

4.5 Simulations and Results

In this section we verify and demonstrate the results of the SL decomposition by comparing its predictions to the results of the pseudospectral simulations detailed in section 4.3. Specifically, we compute eigenfunctions which are bound by the gravitational potential of a soliton and assume the soliton to be the dominant source of the gravitational potential. Next, we use superposition states like eq. 4.18 to generate initial conditions for 3D pseudo-spectral simulations. Finally, we compare the time evolution of these simulations to the evolution predicted by the eigenfunction decomposition.

4.5.1 Spherical Modes and Core Oscillations

Oscillations of the core density are a common feature of SFψDM halos and can result from generic halo mergers. The magnitude of the core oscillations can be significant, up to 30% of the average central density depending on the simulation (62). The spherically symmetric density modes of section 4.2.1 provide a basic mechanism for these oscillations. When the coefficients, A_n, are taken to be real, the equation describing superpositions of spherical modes (eq. 4.19) can be reduced further to

$$\rho(r,t) = \Psi_\Omega^2(r) + \sum_n |A_n \Psi_n|^2 + \sum_n \Psi_\Omega A_n \cos(\Omega_n t) + \frac{1}{2}\sum_{nm} A_n A_m \Psi_n \Psi_m \cos(\omega_{nm} t). \tag{4.21}$$

Since all of the $l = 0$ wave functions have a finite and non zero central density, this will result in core oscillations characterized by the frequencies of Ω_n and ω_{nm}. The size of the oscillations will depend on the relative size of the soliton central amplitude, $\Psi_\Omega(0)$, and the central amplitudes of the trapped modes, $A_n\Psi_n(0)$. In fig. 4.5, we

show the superposition of the first excited spherical mode with a soliton background.

We see that the spectral simulation demonstrates the same relative oscillation frequencies as those that we can theoretically predict with the SL analysis. We can characterize the time periods of these oscillations in terms of the total halo mass as well as the mass parameter of the scalar field. We describe the leading order frequencies in the following discussion. Importantly, gravitationally bounded core oscillations can only result from the interference of the $l = 0$ modes, as all possible modes with $l > 0$ result in zero contribution to the central density due to being multiplied by r^l.

Core oscillations occur generically as the result of halo mergers. Even after long relaxation times, merged halos can still demonstrate significant core oscillations (62). We suggest that this is a result of DM being trapped in spherical modes. During the merging, halos can emit bursts of scalar radiation resulting from the excitation of highly energetic modes. Once initially relaxed, one can usually identify the presence of multiple spherical modes by investigating the core oscillations. We observe a gradual decay in these oscillations, with the highest frequencies decaying faster.

4.5.2 Angular Momentum and Spiral Patterns

We test the impact of imparting angular momentum by inlcuding non-spherical, $l > 0$ modes into the halo wavefunction. We consider the $l = 1$ case for our simulations, using wavefunctions of the form

$$\psi(\vec{r}, t) = \Psi_\Omega(r)e^{i(\Omega)t} + \sum_n A_n \Psi_{n0}(r)e^{i\omega_{n0}t} + \sum_{nm} B_{nm} r\Psi_{n1}(r)Y_1^m(\theta, \phi)e^{i\omega_{n1}t}. \quad (4.22)$$

Here we have included the spherically symmetric modes with $l = 0$ in the first summation, and the rotating non spherical modes with $l = 1$ in the second summation. We demonstrate cases including only the rotational modes as well as cases including

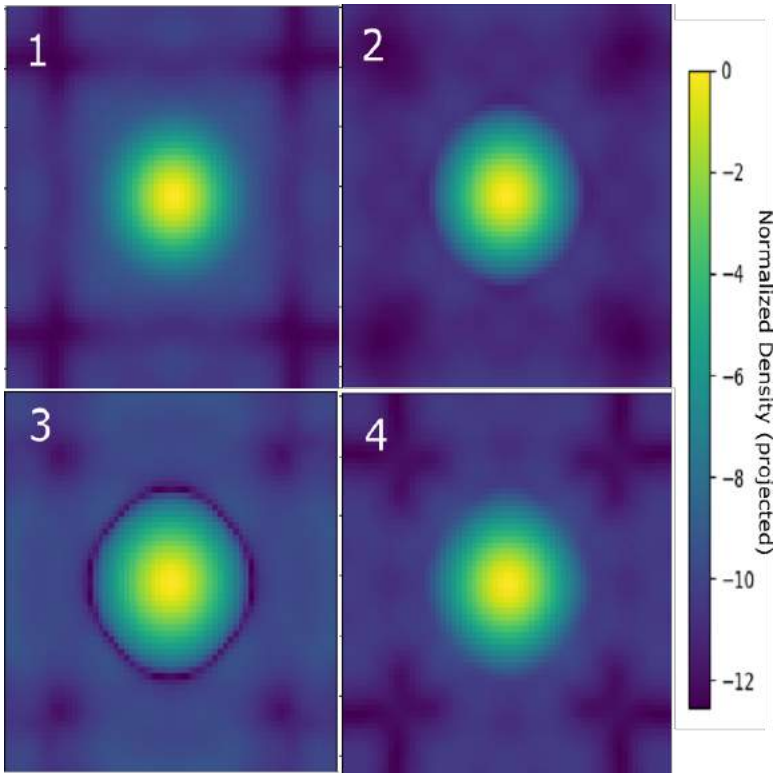

FIGURE 4.3: **Core Oscillations:** An example of a spherical oscillation mode. Density is projected along the line of sight, normalized to the maximum value, and placed on a logarithmic color scale. A soliton and an excited spherical mode (corresponding to eigenfunction with frequency ω_{100}) are initialized in a superposition. The configuration is evolved via the spectral method of section 4.3. We show a single oscillation period. Amplitudes are set such that the excited mode has a central density amplitude equal to 1% of the soliton's central amplitude. The oscillation generates a recurring density fringe corresponding to the overlap of the excited state. Video demonstration is available at https://www.youtube.com/watch?v=cb$_n GYe - A68$.

only the $l = 0$ spherical modes in figs. 4.4 and 4.5.

In fig. 4.4, we demonstrate the time evolution of an $l = 1$ mode. We observe that the rotation of the mode creates short lived spiral pattern in the DM density itself. We observe that the rotation lasts hundreds of rotation periods without decay and that it remains bound to the soliton. This is rather interesting and could perhaps provide a mechanism for generating long lived spiral patterns within a galactic disk, similar to (7). However, so far this is just a conjecture and would require an detailed

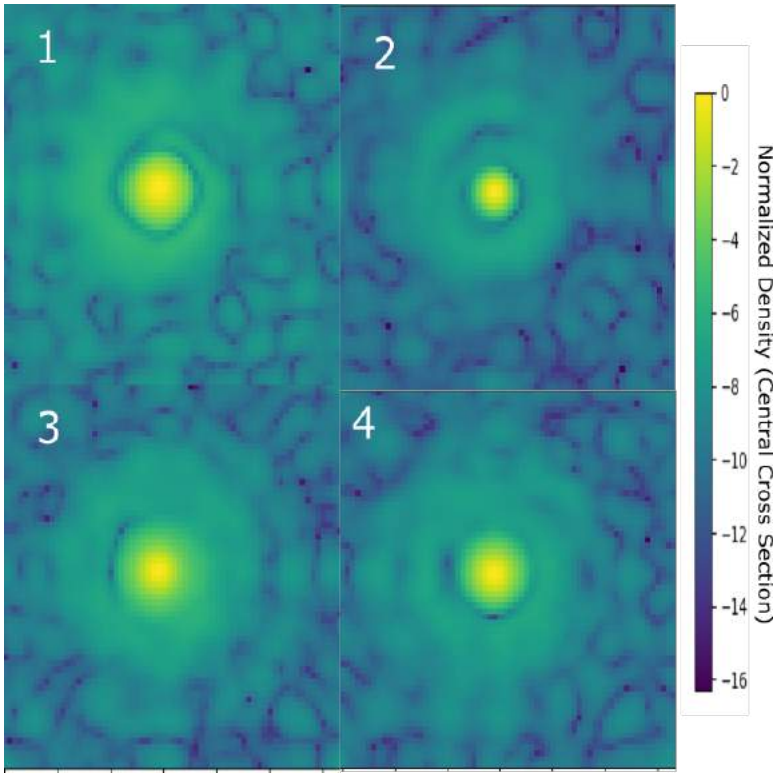

FIGURE 4.4: **Rotational Modes & Spiral Patterns:** An example of bound rotational modes and Dark Matter spiral patterns. The central cross section of the density is shown, normalized to the maximum value and placed on a logarithmic color scale. A soliton and a $l = 1$ mode (corresponding to ω_{111}) are initialized in a superposition. The configuration then evolves via the spectral method. The density amplitudes are chosen such that the excited state wavefunction amplitude is 1% of that of the soliton's at the center. We show the evolution of the rotational pattern; this does not necessarily correspond to one oscillation period. A counterclockwise rotational pattern is seen which persists for at least hundreds of oscillation periods. Video demonstration is available at https://youtu.be/YFVq4V5EvG4.

simulation which includes the evolution of baryonic matter. As a final note, even when the $l = 0$ modes are not included in the initial conditions, they are easily excited by computational defects. In other words, the error resulting from the discrete nature of the simulations can contribute to these oscillations; this results in an oscillating core density in effectively every simulated case.

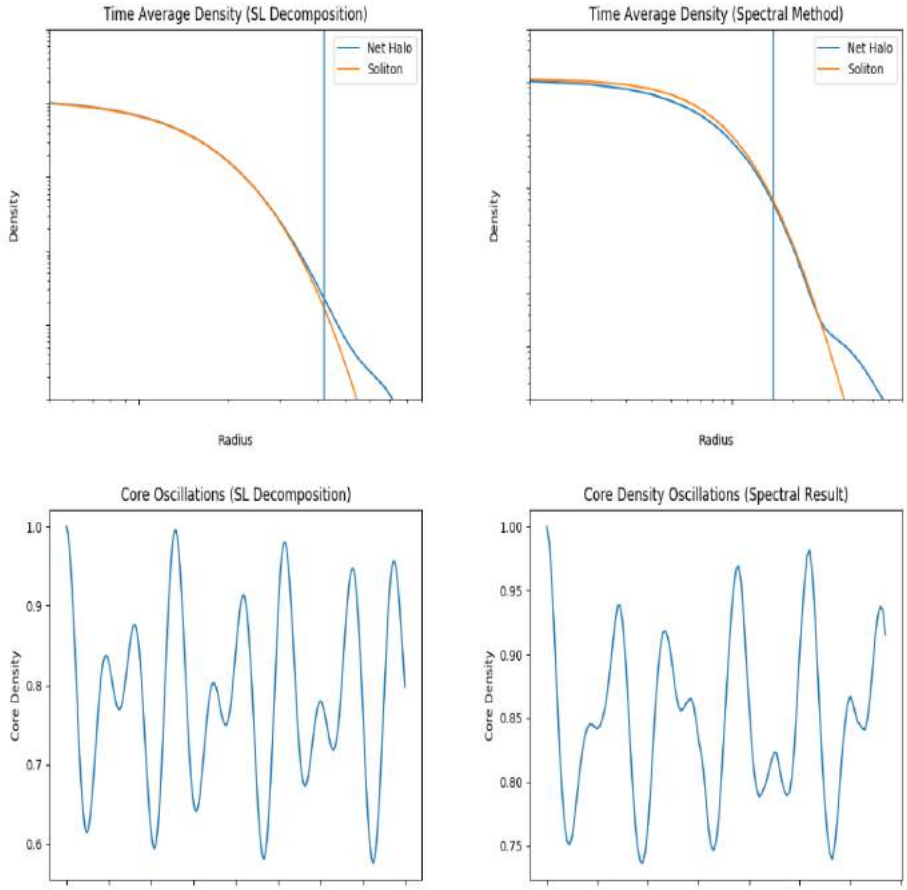

FIGURE 4.5: **Core Oscillations Result:** Results from superimposing a soliton with the first two excited state spherical modes. At the center, modes are give a density of .01 of that of the soliton. (Top) Comparison of the density profile predicted from the SL decomposition versus the results of the 3D Pseudospectral method. Vertical line corresponds to the value of $r = 3.5r_c$, denoting the "break" in the soliton profile. We superimpose the best fit soliton core. Qualitatively, the profiles experience the same profile break. The profile break occurs due to the outer maxima of the excited state. (Bottom) The core density extracted from each method and scaled to have a maximum density of 1. Each halo displays similar frequency patterns and oscillation amplitude.

4.5.3 Discussion

The eigenfunction analysis from this chapter provides a means to estimate the dominant frequencies at which SFψDM halos rotate and oscillate. In particular, we identified the difference frequencies ω_{nm} and Ω_n in section 4.4. As discussed in the prior sections, these frequencies can generate behaviors which are approximately long time stable. Since this analysis occurs in the low-field non-relativistic regime, the scaling relations of eq. 2.44 can be used to place values on the periods of these oscillations. Denoting the mass of the central soliton as M_{sol}, the oscillation periods obey the following generic proportion

$$T \propto M_{sol}^{-2} m^{-3} \tag{4.23}$$

Importantly, the oscillation periods have steep inverse scalings with M_{sol} and m. In other words, both larger halo mass and larger boson mass imply shorter oscillation periods. We will discuss a few simple cases of spherical modes and rotational modes. The interference of each mode with its host soliton has a characteristic frequency which we denote as $\Omega_{nlm} = \Omega - \omega_{nlm}$. We directly compute these frequencies using the SL eigenfunction analysis outlined in this chapter, and convert to their relative period $T_{nlm} = \frac{2\pi}{\Omega_{nlm}}$ [1].

$$T_{100} \approx 250ky \left(\frac{10^{10} M_\odot}{M_{sol}}\right)^2 \left(\frac{10^{-22} eV}{m}\right)^3 \tag{4.24}$$

$$T_{200} \approx 160ky \left(\frac{10^{10} M_\odot}{M_{sol}}\right)^2 \left(\frac{10^{-22} eV}{m}\right)^3 \tag{4.25}$$

$$T_{011} \approx 340ky \left(\frac{10^{10} M_\odot}{M_{sol}}\right)^2 \left(\frac{10^{-22} eV}{m}\right)^3 \tag{4.26}$$

[1] We use units of $1ky = 1000$years and $1My = 10^6$years

$$T_{021} \approx 210ky \left(\frac{10^{10} M_{\odot}}{M_{sol}}\right)^2 \left(\frac{10^{-22} eV}{m}\right)^3 \tag{4.27}$$

As a basic trend, we note that the values of T_{nlm} decrease as the values of n and l increase. The dependence on n is a result of the Sturm-Liouville analysis; for each fixed value of l, there exists a set of eigenfrequencies which increase with n. The l dependence can be explained as a result of the ODE in eq. 4.4; in other words, as a result of eq. 4.4, larger values of l correspond to a greater value for the fundamental frequency of the SL analysis.

It is important to ask whether or not these oscillation frequencies can be physically relevant on galactic scales. Answering this question definitively would require a full 3D simulation of a halo and the baryonic components it contains. However, our analysis still provides some insight as to what regimes may or may not be relevant in this regards. Firstly, we consider the period of the spherical mode T_{100}. For large dwarf galaxies, one can suppose that $M_{sol} \approx 10^9 M_{\odot}$. This results in a period of $T_{100} \approx 25My \left(\frac{10^{-22} eV}{m}\right)^3$. Interestingly, this is somewhat similar to the orbital periods that one expects to occur inside dwarfs. As a rough example, a circular orbit with a diameter of $\sim 10^4 ly$ and velocity of $\sim 100 \frac{km}{s}$ corresponds to a period of $\sim 100My$. Given that this is within an order of magnitude of T_{100}, it seems plausible that spherical oscillations are relevant to the dynamics of orbits in dwarfs for the $m \sim 10^{-22} eV$ regime. However, this window of opportunity swiftly vanishes as m is increases. For instance, the $m \sim 10^{-21} eV$ regime results in oscillations that are 1000 times faster than the relevant orbits, making it unlikely that the oscillations are relevant in this regime. This issue is somewhat reduced if one considers the halo to be in an excited configuration; we discuss the effect in the following paragraph.

Given the observation that the $l > 0$ modes result in stable rotational modes (as in fig. 4.4), one may ask whether or not these modes could be related to the patterns

that appear in spiral galaxies. Given our results, this at first seems very unlikely. Taking a value of $M_{sol} \sim 10^{12} M_{\odot}$, we return a value of $T_{011} \approx 34y \left(\frac{10^{-22}eV}{m}\right)^3$. This is many orders of magnitude smaller than orbits within spirals ($\sim 10 - 100My$) and should therefore be negligible to such orbits. On the other hand, this model considers the galactic halo to be well approximated by a soliton. We do not expect this to be true - in fact our results regarding the BTFR in chapter 3 suggest otherwise. We expect large spiral galaxies to have excitation numbers on the order of $n \sim 200$ or greater. As such, we should adjust the oscillation period according to this expectation. To do so, we utilize a result from (36) which estimates the dependence of excited state frequency, ω_n, with excitation number. For a fixed value of total mass, we have that $\omega_n \propto \frac{1}{n^2}$. We can then make an ad-hoc adjustment of T_{011} by multiplying it by n^2. Given $n = 200$, this results in a period of $T_{011} \approx 1.4My \left(\frac{10^{-22}eV}{m}\right)^3$, which is closer to the relevant regime. Therefore, if one supposes that the halos of spiral galaxies are in highly excited configurations, the bound SFψDM rotational modes could potentially be relevant. Whether or not large halos actually form these excited configurations remains an open question, requiring detailed simulations.

We emphasize that the eigenfunction analysis in this section should be further investigated with full 3D simulations which also include baryonic matter contributions. Overall, we expect our analysis to be a good first order description of halo oscillations. We note that spherical oscillations occur with periods that could be relevant in dwarf galaxies for the $m \sim 10^{-22}eV$ regime. This is consistent with results from (58) which suggests that core oscillations could result in observable orbital resonances within dwarf galaxies. Lastly, we note that 3D simulations of SFψDM halos on the mass and length scales of spirals like the Milky Way have not been achieved at this point. Whether or not such halos exhibit the properties of excited state configurations therefore remains a conjecture at this point. However, we re-emphasize

that the BTFR suggests this to be possible. A definitive conclusion as to whether or not rotational modes could be related to spiral patterns therefore requires further investigation.

5

Conclusions: On Excited States and the Future of SFψDM

This thesis had three main goals: To introduce the theory of SFψDM and its corresponding phenomenology (Chapter 1), to detail the theoretical basis of the EKG equations (Chapter 2), and to investigate and model excited state features of SFψDM halos (Chapters 3 and 4). In doing so, we achieved two main results: we showed that SFψDM excited states can produce a novel model/explanation of the BTFR (Chapter 3) and used that model to constrain the value of the SFψDM mass parameter m, and we showed that superpositions of excited states (Chapter 4) result in halo oscillations that may be relevant towards galactic length scales and time scales. This chapter is purposed towards summarizing these results, explaining their relevance for modelling galactic phenomena, and outlining some future directions for the study of SFψDM excited states and their features.

5.1 Excited States and the BTFR

The discussions of Chapter 3 were focused on furthering the work of (35) which showed that SSS SFψDM excited states, under appropriate boundary conditions, reproduce a trend similar to the BTFR but in a DMO setting. Following this observation, we developed a model for SSS halos in the presence of SSS distributions of baryonic matter. This enabled us to produce a simulation of the BTFR which was consistent with observational data. Moreover, analysis of this simulation allowed us to place a constraint on the value of m and relate this constraint to the excitation numbers of SFψDM halos. Importantly, our constraint on m provides a lower bound for both the value of m as well as the excitation number of halos corresponding to Tully-Fisher galaxies. This has an interesting consequence in that one is able to use this result to estimate halo excitation numbers given a value of m.

Our lower bound of 10^{-22}eV is consistent with most other independently computed constraints (like those discussed in Chapter 1). Using this value, Tully-Fisher galaxies are inferred to have excitation numbers on the order of $n \sim 1 - 200$. If one considers larger values of m, like those suggested by Lyman-α Forest observations ($m \geqslant 10^{-20}$eV), then the corresponding excitation numbers are increased substantially ($n \sim 10^3 - 10^4$). While we did not compute the direct relationship between the value of m and the corresponding excitation numbers, our results resoundingly suggest that the halos of Tully-Fisher galaxies can be modelled as being in highly excited states. This is quite interesting, especially given that most studies only consider soliton-like, ground state halos. This is usually justified by the fact that excited states are inherently unstable and that the soliton ground state is a stable attractor. Based on our BTFR results, we argue that this view is somewhat oversimplified and that excited state properties should be considered given the value of m. This could be particularly relevant for larger galaxies. In particular, when comparing a soliton

with an excited state of the same total mass, the soliton is much more compact and has a much greater central density; this can be seen in figure 2.4. Therefore, if one assumes a large halo to be in the ground state configuration as opposed to an excited state configuration, they may mistakenly expect an extremely dense central density which would not be realized by an excited state halo. Further, if one assumes two halos of different total mass to both be modelled by ground states, then the two halos could return vastly different constraints on m which would seemingly be inconsistent. We suggest that the smallest halos, like those of dwarfs, should be thought of as having the lowest overall excitation number and that more massive galaxies, like large spirals, should be thought of as being in highly excited states. Overall, we believe that the model of the BTFR from Chapter 3 should give good insight as to what excitation numbers one would expect.

The fact that excited state configurations are known to be unstable could possibly be misleading. In particular, the mathematical sense of stability is not necessarily what one would expect in a physical context. We argue that galaxies are in highly dynamical states that are constantly evolving in time. As a result, the transient features of excited states may still be realized in halos even though those halos wouldn't converge to an excited state in the mathematical sense. It is important to ask whether or not these transient features occur on timescales that are observable in the galactic context - this is partly the focus of Chapter 4. Going further, excited states are unstable in a purely DMO context. It is possible that other matter somewhat alleviates this instability - this principle has been demonstrated in (59).

Lastly, we would like to discuss what is meant by "boundary conditions" in the context of the BTFR and what relevance this may hold for halos. It is important to distinguish the boundary conditions from section 3.4.2 from the boundary conditions required to solve the EKGEs. All physical halos must obey boundary conditions at infinity. That is, all halos must respect the boundary conditions that

density converges to 0 at large distance and that total mass is finite. This is distinct from applying a scaling condition at a boundary as in Chapter 3. The amplitude-wavelength boundary conditions from Chapter 3 describe a means to scale excited state halos so that the family of excited states appropriately reproduces the BTFR. This result suggests that the BTFR is related to a characteristic mass scale, described in the results section of Chapter 3, that is held constant amongst the family of excited states. Interestingly, we found that this mass scale is directly related to the "break" in the halo profile at which the halo converts from a soliton-like core to an NFW-like region. We suggest that this mass scale is in somehow related to the quasiparticle fluctuations that occur in simulated halos. A further investigation of this mass scale and how it arises could be be particularly interesting and perhaps provide insight to SFψDM halo formation and halo substructure.

5.2 Superposition States and Halo Oscillations

Chapter 4 was focused on discussing the transient properties of excited states and how they might be realized in halos. In particular, we developed a theoretical model capable of describing superpositions of excited states in the presence of a stable soliton core. This relied on the use of Sturm-Liouville theory applied to the EKGEs. As a result, we found that superposition states can result in halo oscillations that occur on the same timescale as orbits within galaxies (around 10My for $m \sim 10^{-22}$eV). Moreover, in the perturbative regime, we observed that these oscillations persist for hundreds if not thousands of oscillation periods. Therefore, it is at least feasible for these oscillations to have an effect on orbital dynamics. Going further, we found that halo oscillations can generate spiral patterns, even in a DMO context. This is a peculiar feature of SFψDM that merits further investigation.

We consider the work of Chapter 4 to be a preliminary investigation of the notion of superposition states and suggest that it can be greatly extended. In particular,

our model could be extended to consider halos in which the dominant contribution is an excited state as opposed to a ground state - this could be a meaningful extension given that the BTFR of Chapter 3 suggest galaxies to be in highly excited states. For instance, our preliminary results for a soliton-dominated halo suggest rotational periods that are much too short for the generation of large spirals. However, we also demonstrated that adjusting this model to instead consider large spirals to be in highly excited states results in much more reasonable timescales, close to what one would expect for the generation of large spirals. This is a particularly interesting feature. Moreover even without such adjustments, the rotational timescales we found lie in the relevant regime for the generation of dwarf spiral galaxies. An investigation of dwarf spirals could provide unique insight towards this feature.

The existence of spherically symmetric oscillation modes is particularly relevant towards the dynamics of dwarf galaxies. This idea has already been investigated in the context of density oscillations of soliton cores. Core oscillations can be quite substantial (up to order 30% of the central density), even when the superposition states are in the perturbative regime. Moreover, core oscillations can be observed in nearly all generic simulations of SFψDM halos. It has been suggested that such oscillations can produce resonances with orbits within dwarf galaxies. Our results confirm that the timescales of core oscillations are within the relevant regime for this to occur. We suggest that such oscillations could be particularly relevant for the inner regions of dwarf galaxies, perhaps supplying energy to orbits in these regions. This may have an observable effect on the phase space distribution of such orbits or in the galaxy's velocity dispersion profile. However, this notion should be investigated further in order to make more quantifiable predictions. Doing so would involve simulating superposition states in the presence of baryonic matter, a natural next extension for our model.

Lastly, we note that the timescale at which superposition states oscillate de-

creases sharply with the value of m with an approximate scaling of m^{-3}, providing a somewhat narrow regime in which these timescales are relevant for galactic halos. This scaling could be somewhat alleviated by assuming that larger values of m correspond to halos with greater excitation number. However, the relationship between halo excitation numbers and the value of m is non trivial and should be further investigated to reinforce this notion.

5.3 Future Directions and Discussion

Our work in this thesis is unique in that it considers excited state features of SFψDM and shows that they could be relevant towards galactic scale phenomena. The results regarding the BTFR in Chapter 3 solidify this notion, showing that excited state configurations can reproduce the BTFR as well as a constraint on m consistent with other independent studies of SFψDM. Further studies of excited states could provide unique insights to the SFψDM theory. There are several avenues that we suggest could be fruitful in this regard: Modelling excited states outside of the restriction of spherical symmetry, the axially symmetric case for instance; simulating superposition states in the presence of excited state halos; modelling the inclusion of baryonic matter in the context of superposition states; investigating the characteristic mass scale implied by the BTFR; comparing oscillations which result from superpositions with the dynamics of dwarf galaxies, particularly dwarf spirals. These avenues represent a few possible directions for further understanding the physical relevance of excited states.

Solving the EKGEs and the PSEs can be challenging and mathematically intense. It is important to approach this issue from a theoretical perspective as well as with rigorous 3D simulations. Our results show that it is possible to successfully compare these two perspectives. 3D simulations of the largest halos, like those of Milky Way sized halos, are incredibly difficult and have not been achieved at the time of this

thesis, at least to our knowledge. This arises from the difficulty of resolving the deBroglie wavelength scale as well as the larger scale of the galaxy. These scales can differ by orders of magnitude, particularly for larger values of m, making it difficult to resolve both in simultaneity. On even larger scales, those of galaxy clusters for instance, this is exacerbated. We were able to approach the features of large spirals from a theoretical perspective in our study of the BTFR. This provides insight which at this point is not achievable with 3D simulations, highlighting the importance of this perspective. Further, in our investigation of superposition states, we found that the results of our theoretical predictions were consistent with the results of 3D simulations. Ultimately, both perspectives should be reconciled to achieve a complete understanding of SFψDM.

SFψDM is a rapidly growing field at the time of this thesis and represents a new frontier of DM physics. Investigating SFψDM phenomena can be somewhat overwhelming due to the complicated wave phenomena that occur in the theory. This is not a good reason to rule out the theory, we suggest quite the opposite. Studies of SFψDM offer a rich opportunity to learn from both a mathematical perspective as well as a physical perspective, providing a bridge between pure mathematical theory and physical observation. We suggest that advances in 3D modelling as well as the mathematical understanding of the EKGEs are equally important and likely to further our understanding of SFψDM. There are many theoretical avenues that have yet to be investigated. In particular, SFψDM can be motivated by geometric arguments unrelated to the common axion-like particle motivation. This is very interesting when considering the theory of General Relativity as a result of geometric theory. Further, the study of manifolds with non-trivial torsion is relevant not only to SFψDM but also to the field of Differential Geometry as a whole. Studying this class of manifolds and their possible physical manifestations therefore represents an important frontier for both DM physics and mathematics.

We would like to end this thesis with the following sentiment: understanding the full implications of the SFψDM theory will require a significant amount of creativity and attention to detail. It is important to investigate the basic assumptions that we make when comparing to observational data. For instance, asking the question "Is it appropriate to model halos as being in ground state configurations?" One could quickly dismiss this question due to the known instability of excited states and stability of the ground state. If we followed this conclusion exactly, our results regarding the BTFR may have never been achieved. This is not to suggest that such conclusions are not useful, but that they should always be considered in light of the assumptions that we make. Truly understanding SFψDM theory may require the community to challenge many such notions and conclusions; we see this not as an opportunity to contend with other studies, but as an opportunity to learn and question our own biases. SFψDM is a peculiar and difficult theory to understand, both a gift to the puzzling mind and important to our fundamental understanding of the universe.

Appendix A

Appendix

A.1 Numerical Solutions of the SSS EKGEs

This section is meant to outline some of the basic numerical and computational methods that this thesis used to solve the SSS EKGEs. These methods are similar to and inspired by those documented in the thesis of Andrew Goetz (35).

We start at the SSS EKGEs as listed in eqs. 2.23-2.25. To generate physically reasonable solutions with the standard convention for the gravitational potential, we must take the following set of assumptions:

$$M(0) = \Psi_r(0) = 0 \tag{A.1}$$

$$\lim_{r\to\infty} M(r) = M_\infty < \infty \tag{A.2}$$

$$\lim_{r\to\infty} V(r) = 0 \tag{A.3}$$

The first assumption is necessary to ensure regularity at the origin, $r = 0$. This can be concluded from considering the $\frac{M}{r^2}$ and $\frac{2\Phi_r}{r}$ terms in eqs. 2.24 and 2.25. Next, the assumption on $M(r)$ enforces solutions to have finite mass. Lastly, the assumption on $V(r)$ corresponds to taking the convention that the gravitational

potential approaches 0 at infinite distance from the origin. It should be noted that an arbitrary constant, $\bar{V}$, can be added to $V(r)$ without affecting the solution. Thus, a solution which satisfies the first two assumptions, but not the third can be made to satisfy the third by an appropriate adjustment of $V(r)$.

Each solution is then specified by a choice of initial conditions, $(\Psi_0, V_0) = (\Psi(0), V(0))$, as well as its frequency ω. We take the convention that the potential function, $V(r)$, is always negative, and thus consider only $V_0 < 0$. Moreover, we take $\Psi(0) > 0$ without loss of generality since solutions are equivalent under the transformation of $\Psi \to -\Psi$. The frequency must be in the regime of $\omega < m$ to generate bound states. Solutions with $\omega > m$ will be infinitely oscillatory, therefore violating the finite mass condition.

Solutions which satisfy the criteria of A.1-A.3 are specified by a choice of three parameters, with two continuous and one discreet parameter. For this section we will use the parameter set of (m, ω, n) to define the solutions. We note that there are many other was to parameterize the solutions, choosing (m, M_∞, n) for instance. For numerical purposes, it is convenient to consider the case in which the frequency ω is taken to be fixed, allowing one to solve a shooting problem for the central conditions of the $\Psi(r)$ and $V(r)$.

Solutions with fixed ω can be uniquely specified by their excitation number n. Finding a solution of order n requires one find the appropriate initial conditions at the origin for the chosen values of n and ω, $(\Psi_0(n,\omega), V_0(n,\omega)$. These initial conditions will then produce solutions $(\Psi(r;n,\omega), V(r;n,\omega), M(r;n,\omega))$ which must obey the criteria of eqs. A.1-A.3.

Taking a naïve guess of (Ψ_0, V_0) will likely result in solutions which are exponentially divergent shortly after the decay radius is reached, violating the criteria of eqs. A.2 and A.3. In fact, for a fixed value of Ψ_0, the set of V_0 which result in convergent solutions is countable; these V_0 correspond to bound, finite mass, excited states, but

do not necessarily satisfy the convention for V_∞. To make sure the condition for V_∞ is satisfied, one may consider the asymptotic behavior of $V(r)$. That is, for V to appropriately approach 0 in the Newtonian fashion, we can check for the following condition:

$$V(r) - \frac{1}{2}\ln\left(1 - \frac{2M(r)}{r}\right) = Y(r) \approx 0 \tag{A.4}$$

This condition is equivalent to the assumption that the spacetime metric is asymptotically Schwarszchild, or in other words that the potential $V(r) \approx \frac{M(r)}{r}$ at large radii.

Fixing the values of ω and n, computing the correct set of initial conditions for $\Psi(0)$ and $V(0)$ can be achieved through a shooting problem method. This can be achieved with the following routine:

- Choose a value of $\omega < m$, and guess a value for Ψ_0.
- Given Ψ_0, choose a value of V_0 which is consistent with the condition of $k^2(0) < 0$, this ensures the wavefunction is initially oscillatory as are the expected solutions.
- Solve the ODES of eqs. 2.23-2.25 up to the decay radius R_d where $k(R_d) = 0$, and extend the solution to a chosen maximum distance beyond R_d. Count the number of zeros Ψ displays up to this point, and denote it as N.
- To generate a solution of order n, adjust the value of Ψ_0 until $N = n$, record this value of Ψ_0 as Ψ_n.
- Further adjust Ψ_0 to attain a solution with $N = n + 1$, and record Φ_{n+1}
- The pairings (Ψ_n, V_0) and (Ψ_{n+1}, V_0) generate solutions with n and $n+1$ zeros, though may display exponential divergences.

- To find the set without exponential divergence, perform a bisection search in the value of Ψ_0. The bound, non-diverging solution with n zeros will lie on the boundary of solutions with n and $n+1$ zeros. Call the resulting value of $\Psi_0 = \Psi_1$.

- The pair (Ψ_1, V_0) generates a bound solution of order n, but may not have $V_\infty = 0$

- To achieve $V_\infty = 0$, perform a shooting problem in the value of V_0, repeating the entirety of the above procedure for each considered value of V_0. Note that the previous value of Ψ_1 will provide a good initial guess for the next iteration.

- Vary V_0 and repeat procedure until the condition A.3 is satisfied to a determined distance tolerance.

- Result is $(\Psi_0(n,\omega), V_0(n,\omega))$. To generate solutions for different values of ω (and therefore of different mass scale), apply the scaling relations from section 2.5.4 to find appropriate guesses for the parameters then repeat this entire procedure. In the low field regime, these guesses will approximate the actual solutions.

This procedure as outlined, will generate SSS solutions to the EKGEs. We will note that the same method can be applied to the low field PS analogs from eqs. 2.50-2.52. These solutions have been described in a DM only context with no contributions from external baryonic potentials. However, solutions which include external potentials due to other matter are quite analogous. The necessary conditions of eqs. A.1-A.3 can still be achieved in this setting with the procedure outlined above, though the use of a continuation parameter greatly simplifies the problem. To include an external potential then, one may repeat the above procedure first in a DM-only setting, and then slowly introduce the external potential by increasing the

continuation parameter. That is, considering $V_{tot} = V + \alpha V_{ext}$, the solution is close to that of the DM-only setting if α is taken sufficiently small. Therefore, utilizing small steps in α one may iterate this outlined procedure, incrementally finding new guesses for Ψ_0 and V_0 until solutions for $\alpha = 1$ are achieved, fully including the external contribution.

A.2 Sturm-Liouville Theory and the EKGEs

Sturm-Liouville theory is the theory of second order ordinary differential equations with the following canonical form:

$$\frac{d}{dx}\left\{p(x)\frac{dy}{dx}\right\} + q(x)y = -\lambda w(x)y \tag{A.5}$$

This ODE is said to form a *regular Sturm-Liouville problem* on a finite interval, $[a, b]$, given the following conditions and boundary conditions:

- $p(x)$, $p'(x)$, $q(x)$, $w(x)$ are continuous on $[a, b]$
- $p(x) > 0$, $w(x) > 0$, on $[a, b]$
- $\alpha_1 y(a) + \alpha_2 y'(a) = 0$ for $\alpha_1^2 + \alpha_2^2 > 0$
- $\beta_1 y(b) + \beta_2 y'(b) = 0$ for $\beta_1^2 + \beta_2^2 > 0$

For each regular Sturm-Liouville problem, there exists a set of values for λ which result in solutions satisfying the boundary conditions at $x = a$ and $x = b$. These values of λ are usually referred to as the problem's *eigenvalues*. Again, given that the problem is regular, these eigenvalues are countable and can be labelled as λ_n, corresponding to a solution to the ODEs denoted as $y_n(x)$. Moreover, when listed in increasing order, these eigenvalues correspond to solutions with exactly n zeros. That is, we can find eigenvalues such that

$$\lambda_0 < \lambda_1 < \lambda_2 < \lambda_3 ...$$

and such that $y_n(x)$ has exactly n zeros on the interval $[a, b]$.

A powerful feature of the Sturm-Liouville eigenvalue problem, is that the eigenfunctions $y_n(x)$ form an orthonormal basis on the interval $[a, b]$. That is to say, one can define the following inner product with use of the *weight function*, $w(x)$.

$$\langle y_n(x), y_m(x) \rangle = \int_a^b y_n(x) y_m(x) w(x) dx = \delta_{nm} \tag{A.6}$$

This inner product then allows one write any function, $f(x)$, which is defined on the interval $[a, b]$ to be written as an series of the eigenfunctions.

$$f(x) = \lim_{N \to \infty} \sum_{n=0}^{N} (A_n y_n(x)) \tag{A.7}$$

$$A_n = \int_a^b f(x) y_n(x) w(x) dx \tag{A.8}$$

This feature, akin to the Fourier series, is often utilized to solve complicated partial differential equations, such as the wave equation. For instance, consider the 1-dimensional wave equation, subject to the boundary condition of $y(a) = y(b) = 0$. Physically, this can be compared to standing waves on a fixed string.

$$c^2 \frac{\partial^2 y}{\partial x^2} = \frac{\partial^2 y}{\partial t^2} \tag{A.9}$$

Suppose we now assume a harmonic ansatz that $y_n(x, t) = Y_n(x) e^{i\omega_n t}$. This results in the following ordinary differential equation, subject to $Y_n(0) = Y_n(a) = 0$:

$$Y_n''(x) = -\frac{\omega}{c^2} Y_n(x) = -\lambda Y_n(x) \tag{A.10}$$

This ODE now forms a standard Sturm-Liouville problem, the solutions being the standard sine function:

$$Y_n(x) = \sin \frac{n\pi x}{a} \tag{A.11}$$

where the eigenvalues are $\lambda_n = \frac{n^2\pi^2}{a^2}$ and the weight function is trivially $w(x) = 1$. These eigenfunctions can now be used to solve a generic initial value formulation of this 1-D Wave equation, subject to the boundary conditions at $x = 0$ and $x = a$. That is, we can write the generic solution by combining our ansatz, with the orthogonality conditions of the eigenfunctions

$$y(x,t) = \lim_{N\to\infty} \sum_{n=0}^{N} \left(A_n y_n(x) e^{i\omega_n t} + B_n y_n(x) e^{-i\omega_n t} \right) \tag{A.12}$$

$$A_n + B_n = \int_0^a y(x,0) \sin(\frac{n\pi x}{a}) dx \tag{A.13}$$

$$i(A_n - B_n) = \omega_n \int_0^a y_t(x,0) \sin(\frac{n\pi x}{a}) dx \tag{A.14}$$

A.2.1 Singular SL Problems

If one or more of the SL conditions are violated, then the SL problem is referred to as *singular*. For the purposes of this thesis, we will consider a SL problem posed on an infinite domain, $[0, \infty)$. In the example of the wave equation from the previous section, this would correspond to having an infinitely long string with an endpoint fixed at the origin. This can have interesting results in terms of the eigenvalue problem. In particular, infinite domains allow for continuous spectra of eigenvalues.

In practice, solving singular SL problems amounts to taking the limit which extends the interval to have infinite length. For instance, in the case of a domain $[0, \infty)$, one may consider the ordinary SL problem on a domain of $[0, b]$ and examine the behavior of the ordinary problem while taking a limit $b \to \infty$. The analytical approach to taking this limit is dependent on the structure of the particular ODE being solved. In a computational sense, taking this limit corresponds to solving the ordinary problem on a larger and larger computational domain, emulating the behavior of the singular case.

A.2.2 SL Theory of the KG equation

In this section we will describe the SL theory for the KG equation under the influence of a fixed metric. As a starting point, we will evaluate the ansatz from eqsx 4.1 - 4.3. Firstly, we make the definition of $\Phi = (1-\frac{2M}{r})$ for simplicity of writing the equations. We then evaluate the KG equation by using the definition of the d'Alembert operator

$$\Box\psi_{nlm} = m^2\psi_{nlm} \tag{A.15}$$

$$|g|^{-1/2}\partial_\lambda(|g|^{1/2}g^{\lambda\mu}\partial_\mu\psi_{nlm}) = m^2\psi_{nlm} \tag{A.16}$$

Firstly, the determinant of the metric is $g = -e^{2V}\Phi^{-1}r^4\sin^2(\theta)$. Then, since the metric is chosen in a diagonal form, only the terms of the sum with $\lambda = \mu$ result in non zero contributions. Applying these two facts we arrive at

$$(e^{-V}\Phi^{1/2}r^{-2}\sin(\theta)^{-1})\left(\partial_\mu((e^V\Phi^{-1/2}r^2\sin(\theta))g^{\mu\mu}\partial_\mu\psi_{nlm})\right) = m^2\psi_{nlm} \tag{A.17}$$

Now we evaluate the sum over μ, noting that $g^{\mu\mu} = (g_{\mu\mu})^{-1}$, and we apply the derivative operations

$$\Box\psi_{nlm} = (e^{-V}\Phi^{1/2}r^{-2}\sin(\theta)^{-1})\{ \tag{A.18}$$

$$\partial_t((e^V\Phi^{-1/2}r^2\sin(\theta))(-e^{-2V})\partial_t\psi_{nlm})+$$

$$\partial_r((e^V\Phi^{-1/2}r^2\sin(\theta))(\Phi)\partial_r\psi_{nlm})+$$

$$\partial_\theta((e^V\Phi^{-1/2}r^2\sin(\theta))(r^{-2})\partial_\theta\psi_{nlm})+$$

$$\partial_\phi((e^V\Phi^{-1/2}r^2\sin(\theta))(r^{-2}\sin(\theta)^{-2})\partial_\phi\psi_{nlm})\}$$

Next, we evaluate the derivatives and simplify resulting in

$$\Box\psi_{nlm} = \{-e^{-2V}\partial_{tt}\psi_{nlm} + \Phi\partial_{rr}\psi_{nlm}+ \tag{A.19}$$

$$V_r\partial_r\psi_{nlm} - \frac{1}{2}\Phi_r\partial_r\psi_{nlm}+$$

$$2r^{-1}\partial_r\psi_{nlm} + r^{-2}\partial_{\theta\theta}\psi_{nlm}+$$

$$r^{-2}\cot(\theta)\partial_\theta\psi_{nlm} + r^{-2}\sin(\theta)^{-2}\partial_{\phi\phi}\psi_{nlm}\}$$

Finally, we apply the spherical harmonic ansatz of $\psi_{nlm} = r^l \Psi_{nl}(r) Y_l^m(\theta, \phi) e^{-i\omega_{nl}t}$ and utilize the fact that the spherical harmonics are eigenfunctions of the angular part of the d'Alembert operator. That is, we use the following fact

$$\left(r^{-2}\partial_{\theta\theta} + r^{-2}\cot(\theta)\partial_\theta + r^{-2}sin(\theta)^{-2}\partial_{\phi\phi}\right) Y_l^m = \frac{l(l+1)}{r^2} Y_l^m \tag{A.20}$$

This brings us the final form which is an ODE for Ψ_{nl} in terms of the variable r

$$\omega^2 e^{-2V} r^l \Psi_{nl} + \Phi(r^l \Psi_{nl})_{rr} + V_r(r^l \Psi_{nl})_r - \frac{1}{2}\Phi_r(\Psi_{nl} r^l)_r + \frac{2}{r}(\Psi_{nl} r^l)_r + \frac{l(l+1)}{r^2}\Psi_{nl} r^l = m^2 \Psi_{nl} r^l \tag{A.21}$$

We can now analyze this ODE with SL theory, and compute its eigenfunctions. Firstly, we will simplify the problem by taking the following substitutions

$$H_{nl}(r) = r^{l+1}\Psi_{nl}(r) \tag{A.22}$$

$$B(r) = V_r + \frac{\Phi_r}{2\Phi} \tag{A.23}$$

This brings the ODE to the more simplified form of

$$H_{nl,rr} + BH_{nl,r} - (\frac{B}{r} + \frac{m^2}{\Phi} + \frac{l(l+1)}{r^2})H_{nl} + (\frac{\omega^2 e^{-2V}}{\Phi})H_{nl} = 0 \tag{A.24}$$

We are now tasked with placing this equation into the SL form. We achieve this by defining the SL functions $p(r)$, $q(r)$, and $w(r)$ as

$$p(r) = \exp(\int_0^r B(s)ds) \tag{A.25}$$

$$q_l(r) = p(r)(\frac{B}{r} + \frac{m^2}{\Phi} + \frac{l(l+1)}{r^2}) \tag{A.26}$$

$$w_l(r) = p(r)\frac{e^{-2V}}{\Phi} \tag{A.27}$$

This finally brings the KG equation into the SL form

$$(p(r)H_{nl,r})_r - q_l(r)H_{nl} + \omega_{nl}^2 w(r)H_{nl} = 0 \tag{A.28}$$

We can finally identify the eigenvalues and draw the standard conclusions from SL theory. Firstly, we see that each value of l results in a distinct SL problem with an eigenvalue of ω_{nl}. Thus, for each value of l there exists a countable number of ω_{nl} with increasing eigenvalues. These solutions can be identified by their number of zeros, n. Lastly, if we wish to convert these eigenfunctions back into the corresponding density amplitude, we need just apply the relation of eq. A.22 to retrieve each $\Psi_{nlm}(r)$. A generic solution to the KG equation would then be expressed as

$$\psi_{nlm} = \sum_{nlm} A_{nlm} r^l \Psi_{nl} Y_l^m e^{i\omega t} \tag{A.29}$$

To isolate the coefficients A_{nlm} we can make use of the orthogonality conditions for both the spherical harmonics and for the eigenfunctions, giving

$$A_{n'l'm'} = \int \left(d\Omega Y_{l'}^{m'}(\theta,\phi) \int dr (r^{2(l+1)} w_l(r) \Psi_{n',l'}(r) \psi_{nlm}(r)(t=0)) \right) \tag{A.30}$$

In practice, evaluating these coefficients is a computationally intensive process. This is mainly due to the fact that each value of l has a countably infinite number of orthogonal modes characterized by n. Examining the form of this equation, we can identify the radial wave functions for each mode as $\rho_{nl} = r^l \Psi_{nl}$, showing that this orthogonality condition reduces to a simple wave function orthogonality with a weight of w_l. Even further, if one takes the low field limit, the value of $w_l(r) = 1$, showing an orthogonality between the wavefunctions when integrated over the full spatial volume.

Bibliography

[1] Code for anisotropies in the microwave background. `https://camb.info/`. Accessed: 2021-06-01.

[2] hubblesite. https://hubblesite.org/contents/news-releases/1999/news-1999-26.html, Jul 1999.

[3] Nicola C. Amorisco and A. Loeb. First constraints on fuzzy dark matter from the dynamics of stellar streams in the milky way, arxiv: 1808.00464.

[4] Kazunori Kohri B. J. Carr, Yuuiti Sendouda, and Jun'ichi Yokoyama. New cosmological constraints on primordial black holes. *Physical Review D*, 81, 2010.

[5] Eric F. Bell and Roelof S. de Jong. Stellar mass-to-light ratios and the tully-fisher relation. *Astrophys.J.*, 550:212–229, 2000, arXiv:astro-ph/0011493.

[6] A. Bernal, J. Barranco, D. Alic, and C. Palenzuela. Multistate boson stars. *Phys. Rev. D*, 81(044031), 2010.

[7] Hubert L. Bray. On dark matter, spiral galaxies, and the axioms of general relativity, 2010, arXiv:1004.4016.

[8] Hubert L. Bray and Alan R. Parry. Modeling wave dark matter in dwarf spheroidal galaxies, 2013, arXiv:1301.0255.

[9] Richard Brito, Vitor Cardoso, and Paolo Pani. Superradiance – the 2020 edition, 2020, arXiv:1501.06570.

[10] A. Burkert. Fuzzy dark matter and dark matter halo cores. *The Astrophysical Journal*, 904, 2020.

[11] Jiajun Chen et al. New insights into the formation and growth of boson stars in dark matter halos, arxiv:2011.01333.

[12] B. Chiang, H. Schive, and J. Niemeyer. Soliton oscillations and revised constraints from eridanus ii of fuzzy dark matter. *Phys. Rev. D*, 103(103019), 2021.

[13] Benjamin V. Church, Jeremiah P. Ostriker, and Philip Mocz. Heating of milky way disc stars by dark matter fluctuations in cold dark matter and fuzzy dark matter paradigms. *MNRAS*, 485, 2019.

[14] Douglas Clowe et al. A direct empirical proof of the existence of dark matter. *Astrophys.J*, 648(L109-L113), 2006, arXiv:astro-ph/0608407.

[15] Planck Collaboration. Planck 2015 results. xiii. cosmological parameters. *Astronomy and Astrophysics*, 594, 2015.

[16] The Event Horizon Telescope Collaboration. First m87 event horizon telescope results. i. the shadow of the supermassive black hole. *ApJL*, 875, 2019.

[17] H. Davoudiasl and P. Denton. Ultralight boson dark matter and event horizon telescope observations of m87. *Phys. Rev. Lett.*, (021102), 2019.

[18] Manfredo Perdigão do Carmo. *Riemannian Geometry*. Birkhauser Boston, 1979.

[19] Xiaolong Du. *Structure Formation with Ultralight Axion Dark Matter*. PhD thesis, University of Goettingen, 2018.

[20] Xiaolong Du, Christoph Behrens, and Jens Niemeyer. Substructure of fuzzy dark matter halos. *MNRAS*, 465, 2016.

[21] F. W. Dyson, A. S. Eddington, and C. Davidson. A determination of the deflection of light by the sun's gravitational field, from observations made at the total eclipse of may 29, 1919. *Philosophical Transactions of the Royal Society A*, 220:571–581, 1920.

[22] Albert Einstein. Explanation of the perihelion motion of mercury from the general theory of relativity. *Preussische Akademie der Wissenschaften, Sitzungsberichte*, part 2:831–839, 1915.

[23] Albert Einstein. The field equations of gravitation. *Preussische Akademie der Wissenschaften, Sitzungsberichte*, part 2:844–847, 1915.

[24] Alfred L. Tiley et al. The shapes of the rotation curves of star-forming galaxies over the last ≈10 gyr. 2018, arXiv:1811.05982.

[25] C.L. Bennett et al. Nine-year wilkinson microwave anisotropy probe (wmap) observations: Final maps and results. *ApJS 208 20*, 208(20), 2012.

[26] Dylan Nelson et al. The illustristng simulations: Public data release, 2018, arXiv:1812.05609.

[27] E. Armengaud et al. Constraining the mass of light bosonic dark matter using sdss lyman- forest. *MNRAS*, 471(4), 2017.

[28] J. Chen et al. New insights into the formation and growth of boson stars in dark matter halos. 2020, arxiv:abs/2011.01333.

[29] Philip Mocz et al. Galaxy formation with becdm – ii. cosmic filaments and first galaxies, 2019, arXiv:1911.05746.

[30] T. Kobayashi et al. Lyman- constraints on ultralight scalar dark matter: Implications for the early and late universe. *Phys. Rev. D*, 96(123514), 2017.

[31] V. Rubin et al. Rotation of the andromeda nebula from a spectroscopic survey of emission regions. *Astrophysical Journal*, 159, 1970.

[32] B.P. Abbott et al. (LIGO Scientific Collaboration and Virgo Collaboration). Observation of gravitational waves from a binary black hole merger. *Phys. Rev. Lett.*, 116(061102), 2016.

[33] C. W. F. Everitt et al. Gravity probe b: Final results of a space experiment to test general relativity. *Physical Review Letters*, 106, 2011.

[34] K. Freese. Review of observational evidence for dark matter in the universe and in upcoming searches for dark stars. *EAS Publications Series*, 36, 2009.

[35] Andrew S. Goetz. The einstein-klein-gordon equations, wave dark matter, and the tully-fisher relation, 2015, arXiv:1507.02626.

[36] Andrew S. Goetz and Alan R. Parry. Parametrizations of the poisson-schrödinger equations in spherical symmetry, 2015, arXiv:1510.04644.

[37] F.S. Guzman and L.A. Ureña-López. Gravitational atoms: General framework for the construction of multistate axially symmetric solutions of the schrödinger-poisson system. *Phys. Rev. D*, 101(081302(R)), 2020.

[38] F.S Guzman and U.L. Ureña-López. Evolution of the schrödinger-newton system for a self-gravitating scalar field. *Phys. Rev. D 69, 124033*, 69(124033), 2004.

[39] Benjamin Hamm. Scalar field wave (fuzzy) dark matter and the formation of galaxies. 2020, arxiv:2004.07792.

[40] James B. Hartle. *Gravity: An Introduction to Einstein's General Relativity.* Addison Wesley, San Francisco, 2003.

[41] Wayne Hu, Rennan Barkana, and Andrei Gruzinov. Cold and fuzzy dark matter. *Phys.Rev.Lett.*, 85, 2000.

[42] Lam Hui, Jeremiah P. Ostriker, Scott Tremaine, and Edward Witten. Ultralight scalars as cosmological dark matter. 2016, arXiv:1610.08297.

[43] Vid Iršič, Matteo Viel, Martin G. Haehnelt, James S. Bolton, and George D. Becker. First constraints on fuzzy dark matter from lyman- forest data and hydrodynamical simulations. *Phys. Rev. Lett.*, 119(031302), 2017, arXiv:1703.04683.

[44] J.D.Breit, S.Gupta, and A.Zaks. Cold bose stars. *Physics Letters B*, 140, 1984.

[45] David J. Kaup. The klein-gordon geon. *Physical Review*, 172, 1968.

[46] Stacy Y. Kim, Annika H. G. Peter, and Jonathan R. Hargis. There is no missing satellites problem. 2017, arXiv:1711.06267.

[47] Lachlan Lancaster, Cara Giovanetti, Philip Mocz, Yonatan Kahn, Mariangela Lisanti, and David N. Spergel. Dynamical friction in a fuzzy dark matter universe, 2019, arXiv:1909.06381.

[48] Federico Lelli, Stacy S. McGaugh, and James M. Schombert. The small scatter of the baryonic tully-fisher relation. 2015, arXiv:1512.04543.

[49] Federico Lelli, Stacy S. McGaugh, and James M. Schombert. Sparc: Mass models for 175 disk galaxies with spitzer photometry and accurate rotation curves. 2016, arXiv:1606.09251.

[50] D. G. Levkov, A. G. Panin, and I. I. Tkachev. Gravitational bose-einstein condensation in the kinetic regime. *Phys. Rev. Lett.*, 121(151301), 2018, arXiv:1804.05857.

[51] Bohua Li, Tanja Rindler-Daller, and Paul R. Shapiro. Cosmological constraints on bose-einstein-condensed scalar field dark matter. 2013, arXiv:1310.6061.

[52] Mark R. Lovell, Annalisa Pillepich, Shy Genel, Dylan Nelson, Volker Springel, Rüdiger Pakmor, Federico Marinacci, Rainer Weinberger, Paul Torrey, Mark Vogelsberger, Adebusola Alabi, and Lars Hernquist. The fraction of dark matter within galaxies from the illustristng simulations. 2018, arXiv:1801.10170.

[53] David Lovelock. The einstein tensor and its generalizations. *Journal of Mathematical Physics*, 12, 1971.

[54] L.Roszkowski, E.M Sessolo, and S. Trojanowski. Wimp dark matter candidates and searches - current status and future prospects. *Reports on Progress in Physics*, 81(6), 2018.

[55] M. Markevitch. Chandra observation of the most interesting cluster in the universe. 2005, arxiv:astro-ph/0511345.

[56] M. Markevitch et al. Direct constraints on the dark matter self-interaction cross-section from the merging galaxy cluster 1e0657-56. *Astrophys.J.*, 606:819–824, 2003, arXiv:astro-ph/0309303.

[57] David Marsh. Axion cosmology. *Physics Reports*, 643, 2016.

[58] David J. E. Marsh and Jens C. Niemeyer. Strong constraints on fuzzy dark matter from ultrafaint dwarf galaxy eridanus ii. *Phys. Rev. Lett.*, 123(051103), 2018, arXiv:1810.08543.

[59] Jeremy Louis Marzuola, Sarah Raynor, and Gideon Simpson. Nonlinear bound states in a schrödinger-poisson system with external potential. *SIAM J. Applied Dynamical Systems*, 16:226–251, 2017.

[60] Stacy McGaugh, Jim Schombert, Greg Bothun, and Erwin de Blok. The baryonic tully-fisher relation. *Astrophys.J.*, 533:L99–L102, 2000, arXiv:astro-ph/0003001.

[61] Charles W. Misner. *Gravitation.* W.H. Freeman, United States of America, 1970.

[62] Philip Mocz, Mark Vogelsberger, Victor Robles, Jesus Zavala, Michael Boylan-Kolchin, Anastasia Fialkov, and Lars Hernquist. Galaxy formation with becdm: I. turbulence and relaxation of idealised haloes. 2017, arXiv:1705.05845.

[63] Julio F. Navarro, Carlos S. Frenk, and Simon D. M. White. The structure of cold dark matter halos. *The Astrophysical Journal*, 462:563, 1996.

[64] Barrett O'Neill. *Semi-Riemannian Geometry with Applications to General Relativity.* Academic Press, London, 1983.

[65] Jeremiah P. Ostriker, Ena Choi, Anthony Chow, and Kundan Guha. Mind the gap: Is the too big to fail problem resolved? 2019, arXiv:1904.10471.

[66] S. Perlmutter et al. Measurements of omega and lambda from 42 high-redshift supernovae. *ApJ*, 517, 1998.

[67] D. M. Popper. Red shift in the spectrum of 40 eridani b. *Astrophysical Journal*, 120:316, 1954.

[68] Joel R. Primack and Michael A. K. Gross. Hot dark matter in cosmology, 2000, arXiv:astro-ph/0007165.

[69] Adam G. Riess et al. Observational evidence from supernovae for an accelerating universe and a cosmological constant. *The Astronomical Journal*, 116, 1998.

[70] K. Rogers and H. Peiris. Strong bound on canonical ultralight axion dark matter from the lyman-alpha forest. *Phys. Rev. Lett. 126, 071302*, 126(071302), 2021.

[71] V.C. Rubin, W.K. Ford, and N. Thonnard. Extended rotation curves of high-luminosity spiral galaxies. iv. systematic dynamical properties, sa - sc. *Apj*, 225:L107–L111, 1978.

[72] Remo Ruffini and Silvano Bonazzola. Systems of self-gravitating particles in general relativity and the concept of an equation of state. *Physical Review*, 187, 1969.

[73] Mohammadtaher Safarzadeh and David N. Spergel. Ultra-light dark matter is incompatible with the milky way's dwarf satellites. *ApJ*, 893, 2020.

[74] R. Scarpa. Modified newtonian dynamics, an introductory review. *AIP Conference Proceedings*, 822(253), 2006.

[75] Hsi-Yu Schive, Tzihong Chiueh, and Tom Broadhurst. Cosmic structure as the quantum interference of a coherent dark wave. 2014, arXiv:1406.6586.

[76] Hsi-Yu Schive, Ming-Hsuan Liao, Tak-Pong Woo, Shing-Kwong Wong, Tzihong Chiueh, Tom Broadhurst, and W-Y. Pauchy Hwang. Understanding the core-halo relation of quantum wave dark matter, ψdm, from 3d simulations. 2014, arXiv:1407.7762.

[77] Marc Schumann. Direct detection of wimp dark matter: Concepts and status. *J. Phys. G: Nucl. Part. Phys.*, 46, 2019.

[78] Katelin Schutz. Subhalo mass function and ultralight bosonic dark matter. *Phys. Rev. D*, 101(123026), 2020.

[79] B. Schwabe, J. C. Niemeyer, and J. F. Engels. Simulations of solitonic core mergers in ultralight axion dark matter cosmologies. 2016.

[80] Edward Seidel and Wai-Mo Suen. Oscillating soliton stars. *Phys. Rev. Lett.*, 66(1659), 1991.

[81] S.J. Sin. Late-time phase transition and the galactic halo as a bose liquid. *Physical Review D Part. Fields*, 50, 1994.

[82] Thomas P. Sotiriou and Valerio Faraoni. f(r) theories of gravity. *Rev. Mod. Phys.*, 82(451), 2010.

[83] L. Street, P. Suranyi, and L.C.R. Wijewardhana. Density profile of multi-state fuzzy dark matter. 2021, arXiv:2101.00349.

[84] A. Suarez and T. Matos. Structure formation with scalar-field dark matter: the fluid approach. *MNRAS*, 416, 2011.

[85] Abril Suárez, Victor Robles, and Tonatiuh Matos. A review on the scalar field/ bose-einstein condensate dark matter model. *Astrophysics and Space Science Proceedings 38, Chapter 9*, 2013, arXiv:1302.0903.

[86] The EAGLE team. The eagle simulations of galaxy formation: Public release of particle data, 2017, arXiv:1706.09899.

[87] William Thomson and Baron Kelvin. *Baltimore Lectures on Molecular Dynamics and the Wave Theory of Light*. Cambridge University Press, 2010.

[88] Heinz Andernach (translator) and Fritz Zwicky (author). English and spanish translation of zwicky's (1933) the redshift of extragalactic nebulae. 2017, arxiv: 1711.01693.

[89] Andrzej Trautman. Einstein-cartan theory. *Encyclopedia of Mathematical Physics Oxford: Elsevier*, 2:189–195, 2006, arxiv:gr-qc/0606062.

[90] R.B. Tully and J.R. Fisher. Reprint of 1977a&a;a....54..661t. a new method of determining distance to galaxies. *aap*, 500:105–117, Feb 1977.

[91] L.A. Ureña-López, T. Matos, and R. Becerril. Inside oscillations. *Classical and Quantum Gravity 19 23*, 19(23), 2002.

[92] Eleonora Di Valentino, Alessandro Melchiorri, and Joseph Silk. Planck evidence for a closed universe and a possible crisis for cosmology. *Nature Astronomy*, 4, 2020.

[93] Steven Weinberg. A new light boson? *Phys. Rev. Lett.*, 40(223), 1978.

[94] Hermann Weyl. *Space-Time-Matter*. Methuen Co. Ltd., London, 1922.

[95] Jaswant K. Yadav, J. S. Bagla, and Nishikanta Khandai. Fractal dimension as a measure of the scale of homogeneity. *MNRAS*, 405, 2010.

Biography

Benjamin Hamm attended public school in Bunn, NC, graduating from Bunn High School in 2012. He then attended North Carolina State University from 2012-2016 where he received a B.S. in Physics. In addition to pursuing his degree in Physics, he was a trombonist for the NCSU Jazz ensemble. From 2016-2021, he studied Dark Matter Physics at Duke university under the supervision of Hubert Bray and received his Ph.D. In addition to his studies at Duke, he taught hundreds of undergraduates in various courses for the departments of Physics and Mathematics. After receiving his Ph.D., he worked to develop blockchain and decentralized technologies.